Soltan Soltan

Interaction of Superconductivity and Ferromagnetism in YBCO/LCMO Heterostructures

Cuvillier Verlag Göttingen

Interaction of Superconductivity and Ferromagnetism in YBCO/LCMO Heterostructures

Von der Fakultät Mathematik und Physik der Universität Stuttgart
zur Erlangung der Würde eines Doktors der Naturwissenschaften
(Dr. rer. nat.)
genehmigte Abhandlung

vorgelegt von

Soltan Eid Abdel-Gawad Soltan

aus Giza (Ägypten)

Hauptberichter : Prof. Dr. M. Dressel
Mitberichter : Prof. Dr. H. Kronmüller

Tag der Einreichung: 23.12.2004
Tag der Prüfung: 26.01.2005

MAX-PLANCK-INSTITUT FÜR FESTKÖRPERFORSCHUNG
STUTTGART
2005

Bibliografische Information Der Deutschen Bibliothek
Die Deutsche Bibliothek verzeichnet diese Publikation in der Deutschen Nationalbibliografie; detaillierte bibliografische Daten sind im Internet über http://dnb.ddb.de abrufbar.
1.Aufl.-Göttingen: Cuvillier, 2005
Zugl.: Stuttgart, Univ., Diss.,2005
ISBN 3-86537-349-6

Nonnenstieg 8, 37075 Göttingen
Telefon: 0551-54724-0
Telefax:0551-54724-21
www.cuillier.de

1.Auflage, 2005 Gedruckt auf säurefreiem Papier
ISBN 3-86537-349-6

Zusammenfassung

Die Wechselwirkung von Ferromagnetismus und Supraleitung wird anhand von Mehrfachschichten aus dem Ferromagneten $La_{2/3}Ca_{1/3}MnO_3$ (LCMO) und dem Supraleiter $YBa_2Cu_3O_{7-\delta}$ (YBCO) studiert. Die Tatsache, dass die Gitterparameter der ab-Ebenen dieser Materialien sehr ähnlich sind, erlaubt ein epitakisches Wachstum von LCMO/YBCO Schichten, Heterostrukturen und Überstrukturen mit strukturell scharfen Grenzschichten. Diese LCMO/YBCO-Strukturen repräsentieren adäquate Modelsysteme, um die Wechselwirkung der zwei antagonistischen Ordnungsphänomene zu untersuchen.

Obwohl die Erforschung des Proximity-Effektes vor 40 Jahren begann, wurde die Technologie zur Herstellung und Messung von Proben mit mesoskopischen Ausdehnungen erst vor kurzem entwickelt, insbesondere wurde es möglich, Supraleiter/Normalleiter-Strukturen zu untersuchen, welche aus dünnen Schichten bestehen, deren Dicken kleiner als die Kohärenzlänge des Supraleiters ist. Solche Strukturen verhalten sich wie isolierte Supraleiter mit nicht trivialen Eigenschaften.

Viele dieser Strukturen wurden bereits für den Fall ideal durchlässiger Grenzflächen untersucht. Gleichzeitig erfordert der experimentelle Fortschritt eine Weiterentwicklung der Theorie, insbesondere um eine allgemeine Grenzflächentransparenz zu berücksichtigen. Dieser entscheidende Parameter bestimmt die Stärke des Proximity-Effektes und ist zugleich nicht direkt messbar. Vom praktischen Standpunkt aus können Supraleiter/Normalleiter Proximity-Strukturen als Supraleiter mit veränderlicher Parametern betrachtet werden, insbesondere die Energielücke und die kritische Temperatur betreffend. Die Parameter der Proximity-Strukturen sind regelbar z.B. durch Variation der Schichtdicke.

Diese Methode hat bereits bei Supraleitenden Transition-Edge-Bolometern und Photo-Detektoren in der Astrophysik Anwendung gefunden.

Die Physik von Supraleiter/Ferromagnet-Systemen ist noch reichhaltiger. Im Gegensatz zum Fall Supraleiter/Normalleiter, fällt der Ordnungsparameter der Supraleitung nicht in einfacher Weise im nicht-supraleitenden Metall ab, sondern kann auch oszillieren. Dieses Verhalten ergibt sich aus der Austauschenergie J_{spin} der Quasiteilchen. Beim klassischen Ferromagneten (J_{spin} = 1 eV) wirkt es wie ein Potential mit verschiedenen Vorzeichen für die Elektronen eines Cooper-Paares und führt zu einem endlichen

Paarimpuls. Diese Oszillationen zeigen sich in einer nicht-monotonen Abhängigkeit der kritischen Temperatur T_{c} des Supraleiter/Ferromagnet-Systems von der Dicke der ferromagnetischen Schicht. In den meisten Arbeiten, die diesen Effekt untersuchen, sind die Methoden zur Berechnung von T_{c} zur Näherungs-Rechnungen.

Alle Proben dieser Arbeit wurden durch gepulste Laserdeposition hergestellt. Die besten Herstellungsbedingungen für LCMO/YBCO Doppelschichten oder Überstrukturen von STO-Einkristallen sind T_{s} = 780°C bei einen Sauerstoffdruck von 0.4 mbar im Fall von LCMO und 0.6 mbar im Fall von YBCO. Röntegen-diffraktormetriesch Untersuchungen zeigen ein hochgeordnetes Wachstum beider Materialien, und Untersuchungen der ab-Ebenen der Filme zeigen auch eine Orientierung der in-plane-Achsen.

Diese Doppelschichten und Multilagenschichten hoher struktureller Qualität wurden experimentell erforscht, um die Wechselwirkung zwischen ferromagnetisch geordneten LCMO hoher Spin-Polarisierung und dem Hochtemperatur-Supraleiter YBCO zu untersuchen.

Die Hauptergebnisse dieser Arbeit können in drei Teile gegliedert werden:

Untersuchung der Diffusion Spinpolarisierung Quasiteilchen in den Supraleiter bei Doppelschichten aus 50 nm LCMO und variierender YBCO-Schichtdicke:

- Mittels SQUID Magnetometrie wurde herausgefunden, dass alle LCMO/YBCO Doppelschichten ferromagnetische und supraleitende Ordnung bei tiefen Temperaturen zeigen.

- Die kritische Temperatur T_{c} von YBCO in LCMO/YBCO Doppelschichten wird für Dicken d_{YBCO} < 30 nm stark herabgesetzt.

- Es wurde ein theoretisches Modell entwickelt, welches auf dem Parker-Modell für Nichtgleichgewichts-Supraleitung basierend in der Lage ist, die experimentell für verschiedene Schichtdicken gefundenen Übergangstemperaturen vorherzusagen.

- Mit diesem Modell war es möglich, die Spin-Diffusionslänge ξ_{fm} in YBCO zu ξ_{fm} $\approx$ 10 nm bei tiefen Temperaturen zu bestimmen.

Es wurde eine ausgefallene Geometrie für eine LCMO/YBCO Heterostruktur entwickelt, welche die Injektion spinpolarisierter Quasiteilchen in die YBCO-Schicht erlaubt:

- Die Injektion von Strömen durch spin-polarisiertes LCMO in YBCO führt zu einem deutlichen Abfall von T_{c} , viermal stärker im Vergleich mit einem Injektionsstrom durch nicht-spin-polarisiertes Material. Dieses wird als Nachweis Spin-Injektion in YBCO angesehen.

- Es wurde herausgefunden, dass die Injektion spinpolarisierter Quasiteilchen zu einem Abfall des normalleitenden Widerstandes, ρ_{ab}(T) von YBCO bei Temperaturen nahe T_{d} = 200 K führt.

- Dieser Widerstandsabfall kann durch ein Öffnen des Pseudogaps im YBCO-Film erklärt werden. Das Spin-Charge-Seperations-Modell von P.W. Anderson läßt eine Wechselwirkung der injizierten spinpolarisierten Quasiteilchen mit der Lücke vermuten, was zu einer erhöhten Leitfähigkeit führt.

- Ein Abfall des Widerstandes wird nicht gefunden, falls die spin-polarisierten Elektroden entweder durch nicht polarisiertes Material ersetzt werden, oder falls ein dünner isolierender STO-Film LCMO und YBCO entkoppelt.

Die kritische Stromdichte j_c von YBCO in Doppelschichten wurde ortsaufgelöst mittels einer quantitativen magneto-optischen Technik bestimmt:

- Die kritische Stromdichte j_c in ferromagnetischen/supraleitenden Doppelschichten wird im Vergleich zu einer isolierten YBCO-Schicht stark reduziert.

- Eine Änderung des Magnetisierungszustandes der LCMO-Schicht beeinflusst direkt die kritische Stromdichte des Supraleiters. Dieser Effekt kann zu einer Änderung von j_c von bis zu 50% führen.

- Die elektronische Entkopplung von LCMO und YBCO durch einen STO-Film ändert dieses Verhalten nicht wesentlich. Dieses identifiziert eine magnetische Wechselwirkung zwischen dem Flußliniengitter im YBCO-Film und dem Domänenmuster im LCMO-Film als Ursache des Effekts.

Die dargestellte Arbeit kann nicht als vollständige Abhandlung der Wechselwirkung zwischen Ferromagneten und Hochtemperatur-Supraleitern betrachtet werden, auch nicht für den speziellen Fall von LCMO und YBCO.

Im folgenden werden einige noch offene Fragen angeführt, welche zu weiteren Bemühungen auf diesem Gebiet motivieren sollen:

- Der Abfall des Widerstands im normalleitenden Zustand erscheint bei Quasi-Teilchen-Injektion nahe der Pseudogap-Temperatur T^*. Bei Verwendung von stark unterdotierten YBCO verändert sich T^* erheblich und der Widerstand sollte dies auch.

- Es wird diskutiert, dass eine antiferromagnetische-Phase an der LCMO/YBCO-Grenzschicht existiert. Eine Bestätigung dieser Phase mittels systematischer Austausch wechselwirkung Untersuchungen wäre interessant.

- Eine durch das Substrat hervorgerufene veränderung der Domänenstruktur des Ferromagneten sollte direkt die magnetische Veranherung der Flußlinien-Pinning beeinflussen. Dieses könnte durch Verwendung strukturierter oder “vizinal” geschnittener Substrate für die Heterostrukturen erreicht werden.

Es wurde gezeigt, dass Doppelschichten, welche aus spin-polarisiertem LCMO und Supraleitendem YBCO bestehen, eine Vielfalt neuer physikalischer Phänomene zeigen. Die Übergangstemperaturen T_c und T_Curie, die kritische Stromdichte j_c des Supraleiters und sogar der Normalleitende-Widerstand können durch externe Parameter und/oder die Probengeometrie beeinflusst werden. Diese Doppelschichten sind gute Kandidaten für technische Anwendungen in der Zukunft.

Contents

Chapter 1

Introduction and Motivation

1.1 History

Superconductivity was discovered by HEIKE KAMERLINGH ONNES [1] in Holland in 1911 as a result of his investigations leading to the liquefaction of helium gas. Two years later he got the Nobel prize 1913. In Onnes‘ time superconductors were simple metals like mercury, lead, bismuth etc. [1]. These elements become superconductors only at the very low temperatures of liquid helium. During the 75 years that followed, great studies were made in the understanding of how superconductors work. Over that time, various alloys were found that show superconductivity at somewhat higher temperatures. Unfortunately, none of these alloy superconductors worked at temperatures much more than 23 K. Thus, liquid helium remained the only convenient refrigerant that could be employed with these superconductors.

The transition of a normal metal into the superconducting state is revealed by the total disappearance of the electrical resistance at low temperatures. Indeed, the current in a closed superconducting circuit can circulate forever without damping.

Another fundamental property of the superconducting state was discovered in 1933 when Walther Meissner and his Ph.D. student Robert Ochsenfeld demonstrated that superconductors expel any residual magnetic field [3]. Similarly, superconductivity can be destroyed by applying a magnetic field that exceeds the critical value B_c. Superconductivity and magnetism usually try to avoid each other this feature can be exploited to, for example, levitate a magnet above a superconductor.

The recent discovery of compounds that are both ferromagnetic and superconducting at the same time came as a surprise to experimental and theoretical, condensed matter physicists.

The microscopic theory of superconductivity was created by JOHN BARDEEN,

---

[1] From now on, the names of researchers that were awarded the Nobel Prize will be displayed with capital letters.

LEON COOPER and ROBERT SCHRIEFFER[1] in 1957 [2]. According to this so-called *BCS–theory*, the electrons form pairs, known as Cooper-pairs , due to interactions with the crystal lattice at low temperatures. Electrons in these Cooper-pairs have opposite values of momentum, meaning that the pairs themselves generally have zero orbital angular momentum. Additionally, the angular momenta add up to zero. The formation of Cooper-pairs leads to a superconducting energy gap, which means that single electrons cannot occupy states near the Fermi surface. Such energy gaps which are essentially equal to the energy needed to break up the Cooper-pairs show up clearly as jumps in the specific heat and thermal conductivity at what is known as the critical temperature T_{c}.

Another significant theoretical advancement came in 1962 when BRIAN JOSEPHSON[2], a graduate student at Cambridge University, predicted that electrical current would flow between two superconducting materials, even when they are separated by a non-superconductor or an insulator. His prediction was later confirmed and won him a shared of the 1973 Nobel Prize in Physics with LEO ESAKI and IVAR GIAEVER. This tunnelling phenomenon is today known as the “Josephson effect” and has been applied to electronic devices such as the Superconducting Quantum Interference Device (SQUID), an instrument capabable of detecting even the weakest magnetic fields.

Then, in 1986, a truly breakthrough discovery was made in the field of superconductivity. GEORG BEDNORZ and ALEXANDER MÜLLER [3] researchers at the IBM Research Laboratory in Rüschlikon, Switzerland, created a brittle ceramic compound that showed superconductivity at the highest then temperature known 30 K. What made this discovery so remarkable was that ceramics are normally insulators. They do not conduct electricity well at all. So, researchers had not considered them as possible high-temperature superconductor candidates. The Lanthanum, Barium, Copper and Oxygen ($\mathrm{La}_{1.85}\mathrm{Ba}_{0.15}\mathrm{CuO}_4$) compound that MÜLLER and BEDNORZ synthesized, behaved in a not-as-yet-understood way. The discovery of this first of the superconducting copper-oxides (cuprates) won the 2 men a Nobel Prize the following year. It was later found that tiny amounts of this material were actually superconducting at 58 K, due to a small amount of lead having been added as a calibration standard making the discovery even more noteworthy.

The BCS theory is quite successful at explaining the properties of most classical superconducting materials. But the discovery in 1986 of a new class of materials that are superconducting at high temperatures remains a challenge to the theoreticians, and there is still no unambiguous theoretical explanation for this phenomenon.

The observation of superconductivity in organic conductors, heavy-fermion systems, the ruthenates and, most recently, the new ferromagnetic superconductors provides strong

---

[1] Nobel prize 1972

[2] Nobel prize 1973

[3] Nobel prize 1987

arguments for the existence of more exotic types of superconductivity. Indeed, pairing in ferromagnets must result from a different type of electron-pairing. In these materials, electrons with spins of the same direction are paired up with each other to form Cooper-pairs with one unit of spin, resulting in so-called ***triplet superconductivity***. In contrast, conventional superconductivity, also known as ***s*–wave** singlet superconductivity, occurs when electrons with opposite spins bind together to form Cooper-pairs with zero momentum and spin.

A magnetic field can destroy singlet superconductivity in two ways. The first of those effects is known as the *orbital effect* and is simply a manifestation of the Lorentz force. Since the electrons in the Cooper-pair have opposite momenta, the Lorentz force acts in opposite directions and the pairs break up. The second phenomenon, known as the *paramagnetic effect*, occurs when a strong magnetic field attempts to align the spins of both the electrons along the field direction. Such fields, however, do not wreck triplet superconductivity because the spins of both electrons may point in the same direction as the field. This means that triplet superconductivity can only be destroyed by the orbital effect.

Ferromagnetism arises when a large number of atoms or electrons align their spins in the same direction. There are actually two sources of magnetism in metals, localized magnetic moments and the “sea” of conduction electrons. Local magnetism occurs in rare-earth metals (such as gadolinium) due to the incomplete filling of electrons in the inner atomic shells. This leads to a well defined magnetic moment at every fixed atomic site, which in turn produces long-range magnetic coupling due to the exchange of conduction electrons.

The second type of magnetism known as band magnetism, (such as ruthenium) arises from the magnetic moments of the conduction electrons themselves. In a metal, the electrons are “itinerant”, that is they are free to move from one atomic site to another, and they tend to align their magnetic moments in the direction of an applied field.

Ferromagnets only have a net magnetic moment at low temperatures; the internal magnetic field spontaneously appears at the so called *Curie temperature*, which is typically in the range 10–1000 K. At higher temperatures, however, the magnetic moments of the atoms continually change their direction so that the net moment is zero. A similar magnetic transition occurs in antiferromagnetic materials in which the spins of neighboring atoms point in opposite directions. This transition takes place at the *Néel temperature* and leads to the disappearance of the internal magnetic field.

Although superconductivity and magnetism seem to be antagonistic phenomena, could they co-exist in the same compound? This question was first posed by the Russian theorist VITALY GINZBURG[4] in 1957, but early experiments in 1959 by Bernd Matthias, demonstrated that a very small concentration of magnetic rare-earth impu-

---

[4] Nobel prize 2003

rities, even a few percent, was enough to completely destroy superconductivity when ferromagnetic ordering was present.

The origin of this destructive phenomenon is a quantum mechanical interaction between the spins of the electrons and the atomic magnetic moments. Below the superconducting transition temperature, this "exchange interaction" attempts to align the Cooper-pairs . Exchange interactions therefore place stringent limits on the existence of superconductivity.

- ***But can superconductivity and ferromagnetism co-exist?***

The answer to this question is much more fascinating. Finally, the discovery of ferromagnetism ($T_{\mathrm{Curie}} \approx 135$ K) and superconductivity ($T_{\mathrm{c}} \approx 40$ K) in the $\mathrm{RuSr_2GdCu_2O_8}$ (Ru1212) compound opens a lot of questions. Such as the coupling of the ferromagnetic layers between the superconducting layers without killing the superconductivity. Also, the existence of superconductivity and ferromagnetism in the same unit cell. It was demonstrated that, superconductivity in these ferromagnet materials, could be explained by the Larkin-Ovchinnikov-Fulde-Farrell–(LOFF) theory.

When a superconductor is in contact to a normal metal , a number of phenomena occurs such as the *proximity effect*. The two materials influence each other on a spatial scale of the order of the coherence length (ξ_{sc}) in the vicinity of the interface. In particular, the correlations between quasiparticles of the superconducting state are induced into the normal metal, Cooper-pairs penetrate into the normal metal with a finite life time. Until they decay into two independent electrons, they preserve the superconducting properties. Alternatively, the proximity effect can be viewed as resulting from a fundamental process known as Andreev-reflection. Imagine a low energy electron propagating from the normal metal onto the interface with the superconductor. A single electron can penetrate the superconductor only if its energy is larger than the superconducting energy gap ($E_{\mathrm{el-nm}} > \Delta_{\mathrm{sc}}$). Below this energy only Cooper-pairs can exist. Thus low energy electrons can not penetrate into the superconductor and are reflected back as holes, while Cooper-pairs are transferred into the superconductor.

When a superconductor is in contact to a ferromagnet another important phenomenon occurs, the *inverse*–proximity effect (or the so called spin diffusion length ξ_{fm}). The exchange energy (J_{spin}) of the ferromagnet quenches the Andreev-reflections, due to the absence of available states for the reflected holes with different spin. This prevents the Cooper-pairs to diffuse deeply into the ferromagnet layer. In addition, the quasiparticles using the exchange energy as a driving force to break the Cooper-pairs in the superconductor within the inverse proximity effect scale (ξ_{fm}). ξ_{fm} can strongly depend on the type of the ferromagnet , it is rather small for classical ferromagnets, much larger in materials that show the colossal magnetoresistance (CMR) effect.

1.2 Motivation

After the more fundamental aspects of superconductivity now the particular issues are discussed that became subject of the thesis.

Although the investigation of the proximity effect in superconductor /normal metal (SN) systems was started about 40 years ago, the technology allowing to produce and measure experimental samples of mesoscopic dimensions was achieved much more recently. In particular, it became possible to study superconductor /normal metal structures consisting of thin layers (having thicknesses smaller than the coherence length). Such structures behave as a single superconductor with nontrivial properties. Many of them have already been studied for the case of ideally transparent interfaces. At the same time, the experimental progress requires the corresponding advances in theory, especially taking into account arbitrary interface transparency. This crucial parameter determines the strength of the proximity effect and at the same time is not directly measurable. From the practical point of view, the superconductor /normal metal proximity structures can be used as superconductors with relatively easily adjustable parameters, in particular, the energy gap and the critical temperature. The parameters of the proximity structures can be tuned, e.g., by varying the thicknesses of the layers. This method has already found its application in superconducting transition edge bolometers and photon detectors for astrophysics.

The physics of superconductor /ferromagnet systems is even richer. In contrast to the superconductor /normal metal case, the superconducting order parameter does not simply decay into the *non*–superconducting metal but it can also oscillate. This behavior is due to the exchange energy J_{spin} of the conduction quasiparticles . In the classical ferromagnet (J_{spin} $\approx$1 eV) it acts as a potential of different signs for two electrons in Cooper-pairs and leads to a finite momentum of the pair. These oscillations reveal themselves in a *non*–monotonic dependence of the critical temperature T_{c} of superconductor /ferromagnet systems as a function of the thickness of the ferromagnet layers, both in the cases of superconductor /ferromagnet superlattices and bilayers. At the same time, in most of the papers investigating this effect, the methods to calculate T_{c} were approximate.

So far, the oscillation of T_{c} in the superconductor /colossal magnetoresistance bilayers or superlattices was not found. This can be explained due to the high-exchange energy of colossal magnetoresistance materials (J_{spin} $\approx$3 eV). This high exchange energy J_{spin} not only quenches the oscillation of T_{c} but also the Andreev-reflection as mentioned before. This high exchange energy can also act as driving force for the quasiparticles to tunnel into the superconducting layer, called *spin-polarized* quasiparticles self injection. Although such effects have been studied before, it was often done in the simplest models and simplest assumptions about the system parameters. To achieve a better understanding of these phenomena, one should study them at various conditions and determine the physical mechanisms behind the effect.

A possible practical application of ferromagnet /superconductor /ferromagnet heterostructures uses spin-dependent properties of high-T_c superconductors that can lead to the design of new superconducting devices such as "spintronic devices", like transistors with high gain current and high speed. "Spintronics" means the exploitation of the spins of the electrons rather than their charge. Spin controlled solid state devices based on the giant magnetoresistance (GMR) effect are already realized in read-out heads of hard disks. Further challenges in the field of spintronics that are addressed by experiments and theory include the optimization of electron–spin life times and the detection of the spin coherence length in nanoscale structures. Although the superconducting spintronics are not yet experimentally realized, the work in this direction has already started. Using the classical ferromagnet as source for spin–polarized quasiparticle injection into *s*-wave superconductors in the superconducting state was started more than 30 years ago. To achieve better understanding of this phenomenon, colossal magnetoresistance electrodes with full spin polarization are used to inject spin-polarized quasiparticles injection into *d*-wave superconductor . This experiment is now done under various conditions to study the physical mechanisms both in the superconducting and in the normal state of the superconductor.

For a complete description of these heterostructures also the physics of the flux line lattice in the superconductor has to be considered. High-temperature superconductors are extreme type-II superconductors containing Abrikosov flux lines in a large range of applied fields between B_c1= 0.01 T and $B_\mathrm{c2} >$ 100 T. Apart from their high-transition temperatures of T_c = 90 K to 133 K, HTSC differ from conventional superconductors by their short coherence length ξ_sc, a large magnetic penetration depth λ, a pronounced material anisotropy and a layered structure. These four properties drastically enhance the thermally activated depinning of flux lines. Small ξ_sc reduces the pinning energy. Large λ softens the flux-line lattice. The layered structure of HTSC causes fascinating novel phenomena, a flux line is now a string of 2D "pancake vortices" in the superconducting $\mathrm{CuO_2}$ layers. In case of heterostructures of HTSC and ferromagnets now an additional interaction between the flux line lattice and the domain structure of the ferromagnet has to be taken into account. This will lead to new effects that are also discussed in this thesis.

1.3 Outline of the thesis

In Chapter (2) a comprehensive presentation of the theoretical background used in the work will be given. This addresses topics such as Ginzburg-Landau theory (GL-theory) and BCS–theory for classical superconductors , also the theoretical approximations that can be used to deal with high–T_c materials. Especially the role of flux line pinning in presence of ferromagnetic layer is discussed.

In Chapter (3) a comprehensive presentation of the theoretical background for colossal magnetoresistance is given.

A brief summary of the fundamentals of proximity–effect and spin–diffusion length estimation in normal-metal/superconductor and ferromanet/superconductor bilayers will also be included in Chapter (4).

- As already mentioned, several experimental techniques are applied in this work. Their underlying theory and the experimental apparatuses will be described in Chapter (5). More specifically, the instrumentation and theory of magneto–optical (MOP) Faraday effect will be explained.

- The structural analysis of all of the heterostructures is the main part of Chapter (6). The roughness of layers after the growth is analyzed by atomic–force–microscopy (AFM). The results allow statements of the growth mechanisms. Detailed informations about the lattice parameters and oxygen stoichiometry are found in x-ray diffraction investigation. One important issue is the morphology of the interface. This addressed by high–resolution transmission electron microscopy.

- Spin–diffusion length determination will be one of the topics of Chapter (7), Section (7.1), where two series of experimental data on CMR/HTSC bilayers grown on two different single crystalline substrates STO and LSGO will be presented and analyzed with the help of the theory described in Chapter (2). The role of the diffusion of the spin–polarized quasiparticles will allow to extract some interesting relations between the temperature dependence of the quasiparticle density n_{qp}(T) and the order parameter band gap in the cuprates. Additionally, the spin diffusion length ξ_{fm} is derived from the results.

- Section (7.2) concerns injection of spin–polarized quasiparticles (SPQI) in the normal and superconducting state of YBCO. As mentioned in the previous section, the spin–polarized quasiparticles of the magnetic layer can be self–injected into a superconducting layer. In case of an injection the quasiparticles have additional energy to penetrate into the YBCO layer. This method can be used to measure the effect of a polarization enhancement in the CuO_2–plane around the so called pseudogap temperature T^* in the normal state of the superconducting layer. Also, the effects of SPQI in the superconducting state will be shown. As counter experiment several junctions will be shown using different sources for quasiparticle injection. Non–polarized and lower–polarized quasiparticles will be injected into the YBCO in the normal and superconducting states.

- In Section (7.3) the critical current density j_{c} in superconductor /ferromagnet heterostructures is investigated. From quantitative magneto–optical measurements and SQUID magnetization data it is found that the critical current density in a superconducting film is strongly affected by the presence of the ferromagnet . First, a substantial reduction of j_c is found, second a strong dependence of j_c on the magnetization state of the ferromagnet . This result can be explained in terms of additional pinning of the flux lines by the domain structure of the ferromagnet .

- Last but not least, in Chapter (8) the summary of the work of this thesis is presented and an outlook of possible extensions of this work is given.

Chapter 2

Theoretical background

2.1 Introduction

Conventional superconductors are metals in their normal states, and their transport properties are well described by Fermi liquid theory.

The cuprate high temperature superconductors (HTSC) [4] are “bad metals” with strong electron correlation with a normal state that can not be described by Fermi liquid theory. There is compelling evidence that they are better thought of as doped Mott-insulators, rather than as high temperature strongly interacting versions of conventional metals. The cuprate superconductors exhibit numerous types of low temperature ordering which interact strongly with the superconductivity, the most prominent being antiferromagnetism and the unidirectional charge and spin density wave “stripe” order. These orders can compete or coexist with superconductivity. Furthermore, whereas phase fluctuations of the superconducting order parameter are negligibly small in conventional superconductors, fluctuation effects exist in the high-T_c superconductors because of their much smaller superfluid stiffness.

Apparently, this does not influence the fundamental character of the superconducting order parameter. It is still a charge $2e$ scalar field, although it transforms according to a nontrivial representation of the point group or symmetry of the crystal. It is a “*d*-wave superconductor”. At low temperature and energy there is every reason to expect that the physics is dominated by nodal quasiparticles that are similar to those that one might find in BCS-superconductors of the same symmetry. Indeed, there is considerable direct experimental evidence that this expectation is realized. However, the Fermi liquid theory fails to describe the normal state. Especially around the so-called ***pseudogap*** temperature T^* competing orders are present. This fact requires an entirely different approach to understand most of the physics. It is the purpose of this Chapter to address the basic physics of classical and high-temperature superconductivity.

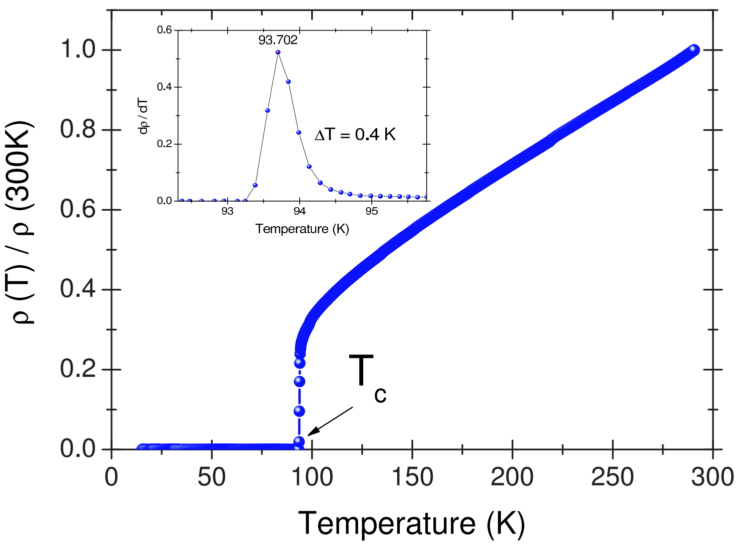

Figure 2.1: Temperature dependence of the resistivity of a thin film of the high-T_c superconductor $YBa_2Cu_3O_{7-\delta}$.

2.2 What is a superconductor?

Superconducting materials have two fundamental properties:

- **No dc-resistivity (ρ = 0 for all $T \leq T_c$):** Zero resistivity $\rho = 0$, i.e. infinite conductivity, is observed in a superconductor at all temperatures below the critical temperature T_c , as depicted in Fig. 2.1. However, if the passing current is higher than the critical current j_c , superconductivity disappears. *Why is the resistivity of a superconductor zero?* If a superconducting metal like Al or Hg is cooled below the critical temperature T_c , the gas of repulsive individual electrons that characterizes the normal state transform itself into a different type of fluid, a quantum fluid of highly correlated pairs of electrons. A conduction electron of a given momentum and spin gets weakly coupled with another electron of the opposite momentum and spin. These pairs are called *Cooper pairs*. The coupling energy is provided by lattice elastic waves, called *phonons*. The behavior of such a fluid of correlated Cooper pairs is different from the normal electron gas. They all move in a single coherent motion. A local perturbation, like an impurity, which in the normal state would scatter conduction electrons (and cause resistivity), cannot do so in the superconducting state without immediately affecting the Cooper pairs that participate in the collective superconducting state. Once this collective, highly coordinated, state of coherent "super-electrons" (Cooper pairs) is set into motion (like the supercurrent induced around the loop), its flow is without any dissipation. There is no scattering of 'individual' pairs of the coherent fluid, and therefore no resistivity.

- **No magnetic induction (B = 0 inside the superconductor):** In magnetic fields lower the critical field B_c the magnetic inductance becomes zero inside the superconductor when it is cooled below T_c . The magnetic flux is expelled from the interior of the superconductor (see Fig. 2.2). This effect is called the Meissner-Ochsenfeld effect after its discoverers [3]. To test whatever a material is superconducting both properties $\rho = 0$ and $B = 0$ must be present simultaneously.

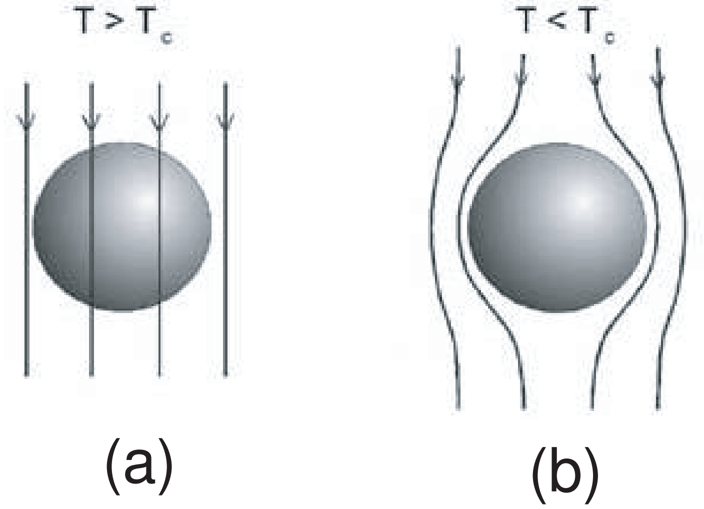

Figure 2.2: Expulsion of a weak external magnetic field from the interior of the superconducting material.

2.2.1 Normal metal vs. superconductor

In this section a discussion is presented about the origin of electrical resistivity in the normal metal and contrast it with the absence of resistivity in the superconductor. An introduction to the basic concept of the superconducting wave function is given which will be used throughout the whole Chapter. Then showing that the Meissner effect can be described by the London model and is another distinct characteristic property of the superconducting state.

2.2.1.1 Description of the normal state

A normal metal consists of a regular crystalline lattice of positively charged ions and a gas of free, non-interacting conduction electrons that fill the space between the ions. If there is typically one electron per ion, this means 10^{23} electrons/cm^3. As the electrons are of opposite charge as the ions, the total charge is balanced and at equilibrium, the model-metal is electrically neutral. If we apply an electric field as an external perturbation to the gas of free electrons within the metal, the external force will accelerate the electrons and create a current flow of “free” electrons. As the ions are arranged in perfectly regular array, they do not scatter conduction electrons at T = 0[1]. The scattering of electrons at T = 0 is actually caused by deviations from the ideal periodic potential of the lattice, i.e., by impurities, imperfections in periodicity like dislocations. Since every real metal contains some imperfections and impurities, one observes some finite resistivity at very low temperatures. This resistivity, extrapolated to T = 0, is called residual resistivity, ρ_{i}. As we increase the temperature, the electrons also get scattered by thermal vibrations of the lattice (called phonons) so the resistivity rises with temperature. This contribution is called phonon resistivity, ρ_{ph}. Therefore the temperature dependance of resistivity of a good metal can be described as : ρ(T) = ρ_{i} + ρ_{ph}. This is empirical Matthiessen's rule and provides a basis for understanding the resistivity of metal at low temperature.

In order to derive a simple expression for the residual resistivity of the metal, first some characteristic quantities of the normal state should be considered. At T = 0 the maximum kinetic energy of an electron inside the metal is called Fermi energy (E_{F}). It is related to the number of carriers per unit volume, n, by the simple relation: $E_{\mathrm{F}} = \frac{\hbar}{2m}(2\pi^2 n)$, where $\hbar$ is the Planck constant and m is the mass of the electron. The Fermi energy of a typical metal is of the order of electron volts (see Table 2.1).

Table 2.1: Some characteristic quantities of the normal state of classical and high-T_{c} superconductor materials.

Material	n [10^{23} cm^{-3}]	ν_F [10^6 ms^{-1}]	ℓ [nm]	ρ(100 K) [$\mu\Omega$cm]
Al	180	2	130	0.3
Nb	56	1.4	29	3
$La_{1.85}Sr_{0.15}CuO_4$	5	0.1	∼5	∼100
$YBa_2Cu_3O_{7-\delta}$	7	0.1	∼10	∼60

Conduction electrons of maximum energy, E_{F}, propagate with the Fermi velocity υ_{F} related to the Fermi momentum P_{F} by $P_{\mathrm{F}} = m\upsilon_{\mathrm{F}}$. We have $E_{\mathrm{F}} = \frac{1}{2}P_{\mathrm{F}}\upsilon_{\mathrm{F}}$. We also define the Fermi wave vector, k_{F}; as in quantum mechanics a wave is always associated with a particle by de-Broglie relation $P_{\mathrm{F}} = \hbar k_{\mathrm{F}}$. The conduction electrons that propagate through the crystal with a characteristic Fermi velocity υ_{F} are scattered by impurities or lattice imperfections. This gives rise to resistivity. Between two scattering events an electron covers on average a characteristic distance ℓ_{e}, called the electron mean free path. The resistivity ρ_{i} of a metal, according to the Drude model, is given by

$$\rho_i = \frac{m\upsilon_F}{ne^2\ell_e} \tag{2.1}$$

---

[1] If the crystal was perfect, at T = 0, the electron waves would propagate without scattering and there would be no resistivity, i.e., conductivity of an ideal crystal at T = 0 should be infinite.

where e and m represent the charge and mass of the electron. In isotropic metals, the conductivity is equal to the inverse of the resistivity; both quantities are tensors in the anisotropic case. Equation (4.1) shows that in the normal state of a given metal the resistivity is inversely proportional to the electron mean free path. The shorter the average distance between the scattering events the higher is the resistivity. The introduction of impurities into a metal obviously reduces ℓ_e and increases ρ_i. This can be clearly seen in Table (2.1), in which typical values for ρ and ℓ_e for several superconducting materials are presented.

2.2.2 The superconducting state

The electrical dc-resistivity in superconductors is zero for temperatures below the critical temperature T_c . So, one can apply a dc electrical current (supercurrent) without energy dissipation. Let us see what happens in a supercondcting state and what are its characteristic properties compared with the normal state taken Al as an example for classical superconductor material. In the normal state above the critical temperature (T_c = 1.1 K) Al is a good conductor and behaves just like an ideal metal or like copper which exhibits no superconducting behavior down to the lowest temperature. Its conduction electrons behave like a gas of nearly free electrons that are scattered by lattice vibrations, lattice imperfections, etc..which contributes to the resistivity. However, when Al is cooled below T_c , its dc-resistance abruptly vanishes, the resistivity is zero. One natural question is, what happens to the scattering of conduction electrons which contributed to the resistivity in the normal state? Why does it disappear? A satisfactory explanation to these questions can be given only within the rather involved quantum mechanical description of the microscopic BCS-theory, which shall be briefly discussed in next section.

When Al is cooled below the critical temperature T_c , the gas of the “repulsive” individual electrons that characterizes the normal state transforms itself into a different type of fluid. A quantum fluid of highly correlated pairs of electrons (in the reciprocal, momentum space, not in a real space). Below T_c a conduction electron of a given momentum and spin gets weakly coupled with another electron of exactly the opposite momentum and spin. These pairs are called ***Cooper pairs***. The glue is provided by the elastic waves of the lattice, called *phonons*. One can visualize this attraction by a real-space picture. As the lattice consists of positive ions, the moving electron creates a lattice distortion. Due to the heavy mass of lattice ions, this positively charged distortion relaxes slowly and is therefore able to attract another electron. The ’distance’ between the two electrons of the Cooper pair, called the ***coherence length***, ξ, is large in classical superconductor materials. It has a value ξ = 1600 nm in pure Al, ξ = 38 nm in pure Nb, for example. The coherence length ξ is very small in high-T_c superconductors, it has a value of $\xi_\mathrm{ab} \approx$ 16 nm, and ξ_c $\approx$ 0.3 nm in $La_{1.85}Sr_{0.15}CuO_4$ and $YBa_2Cu_3O_{7-\delta}$. So while the “partners” in the Cooper pair are far apart, the other nearest electrons (belonging to other Cooper pairs of the collective state) are only a few nanometer away. The behavior of such a fluid of correlated Cooper pairs is different from the normal electron “gas”. The electrons which form the pair have opposite momenta (and opposite spins), so the net momentum of the pair is zero.

2.2.3 Superconducting state and wave function

The Cooper pair has twice the charge of a free electron, $q = 2e$. The electrons are fermions and obey the Fermi-Dirac statistics and the Pauli exclusion principle which allows only one electron in a given quantum state. Cooper pairs are quasi-bosons, obey the Bose-Einstein statistics and are allowed to be ***all*** in the same state. In contrast to the normal metal in which each electron has its own wave function, in a superconductor, all Cooper pairs are described by the single wavefunction

$$\Psi(r) = \sqrt{n_s}(r) \exp i\varphi(r) \tag{2.2}$$

where n_s(r) can be considered as the number of “superconducting electrons” (Cooper pairs), $\Psi(r)\Psi^*(r)$ = n_s(r) and $\varphi(r)$ is a spatially varying phase.

In optics, a beam of photons, being all in the same state, i.e., traveling with the same velocity, can be described by a plane wave, $\exp(ikr - iwt)$ and the gradient of the phase is related to the momentum of the particle by the de-Broglie relation, $P = \hbar k$, or $v = \frac{\hbar}{m}\nabla\varphi$. As all Cooper pairs are in the same state, we have an analogous situation and the gradient of the phase becomes a macroscopic quantity, a quantity proportional to the current flowing in the superconductor.

2.2.4 The Meissner-Ochsenfeld Effect

In addition to zero resistivity (i.e., infinite conductivity), the superconductor exhibits another striking property: it expels the magnetic field from its interior. This is not a consequence of infinite conductivity, it is another intrinsic characteristic property of the superconducting state which shall now be discussed in some detail. As already illustrated in Fig. 2.2, in the normal state at temperatures above T_c the field lines pass through the metallic specimen. Upon cooling below T_c , a phase transition into the superconducting state takes place and the magnetic flux gets expelled out of the interior of the metallic sample. The Meissner-Ochsenfeld effect [3] cannot be deduced from the infinite conductivity of a superconductor. The exclusion of the magnetic field from the interior of a superconducting specimen is a direct evidence that the superconducting state is not simply one of zero resistance. If it were so, then a superconductor cooled in the magnetic field through T_c would have trapped the field in its interior. When the external field is removed, the induced persistent eddy currents would nevertheless preserve the trapped field in the interior of the specimen. The expulsion of the flux therefore implies that this new superconducting state is a true thermodynamic equilibrium state. The above argument can be proved by a few elementary formulae of electrodynamics. Consider Ohm's law, $V = RI$, written as $E = \rho j$, where E represents the electric field, ρ the resistivity and j the electrical current density in the sample. Zero resistivity implies zero electric field. So, if we take the Maxwell equation

$$\mathrm{curl} E = -\frac{\partial B}{\partial t}, \tag{2.3}$$

we have

$$\frac{\partial B}{\partial t} = 0. \tag{2.4}$$

We see that the magnetic induction in the interior of the sample has to be constant as a function of time. The final state of the sample would have been different if it were cooled under an applied external field or if the field were applied after the sample has been cooled below T_c . In the former case the field would have remained within the sample, while in the latter it would have been zero. For the specimen to be in the same thermodynamic state, independent of the precise sequence that one uses in cooling or in applying the field, the superconducting metal always expels the field from its interior, and has $B = 0$ in its interior. So the expulsion of the magnetic field ensures that the superconducting state is a true thermodynamic state.

2.2.5 London theory

F. and H. London [5] started with the idea that one has to modify the usual electrodynamic equations in order to describe the Meissner effect; of course Maxwell equations always remain valid. Thus, it is Ohm's law that has to be modified. In order to do that, they used a two-fluid model. Of the total density n of electrons, there is a fraction n_s that behaves in an abnormal way and represents superconducting electrons. These are not scattered by either impurities or phonons, thus they do not contribute to the resistivity. They are freely accelerated by an electric field. If $\vec{v}_\mathrm{s}$ is their velocity, the equation of motion can be written as

$$m\frac{\partial \vec{v}_s}{\partial t} = e\vec{E}. \tag{2.5}$$

We can now define a superconducting current density

$$\vec{J} = n_s e \vec{v}_s. \tag{2.6}$$

which obeys the following equation:

$$\frac{\partial \vec{J}}{\partial t} = \frac{n_s e^2}{m} \vec{E}. \tag{2.7}$$

Using the Maxwell equation, $\mathrm{curl}\vec{E} = -\mu_\circ \vec{H}$, in which we replaced the magnetic induction $\vec{B}$, which varies on the macroscopic scale, by the local microscopic field $\vec{H}$ ($\vec{B}$ is an average of microscopic $\mu_\circ \vec{H}$) we obtain:

$$\frac{\partial}{\partial t}(\mathrm{curl}\vec{J} + \frac{\mu_\circ n_s e^2}{m}\vec{H}) = 0. \tag{2.8}$$

F. and H. London noticed that with Ohm's law and an infinite conductivity, equation (2.8) leads to $\partial \vec{H}/\partial t$ = 0. An infinite conductivity only implies that the magnetic field cannot change, which is contrary to the experimental evidence. Thus they integrated equation (2.8) and took the following particular solution:

$$\mathrm{curl}\vec{J} + \frac{\mu_\circ n_s e^2}{m}\vec{H} = 0. \tag{2.9}$$

This is the London equation which describes the electrodynamics of a superconductor. We now show that it leads to the flux expulsion, the definition of the penetration depth (λ_L), and a relation between the supercurrent ($\vec{J_s}$) and the vector potential ($\vec{A}$). In order to show how it leads to the Meissner effect, we take the Maxwell equation

$$\vec{J} = \mathrm{curl}\vec{H} \tag{2.10}$$

By applying the curl-operator to both sides and combining with equation (2.9), we obtain

$$\mathrm{curl}\,\mathrm{curl}\vec{H} + \mu_\circ \frac{n_s e^2}{m}\vec{H} = 0 \tag{2.11}$$

or

$$-\Delta\vec{H} + \mu_\circ \frac{n_s e^2}{m}\vec{H} = 0 \tag{2.12}$$

This equation enables one to calculate the local field inside the superconductor and it is another expression of the London equation. Below we show a simple example of the Meissner effect.

Planar superconductor/vacuum interface:

Writing equation (2.12) for a one-dimensional problem, we get

$$\frac{d^2H}{dx^2} = \frac{H}{\lambda^2} \qquad \text{where} \quad \lambda^2 = \frac{m}{\mu_\circ n_s e^2} \tag{2.13}$$

If we consider a uniform, infinite superconductor in the region $x > 0$ and apply the magnetic field $H_\circ$ parallel to the surface, the field inside the superconductor is given by the solution of this equation:

$$H = H_\circ \exp(\frac{-x}{\lambda_L}) \tag{2.14}$$

The field vanishes in the interior of the superconductor (Fig. 2.2). λ_L is the London penetration depth that measures the extension of the penetration of the magnetic field inside the superconductor.

It shows that, in order to have zero field within the bulk of the material, one must have a sheet of superconducting current which flows close to the surface and which creates an opposite field inside the superconductor that cancels the externally applied magnetic field. Therefore equation (2.12) describes well the Meissner effect.

2.3 The Ginzburg-Landau theory

The London theory is not applicable to situations in which the number of superelectrons, n_s, varies; it does not link n_s with the applied field or current. Therefore we need a more general framework which relates n_s to the external parameters. This is the approach of the Ginzburg-Landau theory [6] which uses the general (Landau) theory of second order phase transitions by introducing the corresponding an order parameter.

2.3.1 Ginzburg-Landau free energy

The basis of this description is the intuitive idea that a superconductor contains superconducting electrons with density n_s and non-superconducting electrons with density $n - n_\mathrm{s}$, where n is the total density of electrons in the metal. Ginzburg and Landau have chosen to use a kind of a wave function, to describe the superconducting electrons. This function is a complex scalar, equation (4.2):

$$\psi(r) = \mid \psi(r) \mid \exp i\varphi(r) \tag{2.15}$$

and is called the order parameter. It has the following properties:

- Its modulus $\mid \psi^* \psi \mid$ can be interpreted as the number of superconducting electrons n_s at a point r.

- As in quantum mechanics, the phase φ(r) is related to the supercurrent that flows through the material below T_{c} .
- $\psi \neq 0$ in the superconducting state, but ψ = 0 in the normal state.

Furthermore, Ginzburg and Landau have used the following form of the Helmholtz function:

$$F_s(r,T) = F_n(r,T) + \alpha \mid \psi(r) \mid^2 + \frac{\beta}{2} \mid \psi(r) \mid^4 + \frac{1}{2m} \mid (-i\hbar\nabla - 2e\vec{A})\psi \mid^2 + \frac{\mu_\circ \vec{H}^2}{2} \tag{2.16}$$

$$F_s(T) = \int_V F_s(r,T) d^3r \tag{2.17}$$

where s and n denote the superconducting and normal state, while $\hbar$ is Planck's constant and V is the volume of the sample.

In order to see the advantage of using complex functions in describing superconductivity we rewrite equation (2.17) using the modulus and phase of the order parameter; hence we get

$$F_s(r,T) = F_n(r,T) + \alpha \mid \psi(r) \mid^2 + \frac{\beta}{2} \mid \psi(r) \mid^4 + \frac{\hbar^2}{2m}(\nabla \mid \psi \mid)^2 + \frac{1}{2} \mid \psi \mid^2 m\vec{V}_s^2 + \frac{\mu_\circ \vec{H}^2(r)}{2} \tag{2.18}$$

where

$$\vec{V}_s = \frac{1}{m}(\hbar\nabla\phi - 2e\vec{A}) \tag{2.19}$$

One can see that we have obtained the Landau expansion plus the free energy of the field and the current. If the order parameter does not vary in space, one gets back exactly to the London free energy and London equation by carrying out the minimization. If there is no magnetic field and the order parameter has no phase, one obtains the usual Landau equation. The Ginzburg-Landau free energy is thus the way to introduce the London idea in the usual second order phase transition.

Equation (2.16) introduces two phenomenological parameters, α and β, in the free energy. The fourth term in equation (2.16) is the energy associated with variations of ψ in space. It is written as if representing a true quantum mechanical wave function; $\vec{A}$(r) is the vector potential at a point r and $\vec{H}$ is the microscopic field at the same point. As it is known from electromagnetism: $\mu_\circ\vec{H}$ = curl$\vec{A}$. The Helmholtz energy is the integral over the total volume of the sample of the energy density that depends on the point of consideration. As in the Landau theory one takes

$$\alpha = a(T - T_c), \ \ \beta = \textbf{positive} \quad \text{constant}, \quad \text{independent of} \quad \text{T}. \tag{2.20}$$

2.3.2 Ginzburg-Landau equations

In order to determine the order parameter ψ(r) and the vector-potential $\vec{A}$(r) we minimize the Helmholtz free energy with respect to ψ(r) and $\vec{A}$. By this double minimization one gets two equations named after their authors, Ginzburg-Landau (GL) equations:

$$\alpha\psi + \beta \mid \psi \mid^2 \psi + \frac{1}{2m}(i\hbar\nabla - 2e\vec{A})^2\psi = 0 \tag{2.21}$$

$$\vec{J} = \mathrm{curl}\vec{H} = \frac{e}{m}[\psi(i\hbar\nabla - 2e\vec{A})\psi + c.c.] \tag{2.22}$$

These two equations are coupled and should therefore be solved simultaneously. The first one gives the order parameter ψ(r) while the second enables one to describe the supercurrent that flows in the superconductor.

2.3.2.1 Magnetic penetration depth λ

If we now apply a small magnetic field and assume that we can neglect the variations of ψ(r) , the second Ginzburg-Landau equation (2.22) gives:

$$\vec{J} = \mathrm{curl}\vec{H} = -\frac{4e^2}{m}\vec{A} \mid \psi \mid^2 \tag{2.23}$$

Taking

$$\frac{1}{\lambda^2} = 4e^2\frac{\mid \psi \mid^2}{m}\mu_\circ \tag{2.24}$$

one obtains the London equation. λ is the London penetration depth which is already defined within the London model, if we put n_s = 4$\mid \psi \mid^2$.

2.3.2.2 Coherence length ξ

Considering the first Ginzburg-Landau equation (2.21) in one-dimensional case without external magnetic field:

$$-\frac{\hbar}{2m}\frac{\partial^2\psi}{\partial x^2} + \alpha\psi + \beta \mid \psi \mid^2 \psi = 0 \tag{2.25}$$

this equation defins the length scale

$$\xi^2(T) = \frac{\hbar^2}{2m \mid \alpha \mid} \tag{2.26}$$

The solution of this equation depends only on x/ξ(T). This length is called the coherence length and represents the length over which the order parameter ψ(r) varies, when one introduces a perturbation at some point. This length also diverges when T $\rightarrow T_{\mathrm{c}}$, because of $\alpha \rightarrow$0.

2.3.2.3 Ginzburg-Landau parameter

If both characteristic lengths λ and ξ diverge at T in the same manner as $\mid \alpha \mid^{-1/2}$, their ratio κ, which is called the Ginzburg-Landau parameter, does not depend on temperature:

$$\kappa = \frac{\lambda}{\xi} \tag{2.27}$$

Actually κ is the only parameter that really appears in Ginzburg-Landau equation. One can distinguish two different situations for κ:

- If $\kappa < \frac{1}{\sqrt{2}}$ the superconducting material is a ***type-I*** superconductor.
- If $\kappa > \frac{1}{\sqrt{2}}$ the superconducting material is ***type-II*** superconductor. A detailed concern of this issue is presented in next the section.

2.4 Types of superconducting materials

Below T_{c} , the superconducting state has a lower free energy than in the normal state but it requires the expulsion of the flux. This costs some magnetic energy which has to be smaller than the condensation energy gained in undergoing the phase transition into the superconducting state (i.e., by forming the coherent ensemble of Cooper pairs from the “random” electron gas). Obviously, if we begin to increase the external magnetic field it will reach the point where the cost in magnetic energy will outweigh the gain in condensation energy and the superconductor will become partially (in a particular sample geometry) or totally normal. Superconductivity disappears and the material returns to the normal state if one applies an external magnetic field of strength greater than some critical value B_{c}, called the critical thermodynamic field. The superconducting state can also be destroyed by passing an excessive current through the material, which creates a magnetic field at the surface of strength equal to or greater than B_{c}. This limits the maximum current that the material can sustain and is an important problem for applications of superconducting materials.

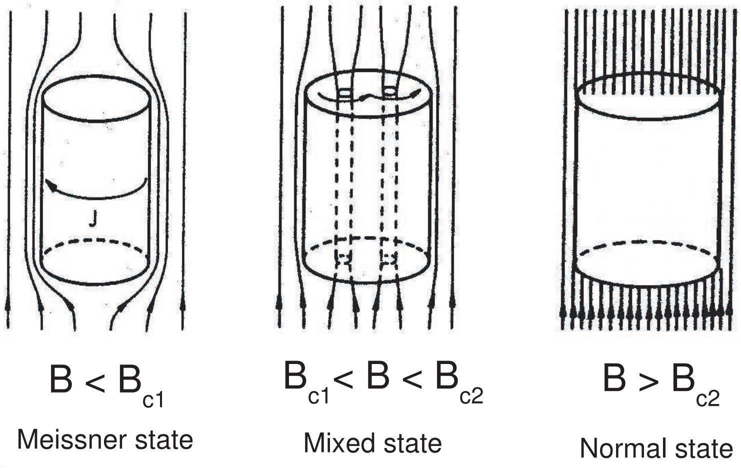

Figure 2.3: Flux penetration in the mixed state.

2.4.1 Type-I superconductors

Superconducting materials that completely expel magnetic flux until they become completely normal are called ***type-I*** superconductors. With the exception of V and Nb, all superconducting elements and most of their alloys in the “dilute limit”, are type-I superconductors. The strength of the applied magnetic field required to completely destroy the state of perfect diamagnetism in the interior of the superconducting specimen is called the thermodynamic critical field B_c. As schematically shown in Fig. 2.4, the variation of the critical field B_c with temperature for type-I superconductor is approximately parabolic:

$$B_\mathrm{c} = B_\circ(1 - \frac{T}{T_c}) \tag{2.28}$$

where $B_\circ$ is the extrapolated value of B_c at T = 0. $B = \mu_\circ(H + M)$, where M is the magnetization and $\mu_\circ = 4\pi \times 10^{-7}$. The Meissner effect, $B = 0$, corresponds to $M = -H$. Above the critical field B_c, the material becomes normal, so $M = 0$. The negative sign shows that the sample becomes a perfect diamagnet that excludes the flux from its interior by means of surface currents.

2.4.2 Type-II superconductors

For a type-II superconductor there are two critical fields. The lower B_c1 and the upper B_c2. The flux is completely expelled only up to the field B_c1. So, in applied fields smaller than B_c1, the type-Il superconductor behaves just like a type-I superconductor below B_c. Above B_c1 the flux partially penetrates into the material until the upper critical field, B_c2, is reached. Above B_c2 the material returns to the normal state (see Fig. 2.5). Between B_c1 and B_c2 the superconductor is said to be in the mixed state. The Meissner effect is only

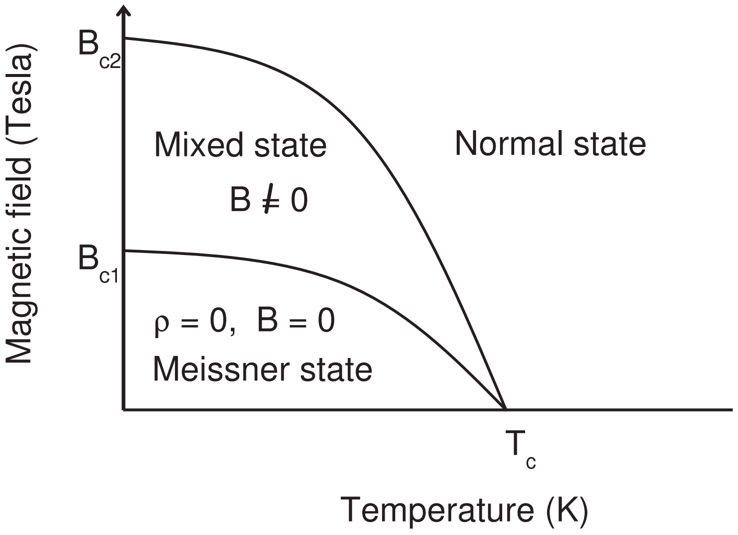

Figure 2.4: Variation of critical fields, B_{c1} and B_{c2} as a function of temperature. The upper critical field B_{c2} can be very high above 100 T in case of high-T_c superconducting material.

partial. For all applied fields $B_{c1} < B < B_{c2}$, magnetic flux partially penetrates the superconducting specimen in the form of tiny microscopic filaments called vortices Fig. 2.3. The diameter of a vortex in conventional superconductors is typically 100 nm. It consists of a normal core, in which the magnetic field is large, surrounded by a superconducting region in which flows a persistent supercurrent which maintains the field within the core (see Fig.2.7). Each vortex carries a magnetic flux $\Phi_\circ = \frac{h}{2e} = 2.067\times10^{-15}$ Tm^2 where h is Planck constant and e is the electron charge. The magnetic induction B is directly related to n, the number of vortices per $B = n\Phi_\circ$.

Superconductivity can and does persist in the mixed state up to the upper critical fields of B_{c2} which is sometimes higher than 60 Tesla or even 150 Tesla in high-T_c superconductors .

2.5 Bardeen-Cooper-Schrieffer theory

In 1957, BARDEEN, COOPER, and SCHRIEFFER (BCS) proposed a general microscopic theory of superconductivity that quantitatively predicts many properties of superconductors and is now widely accepted as providing a satisfactory explanation of the phenomenon [2]. There are various levels of approximation in which the BCS-theory has been applied. The mathematical underpinning of the BCS-theory is so complex that it will not be of much benefit to summarize its general formulation, so this section will emphasize predictions that are often compared with experiments. These predictions arise mainly from the homogeneous, isotropic, phonon-mediated, square well, *s*-wave coupling simplification of the BCS-theory, and many superconductors, to a greater or lesser extent,

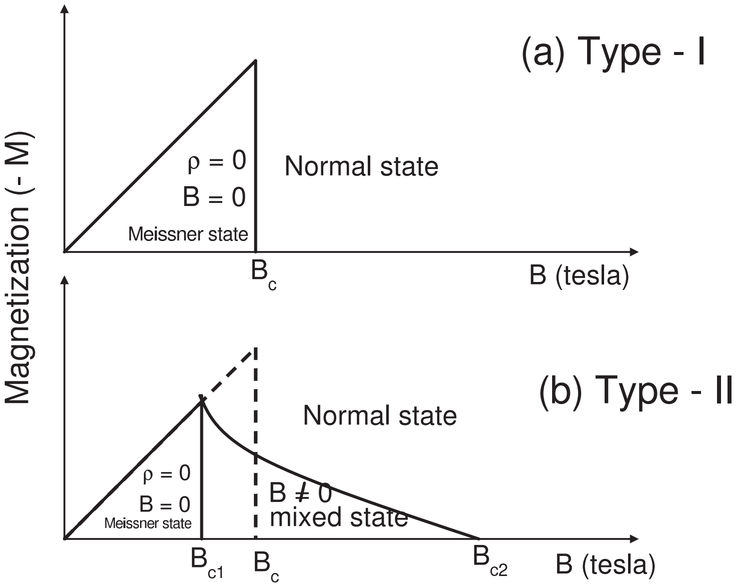

Figure 2.5: Variation of magnetization as a function of the magnetic field for type-I and type-II superconductor .

have been found to satisfy these predictions. Some of them are as follows: The isotope effect involves the claim that for a particular element the transition temperature T_c depends on the mass M of the isotope as follows:

$$M^\alpha T_c = \text{const.} \tag{2.29}$$

The weak coupling BCS limit gives the value α = 1/2, which has been observed in some superconducting elements, but not in all of them.

A superconductor has an energy gap $E_\mathrm{g} = 2\Delta(k)$, which is assumed to be independent of wave vector k, and for this assumption the energies in the normal and superconducting states are

$$E(\epsilon) = \epsilon \quad \text{normal state} \quad \text{and} \quad E(\epsilon) = (\epsilon^2 + \Delta^2)^{1/2} \quad \text{superconducting state} \tag{2.30}$$

where ϵ is the energy in the absence of a gap measured relative to the chemical potential μ:

$$\epsilon = \frac{\hbar^2 k^2}{2m} - \mu \tag{2.31}$$

The density of states $D(E)$ given by (with E = 0 in the center of the gap)

$$= \frac{D_n(E)}{(E^2-\Delta^2)^{1/2}}, \qquad E > \Delta \tag{2.32}$$

$$D_s(E) \qquad = 0 \qquad -\Delta < E < \Delta \tag{2.33}$$

$$= \frac{-D_n(E)}{(E^2-\Delta^2)^{1/2}}, \qquad E < \Delta \tag{2.34}$$

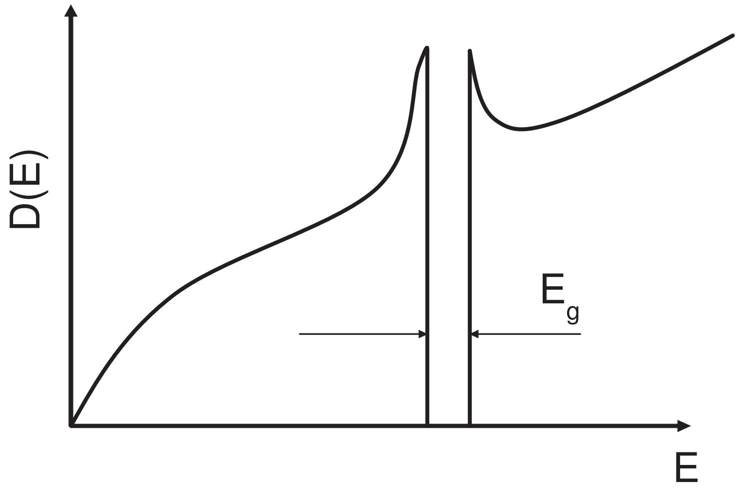

Figure 2.6: Energy dependence of the density of states D(E) in the presence of an energy gap.

is shown plotted in Fig. 2.6, where the normal electron density of states $D_n(E)$ is assumed to have the constant value $D_n(0)$ in the neighborhood of the gap.

Consider a square-well electron-electron potential $V_\circ$ and an energy gap Δ(k) that is equal to $\Delta_\circ$ in the neighborhood of the Fermi surface,

$$\Delta(k) = \Delta_\circ, \qquad -\hbar\omega_D \leq \epsilon(k) \leq \hbar\omega_D, \tag{2.35}$$

and is zero elsewhere. The Debye frequency ω_D determines the range of ϵ because it is assumed that Cooper pair formation is mediated by phonons. The energy gap $\Delta_\circ$ in this approximation is given by

$$\Delta_\circ = \frac{\hbar\omega_D}{\sinh[\frac{1}{V_\circ D_n(0)}]} \tag{2.36}$$

In the weak coupling (small $V_\circ$) limit,

$$V_\circ D_n(0) \ll 1, \qquad k_B T_c \ll \hbar\omega_D. \tag{2.37}$$

we obtain the dimensionless ratios

$$\frac{E_g}{k_B T_c} = \frac{2\Delta_\circ}{k_B T_c} = \frac{2\pi}{\exp\gamma} = 3.52, \tag{2.38}$$

where γ = 0.5772 is the Euler-Mascheroni constant. This ratio approximates experimental measurements that have been made on many superconductors. The dimensionless electron-phonon coupling constant λ is related to the phonon density of states $D_{ph}(\omega)$ through the Eliashberg expression [7]:

$$\lambda = 2\int_0^\infty \frac{\alpha(\omega)D_{ph}(\omega)}{\omega}d\omega. \tag{2.39}$$

Superconductors are characterized as having weak ($\lambda \ll$1), intermediate ($\lambda \approx$1), and strong ($\lambda \gg$1) coupling. The electron-electron interaction potential $V_\circ$ for Cooper pair bonding has an attractive electron-phonon part measured by λ and a repulsive screened Coulomb part μ_c^* to give $V_\circ D_n(0) = \lambda - \mu_c^*$ and this provides the well known formula for the critical temperature T_c :

$$T_c = 1.13\theta_D \exp[\frac{-1}{\lambda - \mu_c^*}] \tag{2.40}$$

where θ_D is the Debye temperature related to ω_D by $\hbar\omega_D$ = $k_B\theta_D$. θ_D ranges from 100 K to 500 K. This range of θ_D (and $\lambda - \mu_c^* \approx$ 0.3) implies a maximum BCS value of $T_c \sim$ 25 K.

A number of related formulae for the dependence of T_c on λ and μ_c^* have appeared in the literature, e.g., the McMillan equation [8].

$$T_c = \frac{\theta_D}{1.45}\exp[\frac{-1.04(1+\lambda)}{\lambda - \mu_c^*(1+0.62\lambda)}] \tag{2.41}$$

The BCS theory predicts that at T_c there is a jump in the electronic specific heat from its normal state value $C_e = \gamma T$ to its superconducting state value C_s given by

$$\frac{C_s - \gamma T_c}{\gamma T_c} = 1.43 \tag{2.42}$$

In the free electron approximation the electronic specific heat coefficient γ depends on the Fermi temperature T_F and the gas constant R through the expression $\gamma = \frac{\pi^2 R}{2T_F}$.

Below T_c , the BCS-theory predicts that the specific heat C_s(T) depends exponentially on the inverse temperature,

$$Cs(T) = a\exp[\frac{-\Delta}{k_B T}] \tag{2.43}$$

where $\Delta = 1.76k_B T_c$, and a is a constant.

2.5.1 Cooper–pairs and $T_{\rm c}$

There are three levels of explanation of the nature of superconductivity that are commonly called BCS. One is the general formulation that does not specify particular interactions. The second is the phonon-mediated version of the theory, in which phonons play the role of bringing about the coupling together of two electrons to form Cooper pairs. The third level, which was described in the original formulation of the theory and provided the results summarized previously. Further it assumes the simplification of an isotropic, homogeneous material with a square-well electron-electron interaction potential involving a phonon coupling mechanism and *s*-wave singlet-state pairing. The superconducting elements, which are almost all type-I, as well as many classical type-II superconductors, are looked upon as phonon-mediated *s*-state types. Pairing mechanisms involving the exchange of particles other than phonons, such as excitons or antiferromagnetic spin fluctuations, have been proposed for non-classical superconductors. In particular, no consensus exists yet about the pairing mechanism of the cuprates, although *d*-wave pairing seems to be favored, another very recently results appears to support the phonon mediated in high-$T_{\rm c}$ superconductivity [9].

2.6 An isolated vortex

Each vortex carries one quantum of flux, $\Phi_\circ = \frac{h}{2e}$. Therefore the number of vortices gradually increases as the field is raised from $B_{\rm c1}$ to $B_{\rm c2}$. Qualitatively, the upper critical field, $B_{\rm c2}$, corresponds to the case where the distance between vortices is equal to the radius of the normal core of the vortex. Near $B_{\rm c1}$, the distance between the vortices is $a_\circ = \sqrt{\frac{2\Phi_\circ}{\sqrt{3}B}}$. The vortices repel each other and it is this magnetic pressure that determines the vortex density. As the field increases, the magnetic pressure and the number of vortices increase. The density of vortices per unit surface n is related to B by the important relation $B = n\Phi_\circ$.

This enables one to calculate the distance between the vortices as a function of B. In order to study the flux penetration we start with a description of an isolated vortex (see Fig.2.7). We consider the most interesting practical limit where $\xi \ll \lambda$, which is the case for high-$T_{\rm c}$ superconductors . In that limit, $\kappa \gg$1, the second Ginzburg-Landau equation takes the simple form (2.22) when the order parameter is constant, e.g. $r > \xi$, namely over all except a small core region of radius. In order to describe the fact that the vortex has a central core of radius ξ (see Fig.2.7) and carries a flux $\Phi_\circ$ we transform equation (2.22) into

$$H + \lambda^2 \,\mathrm{curl}\,\mathrm{curl} H = \frac{\Phi_\circ}{\mu_\circ}\delta_{(r)} \tag{2.44}$$

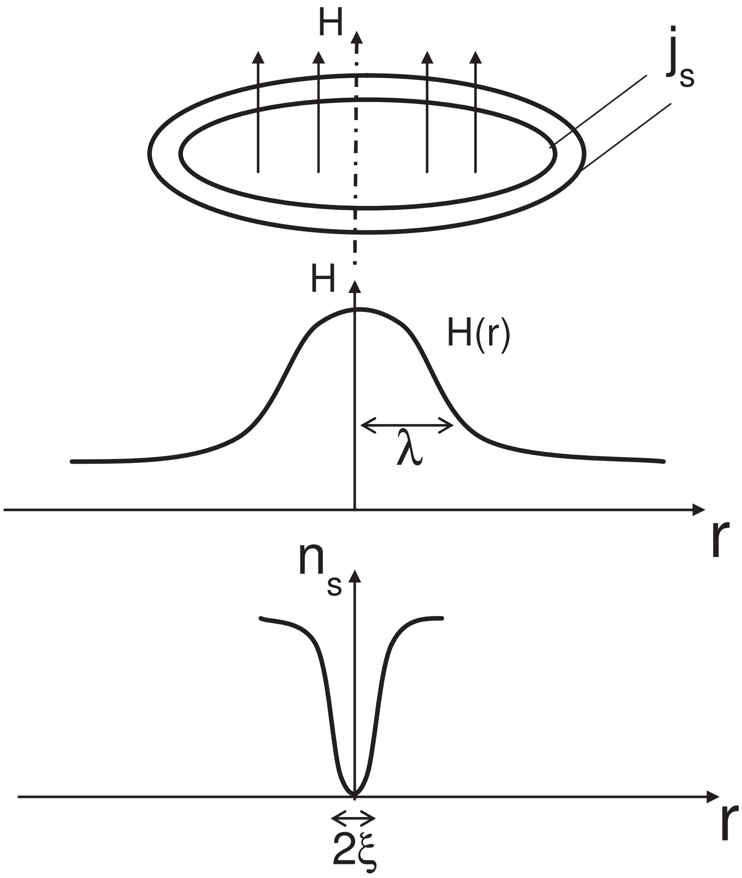

Figure 2.7: The cross section of an isolated vortex in type-II superconductor .

where δ(r) describes a singularity in the plane perpendicular to the field direction at r = 0 and imposes a flux of $\Phi_\circ$ per vortex. By solving equation (2.44) one finds how the field decreases from the center of the vortex:

$$H(r) = \frac{\Phi_\circ}{2\pi\mu_\circ}(\frac{r}{\lambda_L})\exp(\frac{-r}{\lambda_L}) \tag{2.45}$$

Note, that in case of HTSC the magnetic size of a vortex is much bigger than the vortex core, due to the fact that $\lambda \gg \xi$.

2.6.1 Pinning of vortices

Normally, one would think that the critical currents create the field B_{c2} at the surface of the sample. Actually the critical currents correspond rather to those that generate the field B_{c1}, and not B_{c2}. Why does B_{c1} play a role? Because above B_{c1}, there are vortices in the material as we have seen before.

The current displaces the vortices and this creates a non-desirable energy dissipation. The vortex in motion creates an electric field $E = \frac{d\Phi_\circ}{dt}$. In presence of this field, the current j dissipates energy $\varepsilon = E.j$. This energy dissipation is equivalent to resistivity.

Theoretically, critical currents of type-II superconductors are weak; still weaker for small values of $B_{\rm c1}$ compared with $B_{\rm c1}$ which is rather large. So, how does one pass intense currents without dissipation above $B_{\rm c1}$?

The answer is that one has to prevent the motion of vortices so that the critical current would not be limited by $B_{\rm c1}$. This is achieved by the so-called ***vortex pinning*** (or flux pinning). How does one pin the vortex? Simply by creating sites out of which the vortex cannot leave without large energy increase. For example, in conventional type-II materials one can find small inclusions of normal metal imbedded in the superconductor. The vortex will be pinned to such an inclusion as it does not have to spend energy to destroy superconductivity in that inclusion. What is the typical size of efficient inclusions? Evidently the coherence length ξ, the diameter of the tube which is in the normal state within the vortex, see Fig 2.7. Inhomogeneities over distances of the order of the coherence length are therefore responsible for the attainment of very high currents in some materials like Nb-Ti.

In high-$T_{\rm c}$ superconductor where the coherence length is very short $\xi \approx$ 1.5 nm, it is not obvious how to control the vortex pinning sites. Practically all technologically interesting materials like Nb compounds, or high-$T_{\rm c}$ superconductor are type-II superconductors. The reason for this is that the creation of vortices keeps the magnetic energy smaller than the condensation energy, so the overall free energy of the mixed superconducting state remains (thermodynamically) more favorable than the normal state even up to high magnetic fields. Since the supercurrent can flow in the mixed state through the superconducting regions between vortices, type-II superconductors allow one to construct wires needed for high field magnets.

The pinning force per unit volume $F_{\rm p}$, is related to the measured critical current by $F_{\rm p} = j_{\rm c}B$.

It does not say anything about the mechanism of pinning nor how to increase the value of the critical current. Even j is not related to the pinning force of an individual vortex $f_{\rm p}$. Thus if we want to increase $F_{\rm p}$, we have first to make the link with the pinning force on an individual vortex $f_{\rm p}$, and then study the mechanism which can pin an individual vortex line.

We assume random inhomogeneities in the bulk of the sample, which we call pinning points. These objects will be described by an interaction potential with a vortex line. The pinning points are inhomogeneities which can either favor or inhibit the pair condensation responsible for superconductivity, i.e., which repel or attract flux lines.

The first problem that we will deal with is the way these point interactions between flux lines and pinning points add to determine the pinning force density $F_{\rm p}$. So, one attempt is to write $F_{\rm p} = Nf_{\rm p}$, where N is the number of interactions between pinning points and vortices. This is not correct in general. Indeed, consider that we have a rigid lattice of vortices and random inhomogeneities. We would have no pinning at all. The reason stems from the fact that the pinning forces are randomly oriented and statistically canceled. One can also understand this result by considering the fact that the interaction energy in an infinite medium would be independent of the relative position of the rigid lattice of flux lines and the random array of pinning centers. As pinning effectively occurs an explication is needed. It is essential to pinning processes that the lattice can be deformed. In this case the total energy of the system is lowered by deformation of the lattice and pinning may occur if an energy increase is required to move the lattice with respect to the pinning array. It should be also mentioned the opposite limit, i.e., if we have no lattice but a liquid of vortices. In that case we have also $j_c = 0$ because we would need to pin each vortex in order to prevent it from moving. Thus the lattice stiffness is central to the pinning problem. It is necessary to be able to describe the rigidity of the lattice. In order to understand the effects of the pinning centers.

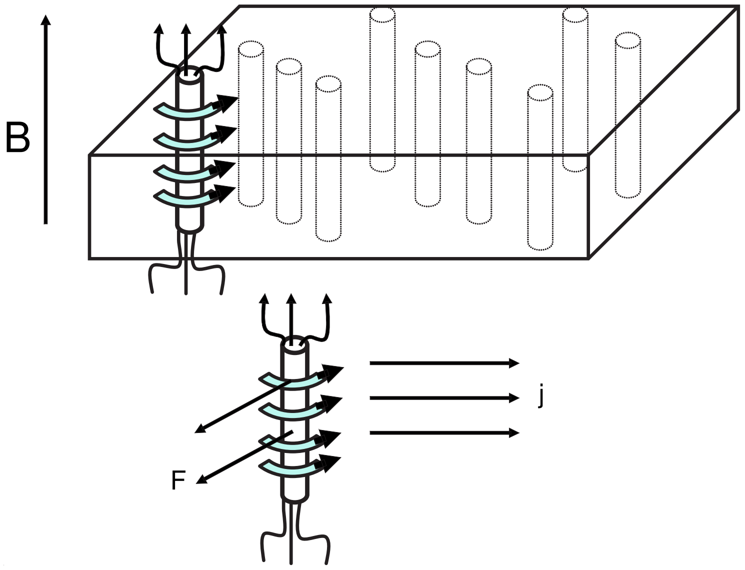

Figure 2.8: Schematic diagram of the mixed state. The vortices form a hexagonal lattice. The Lorentz force F on the flux line in the presence of the current j, is shown below.

$$\varepsilon_L = \int [\underbrace{\alpha(|\,\psi\,|^2 - |\,\psi_\circ\,|^2) + \frac{\beta}{2}(|\,\psi\,|^4 - |\,\psi_\circ\,|^4)} + \underbrace{\frac{1}{2m^*}\,|\,\hat{p}\psi\,|^2} + \underbrace{\frac{1}{2\mu_\circ^2}} B^2]\partial^2 r \tag{2.46}$$

The local variation of the flux line energy creates potential landscape, see Fig. 2.8, has the form in equation (2.46). It consists of three terms:

- *First*: condensation energy : varying on ξ.
- *Second*: kinetic energy: varying on λ and ξ.
- *Third*: magnetic energy: varying on λ.

Table 2.2: Year of discovery and critical temperature T_c of some oxide superconductors.

Year		Materials	T_c (K)
1964		NbO	1
1964		TiO	2
1964	doped	$SrTiO_{3-x}$	0.7
1965	bronzes	K_xWO_3	6
1966	bronzes	K_xMoO_3	4
1969	bronzes	K_xReO_3	4
1974		$LiTi_2O_4$	13
1975		$Ba(Pb,Bi)O_3$	13
1986		$La_{1.85}Sr_{0.15}CuO_4$	38
1987		$YBa_2Cu_3O_{7-\delta}$	93
1988		$Tl_2Ba_2Ca_2Cu_3O_{10}$	125
1994		$HgBa_2Ca_2Cu_3O_{8+\delta}$	133

Usually the enhancement in the pinning force due to the magnetic pinning plying a minor role. Especially in the high-T_c superconductor materials. Nevertheless in this work it will be shown that it can also play a role in the enhancement of the pinning force.

2.7 High-T_c superconductors

In this section an introduction to the field of high-T_c superconducting (HTSC) oxides is given. This will be followed by the phase diagram and the crystal structure of $YBa_2Cu_3O_{7-\delta}$ as an example for HTSC materials. More details about the normal state of HTSC will be presented, especially, around the so-called pseudogap temperature T^* in the generic phase diagram of the cuprates.

Most of the superconducting compounds that were discussed so far were metals. It was reasonable to look for superconductivity in that kind of materials and most research has been done on intermetallic compounds. Some oxide superconductors were known for decades (see Table 2.2), but their transition temperatures were rather small.

Two known exceptions were $LiTi_2O_4$ and $Ba(Pb,Bi)O_3$ with critical temperatures of T_c = 13 K. This was unusual as their densities of carriers were also very small. The breakthrough came in 1986 when GEORG BEDNORZ and ALEX MÜLLER (IBM-Zurich) [4], in their systematic search for new superconductors in metallic Ni and Cu-oxides, observed an evidence for a resistive superconducting transition (with an onset at $T_{c-onset}$ = 30 K) in a fraction of their $La_{1.85}Ba_{0.15}CuO_4$ sample. This led to the discovery of $La_{1.85}Sr_{0.15}CuO_4$ withT_c = 38 K and subsequently to $YBa_2Cu_3O_{7-\delta}$ with T_c = 93 K.

Table 2.3: Critical temperatures of some HTSC compound.

Compound	T_c (K)
$La_{2-x}M_xCuO_{4-y}$	38
M = Ba, Sr, Ca	
$x \sim 0.15$, y small	
$Nd_{2-x}Ce_xCuO_{4-y}$ (electron doped)	30
$Ba_{1-x}K_xBiO_3$ (isotropic, cubic	30
$Pb_2Sr_2Y_{1-x}Ca_xCu_3O_8$	70
$R_1Ba_2Cu_{2+m}O_{6+m}$	
R: Y, La, Nd, Sm, Eu, Ho, Er, Tm, Lu	
m = 1 (123)	93
m = 1.5 (247)	95
m = 2 (124)	82
$Bi_2Sr_2Ca_{n-1}Cu_nO_{2n+4}$	
n = 1 (2201)	10
n = 2 (2212)	85
n = 3 (2223)	110
$Tl_2Ba_2Ca_{n-1}Cu_nO_{2n+4}$	
n = 1 (2201)	85
n = 2 (2212)	105
n = 3 (2223)	125
$HgBa_2Ca_{n-1}Cu_nO_{2n+2+\delta}$	
n = 1 (1201)	95
n = 2 (1212)	125
n = 3 (1223)	133
n = 4 (1234)	127
n = 5 (1245)	110
n = 6 (1256)	91
n = 7 (1267)	85

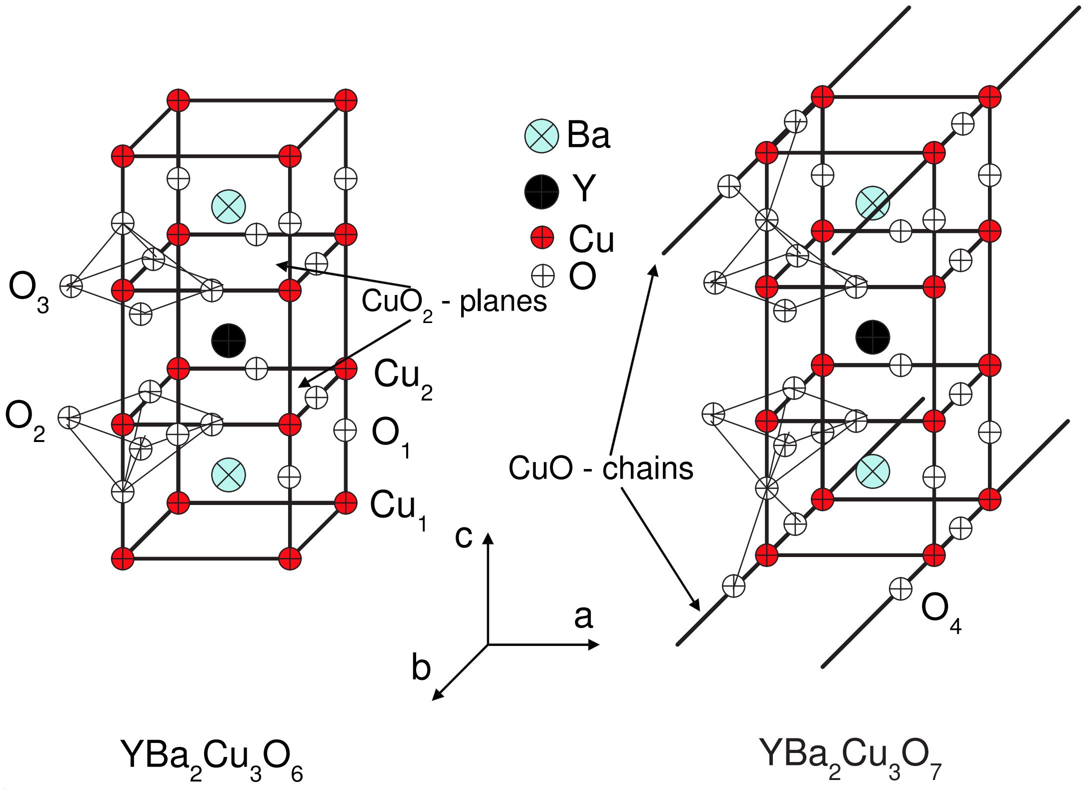

Figure 2.9: Schematic diagrams of $YBa_2Cu_3O_6$ (left) an insulator and $YBa_2Cu_3O_7$ (right) a superconducting oxide.

2.7.1 $YBa_2Cu_3O_{7-\delta}$

In this section first the most important properties of the $YBa_2Cu_3O_{7-\delta}$ superconductor will be discussed, initially from a materials and subsequently from a physics point of view.

- ***i)High-T_c oxides are highly anisotropic, layered structures:*** Except for some materials (like $Ba_{1-x}K_xBiO_3$), most high-T_c superconducting oxides are cuprate compounds. One of their characteristics is the presence of CuO_2 layers which dominate most of the properties. A look at the schematic structure of $YBa_2Cu_3O_{7-\delta}$ presented in Fig. 2.9, shows that it is highly anisotropic. The unit cell is developed from that of a tetragonal perovskite tripled along the c-axis and it consists of a sequence of copper-oxygen layers. The dimensions of the unit cell are approximately 1.2 nm and 0.4 nm in the c and a or b-axis directions respectively. The fact that the unit cell consists of layers of copper oxides will be one of great importance for understanding the physical properties.

- ***ii) Metallic oxides:*** The second important characteristic of these oxides is their metallic behavior, as shown in Fig. 2.1. While most oxides are insulating materials, HTSC oxides exhibit a metal-like conductivity. The room temperature conductivities in a- or b-axis direction of the cuprate crystal are of the same order of magnitude as the conductivities of some disordered metallic alloys. Only the conductivity perpendicular to CuO_2-planes is much smaller.

- ***iii) Ceramic materials:*** The original materials, $La_{1.85}Sr_{0.15}CuO_4$ and $YBa_2Cu_3O_{7-\delta}$, were synthesized as ceramic pellets. One mixes the correct ratio of constituent oxides, grinds and sinters them, makes a pellet, and following a calcining procedure at annealing temperature of $T_{\rm a} \approx$ 950°C and cools it down in oxygen.

  As typical ceramics, high-$T_{\rm c}$ superconducting oxides also contain grains, grain boundaries, twins, and other imperfections. Even some of the best thin films may consist of grains a few microns in diameter; all these are mostly detrimental to high critical current densities that are required for applications. It is important to emphasize that even the best single crystals of HTSC oxides often contain various defects and imperfections like oxygen vacancies, twins and impurities. These imperfections are not only very relevant to their physical properties but possibly even essential for their basic thermodynamic stability. It may well turn out that various imperfections found in HTSC crystals are intrinsic to these materials. In general, it is important to understand that the materials science of HTSC oxides is a non-trivial pursuit and that the understanding of phase diagrams (especially around the pseudogap temperature T^{*}), crystal chemistry, preparation and stability of these oxides is still not completely understood.

2.7.1.1 The phase diagram of $YBa_2Cu_3O_{7-\delta}$

The schematic structure of $YBa_2Cu_3O_6$, given in Fig. 2.9, represents an insulator. It has to be doped to gradually become a hole-doped metallic conductor and a superconductor below some critical temperature, as shown in Fig. 2.1. The doping is achieved by adding additional oxygen which forms CuO chains. These oxygen ions attract electrons from the CuO_2-planes which therefore become metallic (see Fig. 2.10). Note, that the correct formula for YBCO material is $YBa_2Cu_3O_{6+{\rm x}}$, where x corresponds to partial oxygen content:

- for 0.0 < x < 0.4, $YBa_2Cu_3O_{6+{\rm x}}$ is an insulator.
- for 0.4 <x < 1.0, $YBa_2Cu_3O_{6+{\rm x}}$ is a superconductor.

The schematic phase diagram of a cuprate high-$T_{\rm c}$ superconductor is given in Fig. 2.10, as a function of temperature and x the density of doped holes per CuO_2-plane. The solid lines represent phase transitions into the antiferromagnetic (AFM) and superconducting (SC) states. The dashed line marks the opening of a pseudogap (PG) around the temperature T^{*}. The latter crossover is not sharply defined and there is still a debate on its position and the physics behind.

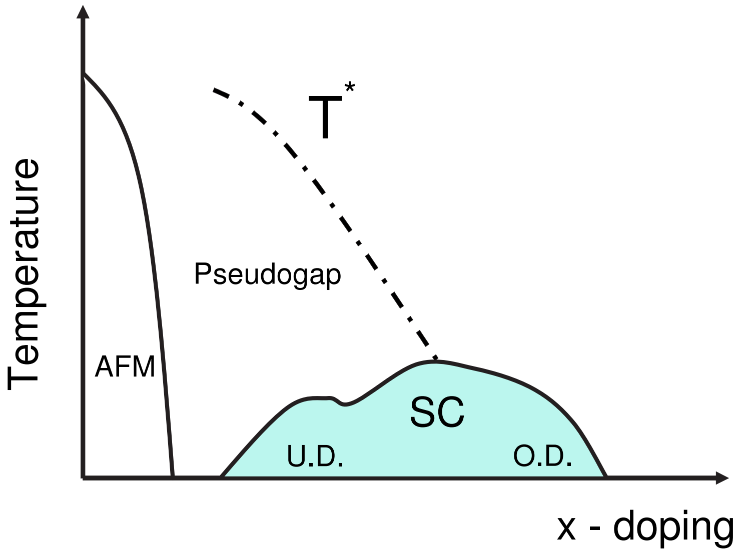

Figure 2.10: Schematic phase diagram of YBCO as a function of temperature and x the density of doped holes per CuO_2-plane. The solid lines represent phase transitions into the antiferromagnetic (AFM) and superconducting (SC) states. The dashed line marks the opening of a pseudogap (PG) around the temperature T^*.

The parent state of each family of HTSC is an antiferromagnetic Mott-insulator with one hole (and spin 1/2) per CuO_2-plane. These insulators are transformed into superconductors by introducing a concentration, x, of doped holes into the CuO_2-planes. As a function of increasing x, the antiferromagnetic transition temperature is rapidly suppressed to zero, then the superconducting transition temperature rises from zero to a maximum and then drops down again (see Fig. 2.10). Where T_c is an increasing function of x, the materials are underdoped (U.D.). They are optimally doped where T_c reaches its maximum, and they are overdoped (O.D.) for larger x. In the underdoped regime there are a variety of crossover phenomena observed at temperatures above T_c . These phenomena are associated with the opening of a *pseudogap*. There are various families of high temperature superconductors, all of them have the same nearly square shaped copper-oxide planes, but different structures in the regions between the planes. One characteristic that seems to have a fairly direct connection with T_c is the number of copper-oxide planes that are close enough to each other that interplane coupling may be significant; T_c seems generally to increase with the number of planes within a homologous series, at least as one progresses from single layer to bilayers, to trilayers materials, see Table 2.3.

The following comments concerning the phase diagram of YBCO hold in a similar way also for the all HTSC families listed in Table (2.3):

- ***Oxygen content***: The oxygen content can be changed reversibly from 6.0 to 7.0 simply by pumping oxygen in/out of the parallel chains of CuO running along the b-axis of Fig. 2.9. $YBa_2Cu_3O_6$ is an insulating antiferromagnet (I-AFM). Increasing the oxygen from YBCO$_{6.4}$ makes the crystal metallic, nonmagnetic and superconducting, T_c = 0+ for YBCO$_{6.64}$.

- ***Higher*** T_c ***:*** The order of magnitude of T_c of YBCO or all HTSC oxides [listed in Table (2.3)] are much higher compared to T_c of the classical superconductor materials . T_c for Nb$_3$Ge is *only* 23 K, the critical temperature corresponds to the binding energy $k_B T_\mathrm{c}$ needed to hold Cooper pairs together in the superconducting state. The fact that $T_\mathrm{c} \sim$ 100 K, i.e. 2Δ = 60 meV, as compared with < 1 meV in conventional superconductors, surprise theorists interested in the microscopic mechanism of high-T_c superconductivity. The critical temperatures of the most extensively studied high-T_c oxide superconductors (HTSC) are shown in Table (2.3).

- ***Short coherence length*** ξ***:*** Very short coherence length, $\xi \approx$ 1.0 nm. If we recall the BCS-derived formula, $\xi \sim \frac{v_F}{k_B T_c}$, we can immediately expect somewhat shorter coherence lengths in HTSC oxides due to their higher T_c 's. However, due to the low density of carriers in HTSC oxides? The Fermi velocity in these ionic metals is also lower than in normal metals. This results in a very short coherence length, $\xi \approx$ 1.0 nm, which is comparable to the size of the unit cell, and it has profound consequences for the physics of HTSC oxides. Actually, the coherence length is different for different crystallographic directions and it was experimentally found in YBa$_2$Cu$_3$O$_{7-\delta}$ that ξ_ab and ξ_c are 1.5 nm and 0.4 nm, respectively. The ξ_c is roughly equal to the interlayer distance and shorter than the corresponding unit cell length, which clearly poses some conceptual problems. As we shall see, these remarkably short coherence lengths dominate all material-related properties and cause a rather complex mixed state. Short coherence length also implies that HTSC oxides are type-II superconductors with very high upper critical fields B_c2.

2.7.2 The pseudogap temperature T^*

the pseudogap is one of the most prominent, and most discussed features of the cuprate superconductors. It is widely observed in underdoped cuprates and, to various extents, in optimally and even slightly overdoped materials or below T_c in case of electron doped cuprates [10]. Among the experimental probes which are used to locate the pseudogap temperature in different materials are:

1) Angle-resolved photoelectron spectroscopy (ARPES) and *c*-axis tunneling: There is a suppression of the low energy single particle spectral weight at temperatures above T_c as detected, primarily, in *c*-axis tunneling [11] and ARPES [12] experiments. The scale of energies and the momentum dependence of this suppression are very reminiscent of the *d*-wave superconducting gap observed in the same materials at temperatures well below T_c . This is highly suggestive of an identification between the pseudogap and some form

of local superconducting pairing.

2) Cu-NMR: There is a suppression of low energy spin fluctuations as detected primarily in Cu-NMR [13]. In some cases, two rather different temperature scales are deduced from these experiments. An upper crossover temperature, at which a peak occurs in the real part of the uniform spin susceptibility (i.e. the Knight shift), and a lower crossover temperature.

3) Resistivity: There is a significant deviation [14,15] of the resistivity in the ab-plane from the linear temperature dependence which is universally observed at high temperatures. A pseudogap temperature is then identified as the point below which dρ/dT deviates significantly from its high temperature value. In some cases, a similar temperature scale can be inferred from a scaling analysis of the Hall resistance, as well. The pseudogap also appears in *c*-axis resistivity, although in a somewhat different manner [16, 17]. In this direction, the pseudogap results in a strong increase in resistivity, reminiscent of the behavior of a narrow gap semiconductor. If we imagine that the *c*-axis transport is dominated by tunneling events between neighboring planes, it is reasonable that a bulk measurement of ρ_c will identify the pseudogap in the same way as the *c*-axis tunneling does.

4) Specific heat: There is a suppression of the expected electronic specific heat [18]. Above the pseudogap scale, the specific heat is generally found to be linear in temperature, $C_V = \gamma T$, but below the pseudogap temperature, C_V/T begins to decrease with decreasing temperature. Interestingly, since the value of above the pseudogap temperature appears to be roughly doping independent.

5) Infrared conductivity: There is an anomalous motion of infrared spectral weight to low energies [19, 20]. The pseudogap is most clearly identified by plotting [20] the frequency dependent scattering rate, defined either as

$$\frac{1}{\tau(\omega)} = \frac{\omega_P^2}{4\pi}\mathrm{Re}\frac{1}{\sigma(\omega)} \tag{2.47}$$

where ω_P is the plasma frequency; the pseudogap is rather harder to pick out from the in-plane conductivity σ_{ab} itself. At large ω_P, one generally sees $\frac{1}{\tau(\omega)} \approx A\omega$, where $A \geq$ 1 in underdoped materials and $\approx$ 1 in optimally doped ones. And it then drops to much smaller values, $\frac{1}{\tau} \ll \omega$, below a characteristic pseudogap frequency. While in optimally doped materials, this manifestation of a pseudogap is only observed at temperatures less than T_{c} , in underdoped materials persist well above T_{c} , and indeed to be not strongly temperature dependent.

2.7.3 Theories of the pseudogap

The experimental evidence of the pseudogap does not yet provide a single view, neither do the available theoretical models. A few selected models are described below. Several of the models described below involve preformed pairs at T^* without phase coherence

[21–29]. The theoretical models seem to explain the pseudogap are summarized in the following:

- ***Spin–charge separation:*** One scenario which has received considerable attention involves spin–charge separation. This idea was first proposed by Anderson in his as the resonating valence bond (RVB) theory [30]. Nagaosa and Lee [31,32] produced a Ginzburg–Landau theory of the spin–charge separated system calculating various transport properties in the pseudogap state. Spin–charge separation creates *holons* with zero spin and *spinons* which are zero charge, spin–1/2 fermions. The spinons pair to form a gap in the spin excitations, identified as the pseudogap. The holons Bose–condense at T_c to form the superconducting state. At present it is believed that even though it is the holons which Bose–condense, gauge field fluctuations lead to a strong coupling between the spinons and holons. A gauge theory of the normal state, including the pseudogap, has been developed by Lee and Nagaosa [31, 32]. Experimental results suggest that T^* is related to the occurrence of a spin–gap in the high-T_c materials [33–35].

- ***Phase–fluctuations:*** It is proposed that superconductors with a low carrier density are characterized by a relatively small phase stiffness and thus, the poor screening implies a significant role of phase–fluctuations [36–45]. Emery and Kivelson [36] have developed a preformed pair model of the pseudogap based on microstripes. Phase separation takes place on a microscopic scale generating dynamical charged stripes separated by insulating antiferromagnetic (AFM) stripes. These microstripes form at the upper crossover temperature T $\gg T^*$. Above this temperature the charge is uniformly distributed. Below T^* charge is confined to the metallic stripes forming a 1D electron gas (1DEG). Spin and charge are separated as spin resides in the AFM stripes. As the temperature is lowered, AFM correlations build up. At the lower crossover temperature T^* pairing behavior emerges. Pairing is a result of a spin gap in the AFM stripes. This is manifested in the 1DEG via pair hopping between the 1DEG and AFM stripes. Emery and Kivelson [36, 37] describe this as a magnetic proximity effect. At this point there are only 1D superconducting correlations. The pseudogap is associated with this spin gap. At T_c Josephson coupling between the metallic stripes becomes large enough to yield global phase coherence. Note that the pairing correlations below T^* are not giving rise to real space pairing; the pairing correlations are dynamical. The phase–fluctuation scenario explains quite natural the strongly enhanced Nernst signal [21] above the critical transition temperature T_c in the underdoped HTSC materials.

- ***Interlayer exchange coupling:*** Millis and Monien [46] proposed that the pseudogap in bilayer compounds was due to interlayer exchange coupling. Further work [47] have produced a model with interlayer pairing of holons producing a

> spin pseudogap. The authors claim that the pseudogap crossover temperature T^* for single layer materials, namely $\mathrm{La}_{1.85}\mathrm{Sr}_{0.15}\mathrm{CuO}_4$, is just slightly above T_c . Interlayer coupling enhances T^* to temperatures well above T_c . Recent data on other single layer compounds throws this scenario into to be uncertain. The single layer mercury compound shows a crossover temperature well above T_c [48].

Spin-polarized quasiparticle injection (SPQI) is a sensitive tool for detecting the opening of a spin-gap, as proposed by Si [49]. A major point of this thesis is the influence of SPQI on the normal state resistivity of YBCO around the pseudogap temperature T^*. It is proposed that the experimental data allow to distinguish between the suggested models of spin-charge separation and phase fluctuations.

Chapter 3

Colossal magnetoresistance

Shortly after the discovery of a colossal magnetoresistance in doped rare-earth manganites the physics involved in magnetic oxides gained an increasing interest.

In section 3.1, only an introduction and an overview of the theory of magnetism is presented in addition to the phenomenological concepts in ferromagnetism.

Section 3.2 focuses on the colossal magnetoresistance (CMR) effect. In a general part the state of the art of the theoretical description will be briefly presented, the subsequent part considers $La_{2/3}Ca_{1/3}MnO_3$ (LCMO) as the member of this class of material that is important of this work.

3.1 Ferromagnetism

In this section, the fundamentals of magnetism are briefly shown. An introduction to the major classes of magnetic behavior is presented via the concept of long-range magnetic order, with a special focus upon the phenomenology of ferromagnetic materials.

3.1.1 Magnetic Order

In a solid the band electrons and sometimes also the ions in the crystalline lattice, carry a microscopic magnetic moment. In case of electrons, this is due to the spin angular momentum; atomic moments result from the orbital motion of the shell electrons, or incompletely filled inner shells. There is a significant difference in character between these moment-carriers. The atoms, and therefore also their moments, are localized at the crystal lattice points. The band electrons, however, propagate through the crystal as Bloch waves, and are regarded as delocalized. Consequently, it is necessary to consider a density of their spins, which is a continuously varying function of position.

In a non-magnetic material there is no long-range ordering of the microscopic magnetic moments over sufficiently large distances, the orientation of the localized moments on the atoms varies randomly, and the departures from the band-electron's average spin density of zero are uncorrelated. Thus, in both cases, the magnetization M (the average moment per unit volume) is zero.

The application of an external magnetic field H has two effects: (a) to align the microscopic magnetic moments in direction of the field, and (b) to induce anti-aligned moments due to the orbital response of the electrons. When the former process is dominant, the material is *paramagnetic*; dominance by the latter leads to *diamagnetism*. In both cases, the external field induces a magnetization, $M = \chi H$; where χ is the magnetic susceptibility of the material and is positive for paramagnets, negative for diamagnets. For both materials, the magnetization vanishes when the external field is removed, the system returning to its original disordered state.

In a magnetic material there exists a spontaneous long-range ordering of the microscopic moments. This is due to so-called *exchange interactions* between the moment-carriers. There are two major classes of magnetic materials exhibiting spontaneous order ferromagnets and antiferromagnets.

In ferromagnetic materials, the exchange interactions tend to align the moments in one direction, giving the material a non-zero magnetization. The preferred direction of alignment (the so-called easy axis) is determined by secondary coupling to the crystal field (e.g. spin-orbit effects) [50]. In contrast to ferromagnets, the exchange interactions in antiferromagnetic materials tend to periodically order the moments in such a way that there is no overall magnetization of the system. In both ferromagnets and antiferromagnets the tendency of the exchange interactions to order the moments is counteracted by thermal fluctuations; in the limit of zero temperature, the thermal agitations which destroy the ordering vanish, and the degree of order is limited only by quantum effects.

3.1.2 Ferromagnetism

The characteristic property of a ferromagnet is the spontaneous magnetization produced by the exchange interactions. This magnetization is not necessarily uniform across the specimen. A ferromagnet may be divided into macroscopic volumes called domains, each possessing one oriented magnetic moment.

The application of an external magnetic field results in an *expansion* of the domains with moments aligned with the field at the expense of those with anti-aligned moments. This process is irreversible and leads to a permanent increase in the magnetization of the sample (*hysteresis effect*). The magnitude of the spontaneous magnetization of a domain obtains a maximum in the limit of zero temperature. This maximum magnetization is referred to as the saturation magnetization (M_s) of the material. Due to the dominance of thermal fluctuations, the spontaneous magnetization of a ferromagnet disappears above a certain critical temperature, the Curie temperature (T_Curie). Generally, a ferromagnetic material becomes paramagnetic above T_Curie, but certain rare-earth elements exhibit antiferromagnetic ordering at temperatures higher than T_{Curie} [50].

The phase transition from the ferromagnetic to the paramagnetic phase (the *normal* phase) is the classic example of a second order phase transition [51].

Theoretical attempts of a microscopic theory of ferromagnetism generally regard either the magnetic ordering of the lattice atoms or the band electrons as of primary importance. Such models are classified as "*localized*" and "*itinerant*", respectively. Although in any real system, both localized and itinerant effects are likely to be present to differing degrees, it is usually possible to expect one to dominate the other. For example, the rare-earth ferromagnets and their ionic compounds (such as EuO and GdC_{12}) are regarded as good examples of localized systems, whereas the ferromagnetism of the $3d$ transition metals (iron, nickel, and cobalt) and a number of alloys of non-magnetic elements (e.g. $ZrZn_2$ and Sc_3In) are best explained by the itinerant scheme [50, 52].

Theoretical studies of itinerant electron models began in 1929 with the pioneering efforts of Bloch. His work indicated that ferromagnetism was only likely to appear in the homogeneous electron gas at very low densities, r_{s}; more detailed studies have proved that the homogeneous electron gas is not ferromagnetic at typical metallic densities [52]. This has been confirmed by computational studies which predict the onset of ferromagnetic ordering only at extremely low densities r_{s}. There is, however, much disagreement about the precise density range, and the physics of these low density regimes should be regarded with caution [53]. More detailed models of itinerant electron systems have met with considerably better success than the homogeneous electron gas approximation. These models have demonstrated the main important role played by the band structure in determining whether or not itinerant electron ferromagnetism will appear in a material. Of particular note is the so-called Slater and Stoner models [54, 55], which gives a criterion for the appearance of ferromagnetism in terms of the DOS at the Fermi energy. The Stoner model gives a very basic phenomenological description of an itinerant system, and considerable improvement has been made upon it [51, 56]. Nevertheless, it has provided a useful starting point for the study of itinerant electron ferromagnetism.

3.2 Colossal magnetoresistance

In this section a brief introduction about the history of origin of the colossal magnetoresistive (CMR) materials will be given. In the following subsections the early theoretical models to explain the CMR effect will briefly be presented. More recent theoretical models will be mentioned afterwards.

3.2.1 The early days of manganites

It is widely recognized that the first paper reporting results for manganites was presented in 1950 by Jonker and Van Santen [57]. In that first publication, La was replaced either by Ca, Sr, or Ba, and results for polycrystalline samples of (La,Ca)MnO_3, (La,Sr)MnO_3, and (La,Ba)MnO_3 were reported. The main result was the appearance of ferromagnetism in these compounds, as described below. Jonker and Van Santen clarified in their first publication that the term "manganites" is not rigorous, and only compounds containing tetravalent Mn should actually be called manganites. However, they write *"For the sake of simplicity the compounds containing trivalent, as well as those containing tetravalent, manganese will be designated as manganites"*, a convention that it is still followed today. Jonker and Van Santen found that the manganites they studied crystallize in a ABO_3 perovskite structure, is shown in Fig. 3.1.

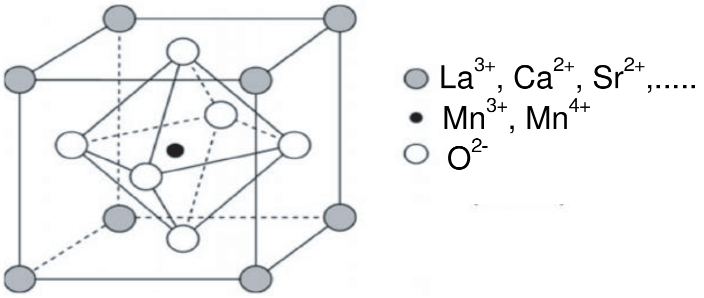

Figure 3.1: Schematic view of the cubic perovskite structure.

The A-site of the perovskite contains a large ion, such as Ca^{2+}, Sr^{2+}, La^{3+}, etc., while the B-sites have a small ion, such as Mn^{3+}, Mn^{4+}, or others. The oxygens surround the B-sites forming an octahedral cage. Typical ionic sizes, directly quoted from [57], are: Ca^{2+} = 0.106 nm, Sr^{2+} = 0.127 nm, Ba^{2+} = 0.143 nm, La^{3+} = 0.122 nm for the A-site ion; Mn^{3+} = 0.07 nm and Mn^{4+} = 0.052 nm for the B-site ion; and O^{2-} = 0.132 nm for oxygen. Manganese is the smallest of the ions involved in the manganites. The Curie temperature was obtained by Jonker and Van Santen [57] using magnetization measurements, and the early samples of manganites contained an excess of oxygen, and the results they obtained are not accurate compared with the modern versions of the (La,Ca)MnO_3 phase diagram, as will be shown later.

In those early studies, the ferromagnetic phase was attributed to a positive *indirect–exchange* interaction. This view was soon replaced by the currently more widely accepted *double–exchange* (DE) picture, discussed later.

In the early studies of manganese oxides, it was also noticed that (La,Sr)MnO_3 can only admit up to 70% Sr. Otherwise, a two-phase compound is obtained for geometrical reasons related to the so-called tolerance factor Γ. This factor plays an important role in Mn oxides, where $\Gamma = (r_{\mathrm{A}} + r_{\mathrm{O}})/\sqrt{2}(r_{\mathrm{B}} + r_{\mathrm{O}})$. The perovskite structure is stable for

$0.89 < \Gamma < 1.02$, $\Gamma = 1$ corresponding to the perfect cubic closely packed structure. Generally, Γ differs appreciably from 1 and the manganites have, at least at low temperature, a lower rhombohedral symmetry or orthorhombic structure.

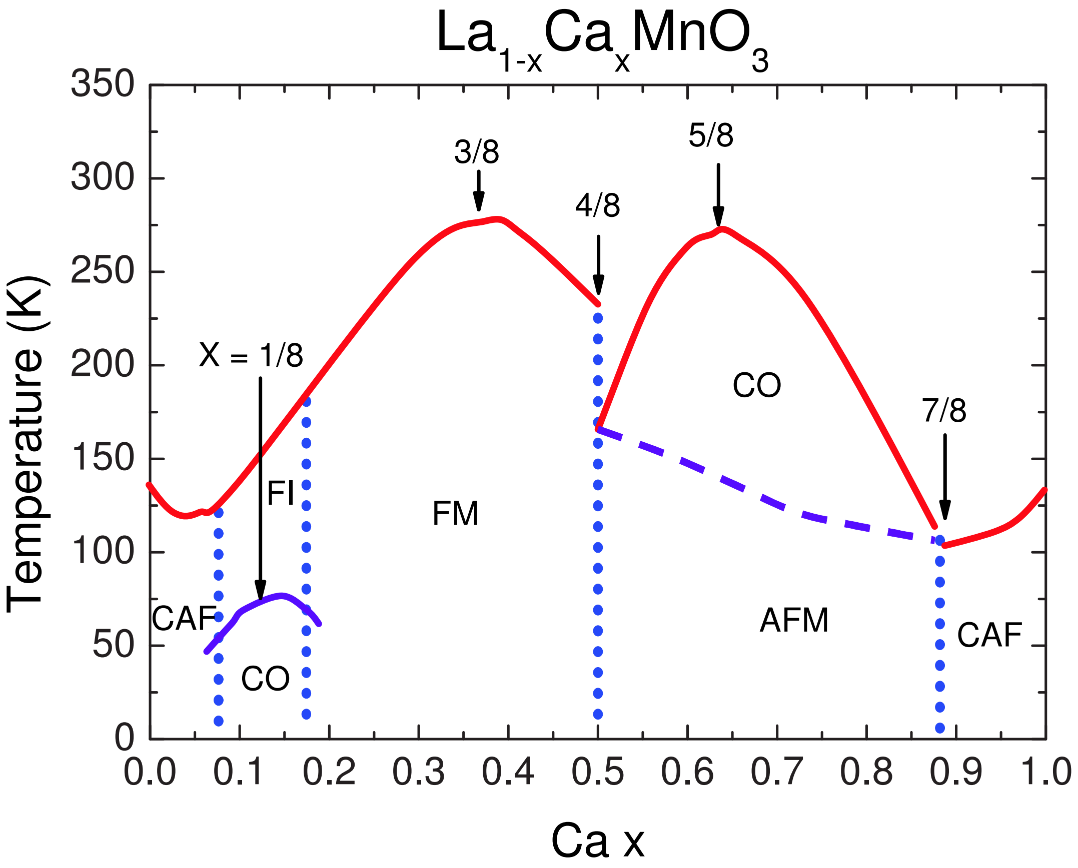

Figure 3.2: The phase diagram of $La_{1-x}Ca_xMnO_3$, after Cheong and Hwang [61]. There exist well-defind anomalies at x = $\frac{n}{8}$ (n = 1, 3, 5, and 7). FM : Ferromagnetic Metal, FI: Ferromagnetic Insulator, AF: Antiferromagnetism, CAF: Canted Ferromagnetism, and CO: Charge/orbital Ordering.

In a subsequent paper by Van Santen and Jonker [58] a few months after the original publication, the conductivity of manganites was reported. Anomalies in the conductivity were found at the Curie temperatures. The study of the lattice parameters as a function of hole doping was reported in those early days by Jonker [59], observing that near the composition of 100% La the crystal is distorted, while at higher Sr or Ca densities, it is not. These distortions are associated with the Jahn–Teller effect, which is very important in manganites, as will be shown later. A few years after the original work of Jonker and Van Santen [59], the magnetoresistance data on manganites was reported by Volger [60]. The author wrote *“Manganites, when in the ferromagnetic state, show a notable decrease of resistivity in magnetic fields”*.

It was already noticed in those early studies that standard explanations for the effect did not work, and that the effect was likely related to the favoring of the ferromagnetic state by a magnetic field. However, one should note that the truly enormous magnetoresistance, the now famous *"colossal"* effect, was discovered much later, in the 1990s.

Among the key efforts widely cited from the early investigations of manganites is the paper by Wollan and Koehler [62] using neutron diffraction techniques to characterize the magnetic structures of $\mathrm{La_{1-x}Ca_xMnO_3}$ in the entire range of compositions. Wollan and Koehler were among the first to use the technique of neutron scattering to study magnetism in materials. Those authors found that, in addition to the ferromagnetic phase reported by Jonker and van Santen, many other interesting antiferromagnetic phases were present in manganites. In some cases, they also reported evidence of charge ordering (CO) coexisting with the antiferromagnetic (AFM) phases.

3.2.2 Doped lanthanum manganite:$\mathrm{La_{2/3}Ca_{1/3}MnO_3}$

The phase diagram of $\mathrm{La_{2/3}Ca_{1/3}MnO_3}$ was measured by Cheong and Hwang [61], and is given in Fig. 3.2. The undoped parent compound $\mathrm{LaMnO_3}$ has an antiferromagnetic insulating ground state. $\mathrm{LaMnO_3}$ and $\mathrm{CaMnO_3}$ are both antiferromagnetic insulators. At first sight a mixture of $\mathrm{LaMnO_3}$ and $\mathrm{CaMnO_3}$ is expected to show no spectacular effect. But, in their phase diagram a ferromagnetism is found, metallicity and several regions with spin and charge orderings. An important aspect in the unexpected rich phase diagram is the small but relevant distinction in crystal structure, although both compounds are perovskites. $\mathrm{LaMnO_3}$ consists of deformed $\mathrm{MnO_6}$ octahedra, whereas the octahedra are perfect in $\mathrm{CaMnO_3}$. The origin of the deformation is the crystal field splitting of the $3d$ orbitals.

Above 10% Ca doping the ferromagnetic interactions suppress the antiferromagnetic coupling and a ferromagnetic ground state is obtained. In the region of 20% to 50% Ca substitution the ground state is a ferromagnetic metal, dominated by double exchange that will be introduced in next section. According to Cheong's phase diagram, Fig. 3.2, the ferromagnetic metallic phase emerges instantly above a critical concentration, at all temperatures below T_{Curie}.

3.2.3 The early theoretical models

The theoretical studies of manganites in the 1950s focused on the origin of the ferromagnetic phase. It was decades after that initial work, when the *colossal* magnetoresistance effects were found, and the excitement around Mn–oxides mainly shifted toward understanding the origin of such huge magnetotransport properties, with potential technological applications. In the following the basic theoretical description for the manganites namely double–exchange and Jahn–Teller effect will be presented.

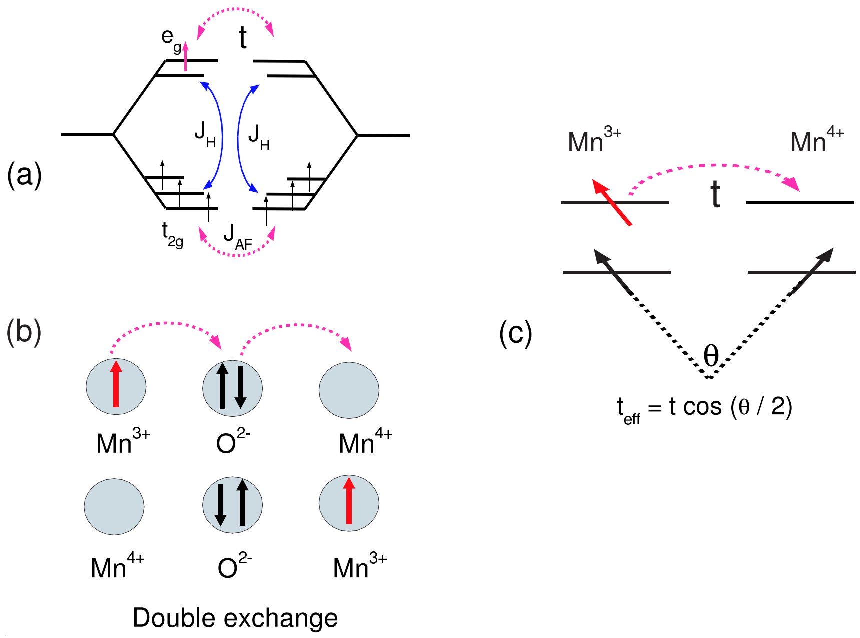

Figure 3.3: (a) Schematic representation of the ideas of Zener to explain ferromagnetism. Zener envisioned a system with both localized and mobile electrons, which in the manganite language are the t_{2g} and e_g electrons, as indicated. (b) Schematic view of the DE mechanism. (c) The effective hopping $t_{\rm eff}$ mechanism is drown schematically.

3.2.3.1 Double–exchange (DE)

The basis for understanding origin of the ferromagnetic phase in CMR type materials or *spin polarization* was presented by Zener in 1951, in a couple of papers [63–65], where mainly qualitative statements and analyses of experiments were presented. Zener's work is widely regarded as providing a proper explanation of manganite ferromagnetism.

Zener interpreted ferromagnetism as arising from an indirect coupling between incomplete d-shells, via conducting electrons. In the first paper of Zener [63], the manganites were not addressed explicitly, but in Mn-oxide language one should think of the incomplete d-shells as the so-called t_{2g} localized spins of manganites, and the conduction electrons are the e_g electrons. It is sufficient to consider a qualitative description of the splitting of the five d-levels in the presence of a crystal environment, as shown in Fig. 3.3(a).

The Hund's rule in each individual ion or atom is enforced by a ferromagnetic Hund coupling $J_{\rm H}$, as in Fig. 3.3(a). This effect was argued by Zener to play a key role in his mechanism, enforcing the configuration where the unpaired spins are aligned to lower the energy. Since the conduction electrons do not change their spin as they move from ion to ion, the electron hopping maintains the z-projection of the spin, Zener reasoned that those electrons are able to move in the crystal in the optimal manner when the net spin of the incomplete d-shells are all parallel. Otherwise, an up electron can land on a down spin ion, and pay an energy proportional to the Hund coupling. In other words, the conduction electrons lower their kinetic energy if the background of d-shell spins, or the t_{2g} spins of manganites, is fully polarized, details will be shown in the next subsection.

The kinetic energy is regulated by a hopping amplitude denoted by t. The d-shell spins are then indirectly coupled via an interaction mediated by the conduction electrons. Zener remarked clearly in his papers that a direct coupling between d-shells (not mediated by conduction electrons, but by the direct virtual hopping of d-electrons) is of opposite sign leading to antiferromagnetism, rather than to ferromagnetism. The coupling involved in this direct exchange process is called J_{AF}, and it will be shown to be important in the physics of manganites. The ideas of Zener are known today as *“double exchange”*.

This mechanism is sketched in Fig. 3.3(b). It can be explained to a *simultaneous* transfer of an electron from the oxygen to the right Mn, and from the left Mn to the oxygen, such that the net transfer is of an electron from left Mn to right Mn. This mechanism leading to ferromagnetism that Zener found should not be confused with the *superexchange* ideas, which also use an oxygen as a bridge between ions. Zener remarked that the superexchange interaction leads to an antiferromagnetic alignment of spins. The original double-exchange idea in [64] was discussed not as a procedure to explain ferromagnetism but as a mechanism for electron transfer, that was built in the context of the original idea of ferromagnetism mediated by conduction electrons.

Zener’s work was continued by ANDERSON[1] and Hasegawa [66] and De GENNES[2] [67], who studied the proposed mechanism in detail. They explained that a better way to describe the motion of electrons from Mn-to-Mn is to transfer electrons *one-by-one*, still using the oxygen as a bridge between ions, rather than simultaneously as believed by Zener. Any perturbation approach in the hopping amplitude t will naturally lead to a one-by-one transfer of electrons. Perhaps the most often-quoted portion of the work of Anderson and Hasegawa [66] is the effective hopping t_{eff} of an electron jumping between two nearest-neighbor Mn ions. In fact, the calculation shows that $t_{\text{eff}} = t\cos\frac{\theta}{2}$, where θ is the angle between t_{2g} spins located at the two sites involved in the electron transfer, as shown in Fig. 3.3(c).

3.2.3.2 Jahn–Teller effect

For an isolated $3d$ ion, five degenerated orbital states are available to the $3d$ electrons with $\ell = 2$. In a crystal, the degeneracy is partly lifted by the crystal field splitting. The five d-orbitals are split by a cubic crystal field into three t_{2g} orbitals and two e_g orbitals. For the MnO_6 octahedron, the splitting between the lowest t_{2g} level and the highest e_g level is Δ= 1.5 eV (Fig. 3.4). For the Mn^{3+} and Mn^{4+} ions, the interatomic correlations ensure paral-

---

[1] Nobel prize 1977

[2] Nobel prize 1991

lel alignment of the electron spins (first Hund's rule); the corresponding exchange energy[3] of about 3 eV [114]. In a crystal field of symmetry lower than cubic, the degeneracy of the e_g and levels is lifted, as shown in the Fig. 3.4(b) for an axial elongation of the oxygen octahedron. Although the energy of Mn^{4+} remains unchanged by such a distortion, the energy of Mn^{3+} is lowered. Thus, Mn^{3+} has a marked tendency to distort its octahedral environment in contrast to Mn^{4+}. This effect is known as *Jahn-Teller* distortion and it is rather effective in the lightly doped manganites, i.e. with a large concentration, (1 - x), of Mn^{3+} ions. The Jahn-Teller distortions are not independent from one Mn^{3+} site to another (cooperative Jahn-Teller effect). This is illustrated by the structure of $LaMnO_3$ (Fig.3.1) in which the MnO_6 octahedra are strongly elongated within the ab-plane in a regular way leading to a doubling of the unit cell. On increasing the Mn^{3+} content, the Jahn-Teller distortions are reduced and the stabilization of the ($3z^2$ - r^2) e_g–orbital becomes less effective. Nevertheless, in a large number of manganites, the e_g–orbitals of two types, ($3z^2$ - r^2) and (x^2 - y^2) are not occupied by the e_g electrons of Mn^{3+} at random and an orbital order is achieved.

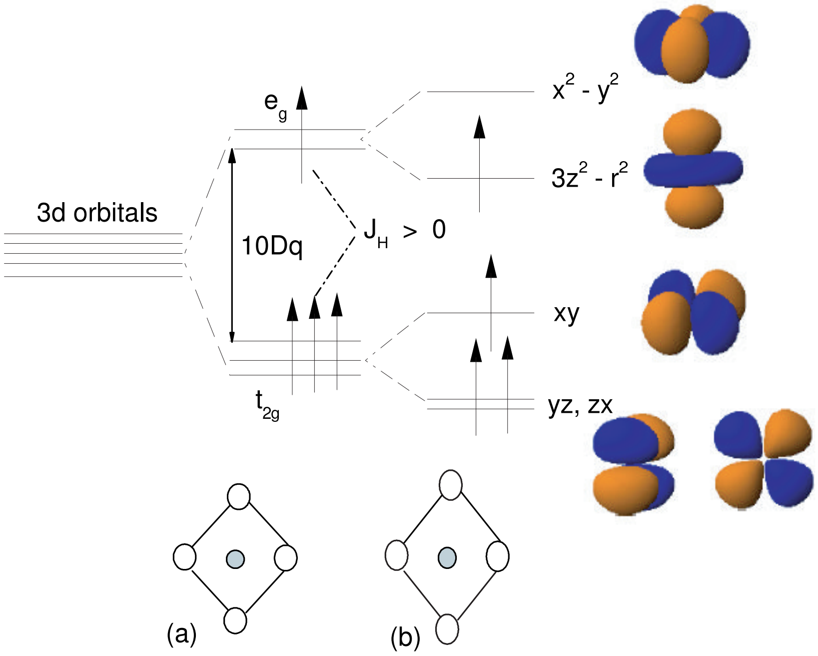

Figure 3.4: Energy level diagram and orbital eigenstates of Mn^{3+} in a crystal field of cubic and tetragonal symmetry.

3.2.4 Transport and CMR effect

Figure 3.5 shows the typical behavior of Ca-doped CMR materials. The temperature dependence of the resistance for a thin film of 1/3-Ca doped $La_{1-x}Ca_xMnO_3$ with thickness

---

[3] This energy what will be called later as J_{spin}.

of t = 200 nm under several magnetic fields applied || to the electric current is shown. One of the most remarkable properties of the manganites is the influence of a magnetic transition on the electronic conduction. The resistance below the magnetic ordering, the Curie temperature T_{Curie}, exhibits a positive thermal coefficient, indicating metallic-like behavior. Above T_{Curie} a negative thermal coefficient is found. This brings about a maximum in the resistivity curve near T_{Curie}. The implications of this behavior were first explored in 1993, when a reduction of the resistance was observed in thin films under application of an external magnetic field by Von Helmolt *et al.* [68] and Chahara *et al.* [69]. This reduction was only 50% of the zero field resistance. One year later it proved to be possible to reduce the resistivity by several orders of magnitude [70].

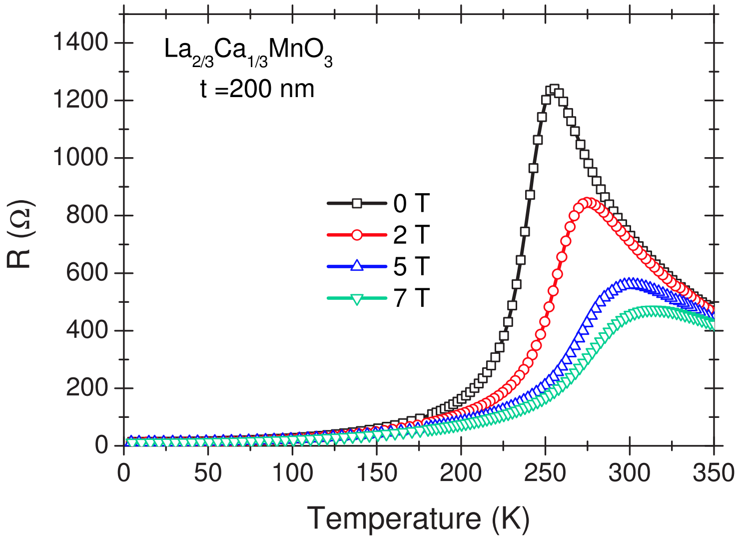

Figure 3.5: Resistance versus temperature for a thin film of 1/3-Ca doped $La_{1-x}Ca_xMnO_3$ with thickness of t = 200 nm under several magnetic fields applied || to the electric current.

A defining moment for the field of manganites was the publication by Jin *et al.* [70] of results with truly colossal MR ratios. Those authors studied films of $La_{2/3}Ca_{1/3}MnO_3$ and defining the magnetoresistance (MR) ratio as $\Delta R/R = (R_{\mathrm{H}} - R_0)/R_{\mathrm{H}}$, where R_0 is the resistance without a magnetic field, and R_{H} is the resistance in a magnetic field of 6 T, Jin *et al.* reported MR ratio values much higher than previously observed by other authors [68, 69].

The term Colossal Magnetoresistance (CMR) was born. The new term is a superlative of Giant Magnetoresistance, which is observed in the resistance of ferromagnetic/nonmagnetic superlatices by switching an external field. Giant magnetoresistance is caused by introducing interfaces in spin polarized conductors and is restricted below T_{Curie}, whereas CMR is a bulk property which originates from magnetic ordering and is usually confined to the vicinity of T_{Curie}. The electronic transport properties of the transition metal oxides strongly interact with the magnetic properties and with the crystal lattice. A similar change can occur due to external effects, such as a magnetic field or a hydrostatic pressure. The behavior of the manganites is a beautiful example to show the interaction between chemical composition, experimental conditions and physical properties.

3.2.5 More recent CMR models

After the early studies of manganites described above, Tokura [71] proposed that the charge-ordering (CO) states observed by Wollan and Koehler [62], and Jirák *et al.* [73] are very important for the explanation of the CMR effect, see the phase diagram in Fig.3.2. They presented results indicating an abrupt collapse of the charge-ordered state into a ferromagnetic state (FM) under the influence of a magnetic field. The competition between CO and FM is indeed a key component of the current theories of manganites aiming to explain the CMR phenomenon. It is clear from the experiments and the theory that the CO/FM transition should be first-order unless disordering effects smear it into a rapid but continuous transition. The huge CMR effect in some compounds at very low temperatures, such as shown in Fig.3.5, appears to be caused by the CO/FM first-order transition induced by magnetic fields. This physics is not contained at all in the early theoretical studies of manganites in the 1950s and 1960s, which were based on the so-called double-exchange effects and one-orbital models. Only in the late 1990s and early 2000s Tokura [71] suggested the CO/FM competition model and the phase separation model proposed by Dagotto [72] has been identified as the key of the CMR phenomenon.

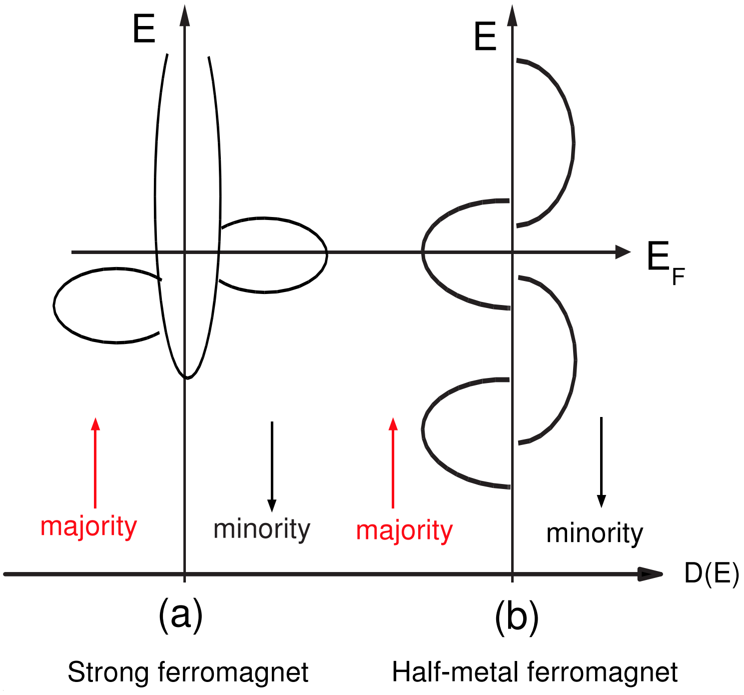

Figure 3.6: (a) Schematic density of states of a strong ferromagnet and (b) half-metallic ferromagnet.

3.2.6 Spin-polarization and CMR

A fundamental interest for both basic physics and device applications is the degree of spin-polarization P at the Fermi level. The band-structure of ferromagnets is spin dependent and two subbands are found for majority (carrier spin directed parallel to the magnetization) and minority (spin antiparallel to the magnetization) carriers, respectively [74]. The schematic density of states of a strong and a half-metallic ferromagnet (e.g. CMR) is shown in Fig. 3.6(a) and (b); respectively. The majority d bands are completely filled in case of the strong ferromagnet. In the case of an itinerant ferromagnet ($\mathrm{La}_{2/3}\mathrm{Sr}_{1/3}\mathrm{MnO}_3$ or $\mathrm{La}_{2/3}\mathrm{Ca}_{1/3}\mathrm{MnO}_3$ as an example), the spin-polarization is often defined as the normalized difference of the majority ($n\uparrow$) and minority ($n\downarrow$) density of states at the Fermi level, thus

$$P_n = \frac{n\uparrow - n\downarrow}{n\uparrow + n\downarrow} \tag{3.1}$$

This definition is related to the definition of the magnetization as the difference between the integrated majority and minority carrier density, $M = \mu_B \int (n\uparrow - n\downarrow) dE$, and often a scaling P(T)$\propto$ M(T) is expected. The spin-polarization defined in this way might be probed by spin-polarized photoemission. However, as pointed out by Mazin [75], the definition of spin-polarization is by no means unique. Often transport properties are of interest, especially for applications. In a ferromagnet the majority and minority carriers can be regarded as two parallel transport channels as proposed theoretically by MOTT[4] [76], Campbell and Fert [78], and experimentally by Meservey and Tedrow [77]. The definition of the spin-polarization in terms of the majority ($J\uparrow$) and minority ($J\downarrow$) current densities seems more appropriate. Within classical Boltzmann transport theory, $J_{\uparrow\downarrow} \propto \langle nv\rangle_{\uparrow(\downarrow)}\tau_{\uparrow(\downarrow)}$, where $\langle....\rangle$ denotes a Fermi surface average and $\tau_{\uparrow(\downarrow)}$ the relaxation times for majority and minority carriers, respectively. Assuming a spin-independent relaxation time, one finds

$$P_J = \frac{J\uparrow - J\downarrow}{J\uparrow + J\downarrow} = \frac{\langle nv^2\rangle_\uparrow - \langle nv^2\rangle_\downarrow}{\langle nv^2\rangle_\uparrow + \langle nv^2\rangle_\downarrow} \tag{3.2}$$

Within the two-current model, the spin-polarization defined by the majority and minority currents can be simply related to the majority ($\rho\uparrow$) and minority ($\rho\downarrow$) resistivities:

$$P_\rho = \frac{\rho\uparrow - \rho\downarrow}{\rho\uparrow + \rho\downarrow} \tag{3.3}$$

The channel resistivities can be determined at low temperature from deviations of Matthiessen's rule. These depend on the impurities present in the metal and consequently the spin-polarization can be tuned by alloying.

---

[4] Nobel prize 1977

The experiments capable of determining the transport spin-polarization are spin-polarized tunnelling between ferromagnetic contacts and the dynamic conductance of superconductor/ferromagnet (SC/FM) contacts. Mazin [75] analyzed the transport through a SC/FM contact. In the case of ballistic transport without a barrier, the current through the contact is proportional to $\langle nv \rangle$; thus, the ballistic spin-polarization is defined by

$$P_v = \frac{\langle nv \rangle_\uparrow - \langle nv \rangle_\downarrow}{\langle nv \rangle_\uparrow + \langle nv \rangle_\downarrow} \tag{3.4}$$

and does not agree with the spin-polarization equation (3.2) defined via currents. If a specular barrier is present, the tunnelling current depends in a more complex way on both the Fermi velocity and the barrier transparency, and the measured spin-polarization does not agree with any of the definitions introduced so far. This analysis shows that experimental values obtained with different techniques relate to different definitions of the spin-polarization that need not necessarily agree.

Some data on the spin-polarization of elemental as well as oxide magnets are summarized in Table (3.1). The spin-polarization was determined by ferromagnet/insulator/ferromagnet (FIF) tunnelling, ferromagnet/insulator/superconductor (FIS) tunnelling, Andreev reflection (AR) [79] at superconductor/ferromagnet interfaces spin-polarized photoemission spectroscopy (SPES) and 2D angular correlation of electron–positron radiation (2D-ACAR). Here, only spin-polarization measurements using AR will be discussed in detail.

Electron transport through a normal-metal/superconductor interface for energies below the superconducting gap Δ is possible through AR. An electron incident from the normal metal forms a pair with another electron of opposite momentum and spin and enters the superconductor as a Cooper pair, while a hole is reflected. This leads to a conductivity enhancement by a factor of two at small voltages. At large bias voltages, transport is dominated by quasiparticle injection and the conductance approaches the normal state conductance G_n. In case of a FM/SC interface, AR is suppressed, since not every majority electron finds a minority electron with appropriate momentum to form a Cooper pair. It is evident that the zero-bias conductance should vanish in the case of a half-metallic ferromagnet. It was shown [80] that the conductance of a FM/SC interface at zero temperature is given by

$$\frac{1}{G_n}\frac{dI}{dV} = 2(1- \mid P_v \mid) \qquad eV \ll \Delta \tag{3.5}$$

with the spin-polarization P_v as defined above. Thus, from the suppression of the conductance at zero bias the spin-polarization P_v can be determined. This method is not sensitive to the sign of the spin-polarization.

Table 3.1: Spin-polarization as determined from FIF, FIS tunnelling, AR and SPES for elemental ferromagnets and oxide magnets. The AR technique is not sensitive to the sign of the spin-polarization. All values were measured at temperatures of T = 4.2 K or below, except for the SPES value of Ni, that was measured at T = 300 K.

Compound	FIS	FIF	AR	SPES
Fe	+0.45[1]	+0.35[2]	–	+0.40[3]
Co	+0.42[1]	+0.34[4]	0.37[5]	-0.40[6]
Ni	+0.31[1]	–	0.32[5]	-0.30[7]
Gd	+0.13[8]	–	–	+0.05[9]
CrO_2	–	–	**+0.90**[10]	**+1.0**[11]
Fe_3O_4	–	-0.50[12]	–	-0.40[13]
$SrRuO_3$	**-0.095**[14]	–	–	–
$La_{2/3}Sr_{1/3}MnO_3$	**+0.70**[15]	**+0.83**[16]	**+.80**[10]	**+0.90**[11]

[1] Ref. [81], [2] Ref. [82], [3] Ref. [83], [4] Ref. [84], [5] Ref. [85], [6] Ref. [86], [7] Ref. [87], [8] Ref. [88], [9] Ref. [89], [10] Ref. [80], [11] Ref. [90], [12] Ref. [91], [13] Ref. [92], [14] Ref. [93], [15] Ref. [94], [16] Ref. [95].

Results of spin-polarization measurements from FIF and FIS measurements, AR and spin polarized photoemission are summarized in Table (3.1) for the elemental magnets Fe, Co, Ni, and Gd, as well as for the oxide magnets, CrO_2, Fe_3O_4,$SrRuO_3$, and $La_{2/3}Sr_{1/3}MnO_3$. Although the data show some scatter, it is clear that CrO_2 and $La_{2/3}Sr_{1/3}MnO_3$ have a spin-polarization much larger than that of elemental ferromagnets.

Chapter 4

Ferromagnetism and Superconductivity

In the previous two Chapters 2 and 3 the basic theory of both superconductors and colossal magnetoresistance materials was presented. In this Chapter some peculiarities are described when superconductors and ferromagnets are brought to an intimate contact, e.g. bilayers.

The first section describes the proximity effect of normal metals and superconductors (NM/SC) electronically in contact. This will be followed by a section where the normal metal is replaced by a (weak or stronger) ferromagnetic. Here the model of spin-polarized quasiparticle ***self*** diffusion will be addressed to explain the breaking the Cooper-pairs in the superconductor .

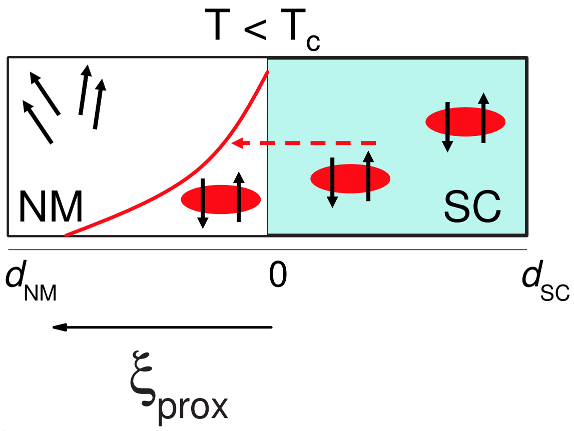

Figure 4.1: Schematic diagram of the order parameter at the interface between a normal metal and superconductor at $T \ll T_{\mathrm{c}}$.

4.1 Normal metal/superconductor bilayer

In ideal normal metal/superconductor structure is of a high interface transparency there is a distance dependent probability (*proximity effect*) for the existence of Cooper-pairs in the normal metal (see Fig. 4.1). In the Ginzburg-Landau approach, this effect is described by a boundary condition; the appropriate boundary condition is a direct generalization of

$$\frac{\partial\psi}{\partial n} - \frac{2ie}{\hbar}A\psi = \frac{1}{\xi_{\text{prox}}}\psi \tag{4.1}$$

ξ_{prox} is the proximity length that describes the decay of Cooper-pairs density inside the normal metal.

There are several physical effects related to the existence of ξ_{prox}, like, for example, the decrease of the critical temperature of thin superconducting films deposited on the normal metal.

The microscopic theory gives for a superconductor/insulator interface:

$$\xi_{\text{prox}} = \frac{\xi_\circ^2}{a_\circ} \tag{4.2}$$

where $\xi_\circ$ is the coherence length of the superconductor and $a_\circ$ is the interatomic distance. At a NM/SC interface in the clean limit $\xi_\circ \ll \ell_e$; where ℓ_e is the mean free path we have:

$$\xi_{\text{prox}} = \frac{\hbar v_F}{k_B T} \tag{4.3}$$

while for the dirty limit $\xi_\circ \gg \ell_e$ we get:

$$\xi_{\text{prox}} = \sqrt{\frac{\hbar v_F \ell_e}{6\pi k_B T}} \tag{4.4}$$

Equation (4.4) shows that $\xi_{\text{prox}} \propto \frac{1}{T^{1/2}}$. This relationship will be later important for the comparison between NM/SC and FM/SC proximity effect.

In conventional superconductors the coherence length is much larger than the atomic distance ($\xi_\circ \gg a_\circ$). For superconductors in contact to an insulator, ξ_{prox} is very small so superconductivity is not affected. When the coherence length is short,($\xi_\circ \approx a_\circ$), one can expect some important effects. A typical example are the high-T_c superconductors. In case of a NM/SC interface, superconductivity is induced in the normal metal within a sheet of thickness ξ_n. This length is called the *normal coherence length* where Cooper pairs enter the normal metal.

4.2 Ferromagnet/superconductor bilayer

As shown in the previous sections superconductor is characterized by Cooper-pairs whose participating charge carriers have opposite spin and momentum. Whereas ferromagnets is characterized by parallel alignment of magnetic moments. Both ordering phenomena are antagonistic by nature [96–98].

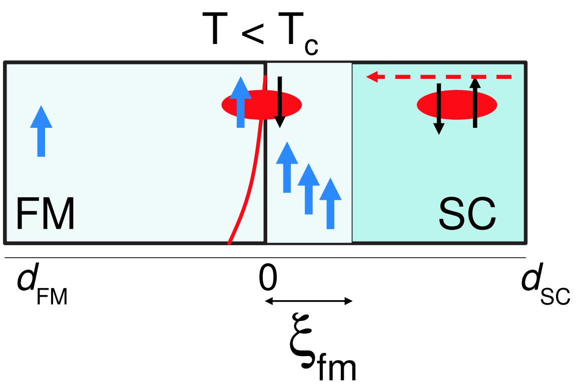

Figure 4.2: Schematic diagram of the order parameter at the interface between a ferromagnet and a superconductor at $T \ll T_c$. The spin-polarized quasiparticle not only quenches the order parameter to penetrate into FM but also diffuses into the SC side with the diffusion length $\xi_{\rm fm}$.

The basic mechanism behind this antagonism is two-fold: the electromagnetic behavior of the superconductor, and the effect of exchange correlations in breaking Cooper-pairs. In the presence of sufficiently weak magnetic fields, superconductors exhibit perfect diamagnetism (Meissner effect). For most ferromagnets, the surface currents required to screen the bulk from the spontaneous magnetization exceed the superconductor critical currents; the possibility of coexistence with superconductivity is therefore limited to very weak ferromagnets. In itinerant-electron systems, the spin-splitting of the electronic spectrum due to the presence of exchange interactions between the band-electrons also has a deleterious effect upon superconductivity [99, 100]. This may be understood with reference to the Stoner model.

In the Stoner ferromagnet, the interaction of the electrons with the internal field $H_{\rm int}$ lowers/raises the energy of the spin↑ (spin↓) electrons by $\mu_\circ H_{\rm int}$ thus, the spin↑ electrons at the Fermi surface have a kinetic energy of $E_{\rm F} + \mu_\circ H_{\rm int}$ whereas the spin↓ electrons have the kinetic energy $E_{\rm F} - \mu_\circ H_{\rm int}$. In order to form a Cooper-pair, two electrons must have a kinetic energy within the Debye frequency $\omega_{\rm D}$ of $E_{\rm F}$. Although assumed to be small the exchange potential $\mu_\circ H_{\rm int} \gg \omega_{\rm D}$. This essentially forbids the Cooper-pairing of electrons in the standard spin-singlet configuration.

In spite of these objections, the coexistence of ferromagnetism and superconductivity has been observed since the late 1960s. In the majority of these systems, however, the ferromagnetism is localized in nature, or the system is divided into non-overlapping ferromagnetic and superconducting regions of mesoscopic dimensions [101, 102].

More recently the discovery of ferromagnetism ($T_{\rm Curie} \approx 135$ K) and superconductivity ($T_{\rm c} \approx 40$ K) in the $\rm RuSr_2GdCu_2O_8$ (Ru1212) compound opens a lot of questions [103–105]. The mechanism responsible for superconductivity in these systems is generally regarded as exotic, the possibility of spin-triplet Cooper-pairing has been raised to describe the apparently cooperative coexistence between superconductivity and ferromagnetism [104, 105].

In case of FM/SC the proximity effect is drastically reduced, due to the destructive action of the exchange energy J_{spin} on the Cooper pairs, this schematically shown in Fig. 4.2. In that case the condensate penetrates into the FM region over a distance of the order of:

$$\xi_{\mathrm{prox}} = \frac{\hbar v_F}{\Delta J_{\mathrm{spin}}}. \tag{4.5}$$

One important property in equation (4.5) for ξ_{prox} into the ferromagnet is the exchange energy J_{spin}, i.e. $\xi_{\mathrm{prox}} \propto \frac{1}{J_{\mathrm{spin}}}$. Each electron of a pair is in a different spin band. These bands are shifted by an energy J_{spin}. Therefore, if J_{spin} is very large the Cooper pair breaks up. In order to have a stronger proximity effect, i.e., weaker exchange fields, experimentalists are using dilute magnetic alloys. For example Cu-Ni alloys have been used in order to observe the change of sign of the Josephson critical current in a superconductor/ferromagnet/superconductor (SC/FM/SC) heterostructure.

Theoretical works on bilayers of metallic ferromagnets and low-temperature superconductors [106, 107] predicted oscillations of the critical temperature T_{c}. This was confirmed by experimental results [108,109]. The oscillating behavior of the superconducting temperature is due to tunnelling of Cooper-pairs into the FM layer [110]. A review on this topic is given by Izyumov et al. [111].

So far, oscillations of the superconducting transition temperature T_{c} in the colossal magnetoresistance CMR / *d*-wave–HTSC superlattices have not been found experimentally [112, 113]. This can be understood from equation (4.5) due to the higher exchange energy $J_{\mathrm{spin}} \approx 3$ eV [114] of the half metal CMR as has been mentioned in previous Chapter 3.

Another interesting effect is the spin-polarized quasiparticle *self* diffusion into the SC layer (the inverse proximity effect) using the exchange energy J_{spin} as driving force. Here, the Cooper pairs share the electrons between the superconductor and the ferromagnet at the interface, see Fig. 4.2. It is discussed that while the spin of the electron in the FM prefers to be parallel to the magnetic moment of the FM the spin of the electron in the SC is automatically antiparallel to the magnetization [115]. In SC a (screening) magnetic moment is induced which penetrates over the characteristic superconducting length ξ_{fm} and this appears as reduction in the saturation magnetization M_{s} of the FM layer. This will be shown experimentally in Chapter 7. For a non-itinerant ferromagnet the effect will be zero or negligible. The reason is that according to the physical picture the electrons involved in this effect are only those of the condensate which, as it is well known, are around the Fermi level. Therefore the screening in the superconductor cannot be determined by the magnetization of the ferromagnet, which involves the integral over all the electrons, but rather by the polarization of the electrons at the Fermi level, see Fig.

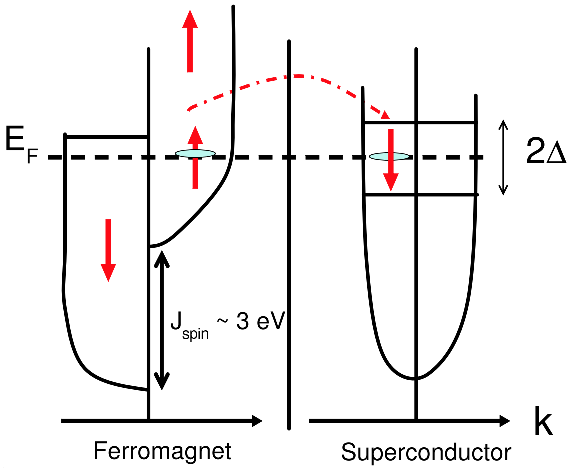

Figure 4.3: Schematic energy band structure of a FM/HTSC bilayer. The FM has a large exchange energy $J_{\text{spin}} \approx 3$ eV. The two electrons connected by a dashed line represent a Cooper pair which contributes to the inverse proximity effect.

4.3.

The pair breaking in CMR/HTSC bilayer due to the self injection of quasiparticles (QPI) into the superconducting layer has also been taken into account [116]. This phenomenon has been very early investigated by Parker [117] and can be written as:

$$\frac{\Delta(n_{qp})}{\Delta(0)} \approx 1 - \frac{2n_{qp}}{4N(0)\Delta(0)} \tag{4.6}$$

where $\Delta(n_{\text{qp}})$ is the energy required to suppress the order parameter of the superconductor due to the density of spin polarized quasiparticles n_{qp}. N(0) and Δ(0) give the density of states and the order parameter at T = 0 K, respectively. n_{qp} is generated by self-injection along the *c*-axis across the highly transparent interface and is governed by the high exchange spin splitting energy of the CMR magnetic layer.

Based on equation (7.3) a theoretical model in addition to the experimental results concerning the (*self diffusion*) of spin-polarized quasiparticles (SPQ) into the superconductor YBCO at T $\ll T_{\text{c}}$ will be shown in section 7.1. In this section it is shown that the spin diffusion length ξ_{fm} from LCMO into YBCO can be determine in the order of 10 nm at low temperatures.

Chapter 5

Experimental techniques and underlying theory

The scope of this chapter is to introduce the techniques exploited in the experimental part of the thesis, namely pulsed laser deposition (PLD) for thin films preparation, magneto–optics, SQUID magnetometery and transport for critical current, magnetization, resistivity measurements.

In section 5.1 a summary of the main aspects of the theory of pulsed laser deposition is given, paying special attention to the ablation mechanism. In section 5.2 the main aspects of the theory of the magneto–optical technique is presented. It is one of the main techniques employed in this thesis, especially the acquisition of the experimental data discussed in section. 7.3. A description of the determination of the critical current density j_c of HTSC is given, whereas for the full description only the main ideas are drawn. In section 5.3 the SQUID magnetometery which is also one of the main technique employed in the thesis work, will briefly be introduced. The photolithography process and the transport technique was employed for resistivity measurements for HTSC this will be shown in Sec. 5.4.

5.1 Pulsed laser deposition

Pulsed laser deposition is a technique for creating thin films. The PLD method of epitaxial thin film growth involves evaporation of a solid target in an Ultra High Vacuum chamber by means of short and high-energy laser pulses [118–120]. In a typical PLD process, ceramic target is placed in a vacuum chamber. A pulsed laser beam vaporizes the surface of the target, and the vapor condenses on a substrate. The main components are a laser, optics, and a vacuum system. Figure 5.1 shows sketch of the PLD setup for in-situ pulsed laser deposition.

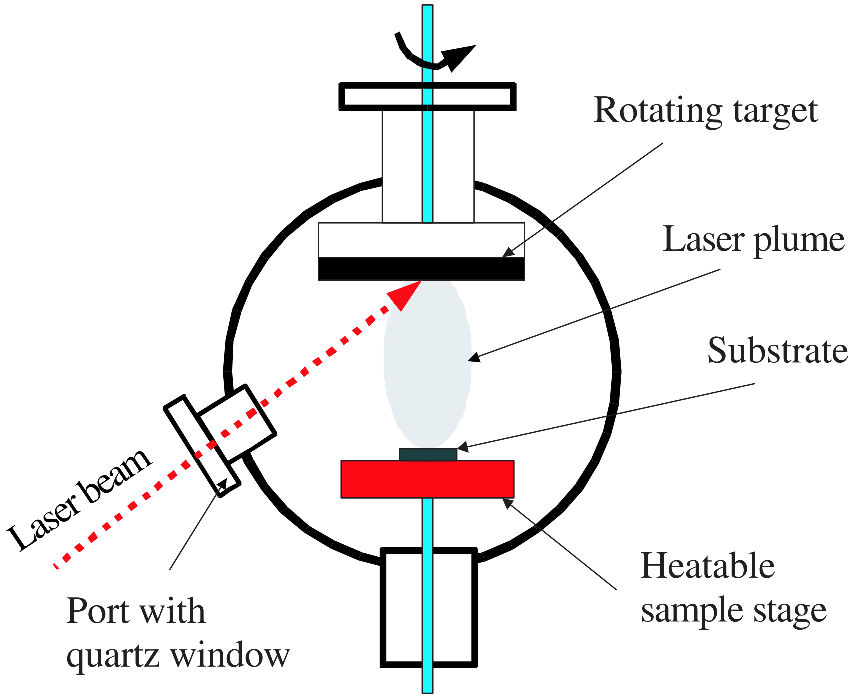

Figure 5.1: Sketch of the experimental setup for in-situ pulsed laser deposition. Small amount of material is ablated from the target by a pulsed laser beam. A plasma is formed, which expands into the vacuum and sublimates onto the heated substrate.

5.1.1 Historical Development of Pulsed Laser Deposition

Using a laser to ablate material has to be traced back to 1962 when Breech and Cross [121], used ruby laser to vaporize and excite atoms from a solid surface. Three years later, Smith and Turner [122] used a similar laser to deposit thin films. This marked the very beginning of the pulsed laser deposition technique. However, the development and investigations of pulsed laser deposition did not gather the expected momentum. In fact, the laser technology was immature at that time. The availability of the types of laser was limited; the stability output was poor and the laser repetition rate was too low for any realistic film growth processes. Thus the development of PLD in thin film fabrication was slow comparing with other techniques such as MBE, which can produce thin film of much higher quality. The rapid progress of the laser technology [123, 124], however, enhanced the competitiveness of PLD in the following decade. The lasers having a higher repetition rate than the early ruby lasers made the thin film growth possible. Subsequently, reliable electronic Q-switches lasers became available for generation of very short optical pulses. For this reason PLD can be used to achieve congruent evaporation of the target and to deposit stoichiometric thin films. The absorption depth is shallower for UV radiation. Subsequent development led to lasers with high efficient harmonic generators and excimer lasers delivering powerful UV radiation. From then on, non-thermal laser ablation of the target material became highly efficient. Pulsed laser deposition as a film growth technique has attained its reputed fame and has attracted wide spread interest after it has been used successfully to grow high-temperature superconducting films in 1987.

5.1.2 Why is PLD useful?

During the last decade, pulsed laser deposition has been employed to fabricate crystalline thin films with epitaxial quality. Ceramic oxide, nitride films, metallic multilayers, and various oxide superlattices grown by PLD have been demonstrated. Recently, PLD was used to synthesize nanotubes [125], nanopowders [126] and quantum dots [127]. Production-related issues concerning reproducibility [128] and large-area upscaling [129] have begun to be addressed. It may start up another area of thin film fabrication in industry. The advantage of the PLD can be summarized as following:

- ***Cost:*** PLD is cost-effective: one laser can serve many vacuum systems.
- ***Targets:*** The targets used in PLD are small compared with the large size required for sputtering techniques. It is quite easy to produce multi-layered films of different materials by sequential ablation of assorted targets. Besides, by controlling the number of pulses, a fine control of film thickness down to atomic monolayers can be achieved.
- ***Materials:*** Many materials can be deposited in a wide variety of gases over a broad range of gas pressures.
- ***Film stoichiometry:*** The most important feature of PLD is that the stoichiometry of the target can be retained in the deposited films. This is the result of the extremely high heating rate of the target surface (108 K/s) due to pulsed laser irradiation. It leads to the congruent evaporation of the target irrespective of the evaporating point of the constituent elements or compounds of the target.
- ***Fast:*** PLD is fast, high quality samples can be grown reliably in 10 or 15 minutes.

5.1.3 Mechanisms of PLD

The principle of pulsed laser deposition, in contrast to the simplicity of the system set-up, is a very complex physical phenomenon. It not only involves the physical process of the laser-material interaction of the impact of high-power pulsed radiation on solid target, but also the formation of the plasma plume with high energetic species and even the transfer of the ablated material through the plasma plume onto the heated substrate surface.

In general, a pulsed laser beam is focused onto the surface of a solid target. The strong absorption of the electromagnetic radiation by the solid surface leads to rapid evaporation of the target materials. The evaporated materials are highly exited and ionized, as shown schematicly in Fig. 5.1.

Thus, the thin film formation in PLD generally can be divided into the following steps, illustrated in Fig. 5.2. (a) Initial absorption, (b) Target surface heating, (c) Evaporation and plasma heating (1D expansion), and (d) 3D expansion of the gas cloud. After that, Deposition of the ablation materials on the substrate, and nucleation and growth of a thin film on the substrate surface.

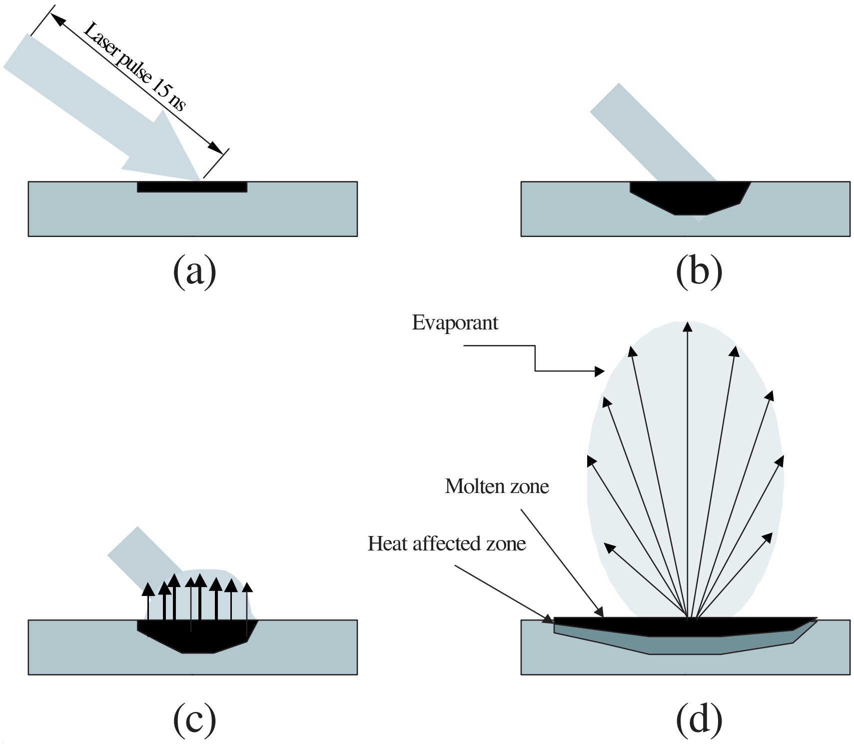

Figure 5.2: Schematic sequence of the laser ablation process in vacuum: (a) Initial absorption, (b) Target surface heating, (c) Evaporation and plasma heating (1D expansion), and (d) 3D expansion of the gas cloud.

Each step in PLD is critical for the formation of high-quality, epitaxial, crystalline, stoichiometric, uniform thin film with small surface roughness.

In the first step, Fig. 5.2a, the laser beam is focused onto the surface of the target. At sufficiently high flux densities and short pulse duration, all elements in the target are rapidly heated up to their evaporation temperature, Fig. 5.2b. Materials are dissociated from the target surface and ablated out with the same stoichiometry as in the target, Fig. 5.2c-d. The instantaneous ablation rate is highly dependent on the fluences of the laser shining on the target. The ablation mechanisms involve many complex physical phenomena such as collisional, thermal, and electronic excitation, exfoliation and hydrodynamics.

During the second step, shown in Fig. 5.3, the emitted materials tend to move towards the substrate according to the laws of gas-dynamic and show the forward peaking phenomenon. The spot size of the laser and the plasma temperature have significant effects on the deposited film uniformity. The target-to-substrate distance is another parameter that governs the angular spread of the ablated materials.

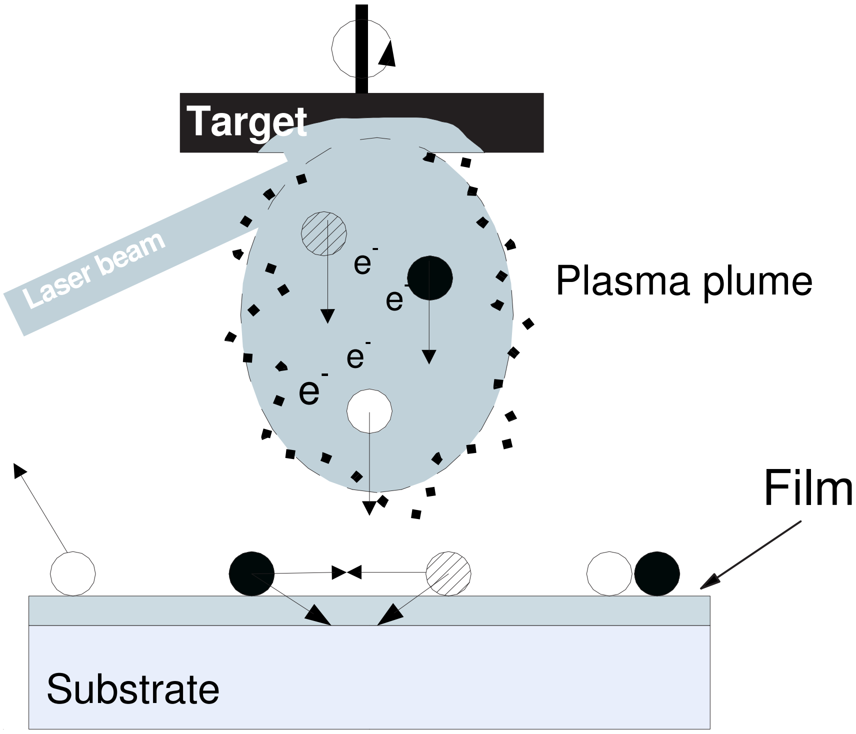

Figure 5.3: Schematic sequence of the nucleation and growth process of the thin film.

The third step is important to determine the quality of the thin film. The ejected high-energy species impinge onto the substrate surface and may induce various type of damage to the substrate.

These energetic species sputter some of the surface atoms and a collision region is formed between the incident flow and the sputtered atoms. The film grows after a thermalized region is formed. The region serves as a source for condensation of particles. When the condensation rate is higher than the rate of particles supplied by the sputtering, thermal equilibrium conditions can be reached quickly and the film grows on the substrate surface at the expenses of the direct flow of the ablation particles and the thermal equilibrium obtained.

Nucleation and growth of crystalline films depends on many factors such as the density, energy, ionization degree, and the type of the condensing material, as well as the temperature and the physico-chemical properties of the substrate. The two main thermodynamic parameters for the growth mechanism are the substrate temperature T_{s} and the supersaturation D_{m}. They can be related by the following equation $D_{\mathrm{m}} = k_{\mathrm{B}}Tln(R/Re)$; where k_{B} is the Boltzmann constant, R is the actual deposition rate, and Re is the equilibrium value at the temperature T.

The nucleation process depends on the interfacial energies between the three phases present, the substrate, the condensing material and the vapor. The minimum-energy shape of a nucleus is like a cap. The critical size of the nucleus is depending on the driving force, i.e. the deposition rate and the substrate temperature T_{s}. For large nuclei, characteristic of small supersaturation, they create isolated patches (islands) of the film on the substrate which subsequently grow and coalesce together. As the supersaturation increases, the critical nucleus shrinks until its height reaches one atomic diameter and its shape is that of a two-dimensional layer. For large supersaturation, the layer-by-layer nucleation will happen for incompletely wetted foreign substrates.

The crystalline film growth depends on the surface mobility of the adatom (vapour atoms). Normally, the adatom will diffuse through several atomic distances before sticking to a stable position within the newly formed film. The surface temperature of the substrate determines the adatom's surface diffusion ability. High temperature favours rapid and defect free crystal growth, whereas low temperature or large supersaturation crystal growth may be overwhelmed by energetic particle impingement, resulting in disordered or even amorphous structures.

Metev and Veiko [132] suggested that t, the mean thickness at which the growing, thin and discontinuous film reaches continuity is given by the formula $t = A(1/R)^{1/3}\exp(-1/T_{\mathrm{s}})$, where R is the deposition rate (supersaturation related), T_{s} is the temperature of the substrate and A is a constant related to the materials.

In the PLD process, due to the short laser pulsed duration ($\approx$ 10 ns) and hence the small temporal spread ($\leq$10 ms) of the ablated materials, the deposition rate can be enormous (10 μm/s). Consequently, a layer-by-layer nucleation is favoured and ultra-thin and smooth films can be produced. In addition the rapid deposition of the energetic ablation species helps to raise the substrate surface temperature. In this respect PLD tends to demand a lower substrate temperature for crystalline film growth.

Table 5.1 shows an overview of typical deposition parameters using the PLD technique for all of the used materials throughout the thesis.

5.2 The magneto–optical technique

Most of the magnetic measurements on superconductors are carried out using integral techniques like SQUID magnetometery, AC susceptibility etc. However, to obtain information like critical current densities or pinning forces from the measurements, assumptions about the local flux distribution must be made; usually this is done by means of critical state models. To verify these models the direct observation of flux distributions is of great interest. Among local techniques, the magneto-optical observation technique offers the unique possibility to observe dynamic processes combined with a relatively high spatial resolution.

Table 5.1: Overview of typical deposition parameters of the all used materials through the thesis. The laser energy 1.6 J/cm^2 was fixed through the preparation.

Material	T_s [°C]	O_2–deposition [mbar]	T_a [°C]	Deposition–rate [Å]
$YBa_2Cu_3O_{7-\delta}$	780	0.4	535	0.9
$La_{2/3}Ca_{1/3}MnO_3$ [1]	800	0.6	535	0.25
$La_{2/3}Sr_{1/3}MnO_3$ [1]	800	0.6	535	0.25
$SrRuO_3$	780	0.4	535	0.35
$LaNiO_3$	780	0.4	535	0.35
$SrTiO_3$	780	0.4	535	0.35

[1] In case of heterostructure the second layer is deposited at T_s = 780°C.

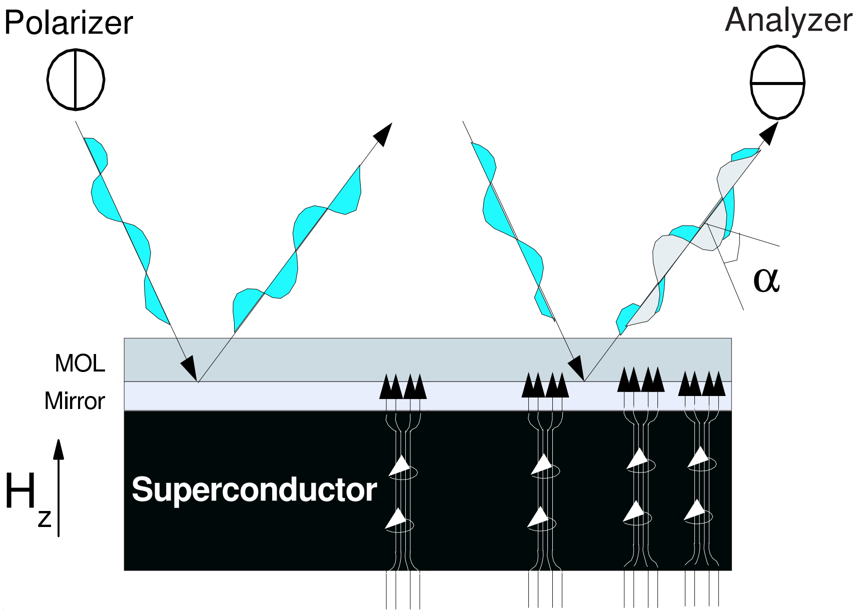

Figure 5.4: The basic principle of the measurement of the magnetic flux distribution of superconductors by the magneto-optical technique.

5.2.1 General description and optimization

The magneto-optical techniques for flux visualization are based on the Faraday effect: in the presence of an external magnetic field $\mu_\circ H_{\text{ext}}$ the propagation velocity of light passing through a medium is different for right and left handed circularly polarized light. For incident linearly polarized light propagating parallel to H_{ext}, as shown in Fig. 5.4, this results in a rotation of the polarization vector over an angle α given by:

$$\alpha = V \cdot l \cdot H_{\text{ext}} \tag{5.1}$$

where l denotes the length of the medium traversed by the light and V is a medium-specific constant, called the Verdet constant. This effect was discovered by Faraday in 1846.

5.2.1.1 Magneto-optical films

A number of different materials have been applied as indicators in MO imaging: cerous nitrate-glycerol, various europium compounds [133] and bismuth-substituted iron garnets [134]. Today, the most popular indicator is the ferri-magnetic bismuth-doped iron garnet film film with in-plane spontaneous magnetization. Application of a perpendicular magnetic field creates an out-of-plane component of the magnetization responsible for the Faraday rotation. A single-crystalline film with a typical thickness of a few microns can be grown by liquid-phase epitaxy on a gadolinium-gallium-garnet (GGG) substrate.

In magneto-optical experiments a thin layer of a material with a large Verdet constant is placed directly above the superconductor. By looking with a polarization microscope at this layer, the spatial variation of the perpendicular component of the local magnetization H_z just above the sample is made visible as an intensity pattern. This is depicted in Fig. 5.5.

Figure 5.5 shows three magneto-optical images of a square–shaped $\mathrm{YBa_2Cu_3O_{7-\delta}}$ thin film with thickness of d = 200 nm, a lateral size of a = 1.5 mm at T = 7 K with different external magnetic fields along z-axis after zero-field cooling: $\mu_\circ H_\mathrm{z}$ = 30, 50, 100 mT (a), (b), and (c) respectively. Bright gray color represents high local fields and black represents small local fields. The images show that an increasing external field leads to the penetration of magnetic flux into the superconductor.

5.2.2 The determination of the critical current density j_c

For a quantitative exploitation of the magneto-optical technique it is necessary to use films with in–plane easy magnetization direction. If a magnetic field H_z is applied normally to the film plane, the in–plane magnetization vector M is rotated out of the film plane by an angle of

$$\phi = \arctan \frac{H_\mathrm{z}}{H_\mathrm{k}} \tag{5.2}$$

H_k represents the anisotropy field of the film. Similar to the paramagnetic MOLs, a linearly polarized light beam propagating normal to the film plane is rotated by an angle α which is proportional to M_z. The presence of a spontaneous magnetization vector, however, causes a non-linear relation between the normal component M_z and the external magnetic field H_ext which gives a Faraday rotation of

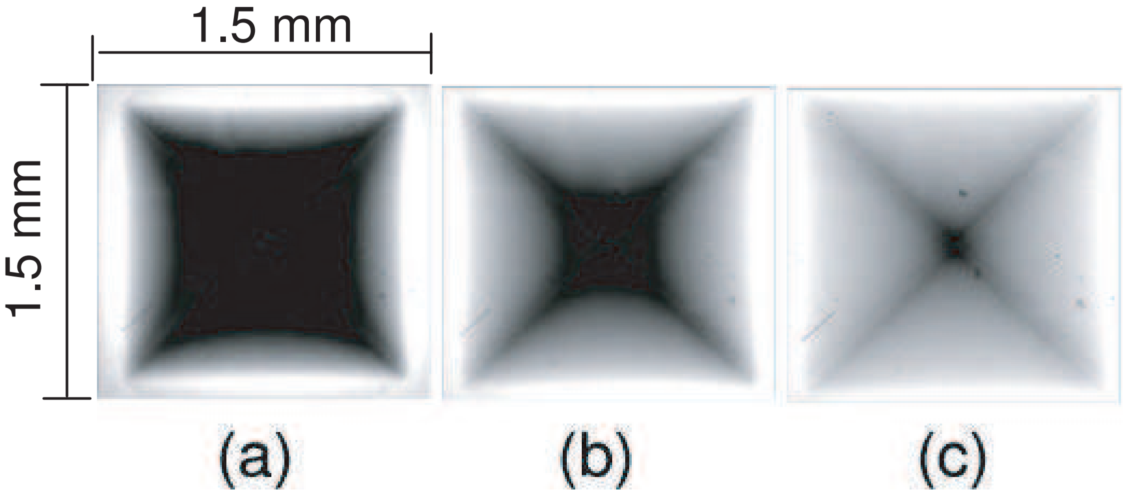

Figure 5.5: Magneto-optical images of a square–shaped $YBa_2Cu_3O_{7-\delta}$ thin film (d = 200 nm, a = 1.5 mm) at T = 7 K. The images are obtained by applying different external magnetic field along z–axis $\mu_\circ H_\mathrm{z}$ = 30, 50, 100 mT (a), (b), and (c), respectively. Bright grey represents high local fields and black represents small local fields.

$$\alpha = cM_\mathrm{z} = cM_\mathrm{s}\sin\phi = cM_\mathrm{s}\sin[\arctan\frac{H_\mathrm{z}}{H_\mathrm{k}}] \tag{5.3}$$

M_s indicates the spontaneous magnetization of the ferrimagnetic film and c is a materialspecific constant similar to the Verdet constant. Note that equation (5.3) is only applicable if the magnetic hysteresis is completely negligible. In order to obtain a high magnetic resolution and a reasonable field range without saturation, the anisotropy field H_k of the iron garnet should be larger than the measured field strengths. Typical values are $\mu_\circ H_\mathrm{k}$ = 100–300 mT.

5.2.2.1 Calibration of the flux density

The calibration of the measured light intensity distribution I(x,y) into a magnetic flux density distribution B_z(x,y) requires a quantitative description of the polarization effects of the MOLs as well as the transfer of a polarized light beam through a polarization microscope. Additional disturbing effects on the polarization vector in a non ideal optical system, such as inhomogeneous illumination of the MOL or polarization effects of optical lenses and mirrors, have to be corrected.

The light intensity I', reflected out of a MOL with thickness d and absorption coefficient γ, is $I' = I_\circ \exp(-2\gamma d)$, where $I_\circ$ represents the intensity of the incident polarized light beam. For an ideal polarization microscope, the light intensity I of a light beam traversing the polarizer, MOL and analyzer is given by the Malus law:

$$I = I_{\circ} \exp(-2\gamma d) \sin^2(\alpha + \Delta\alpha) = I' \sin^2(\alpha + \Delta\alpha) \tag{5.4}$$

where$\Delta\alpha$ denotes the deviation of the polarizer and analyzer from the crossed orientation (90^o). The Faraday rotation α is determined by equations (5.1) and (5.3) respectively, depending on the MOL used. In principle, equation (5.4) allows a calibration of the magneto-optically measured light intensity distribution I(x,y) to a magnetic flux density distribution B_{z}(x,y) at a plane z = constant above the superconductor. A feasible relation is given by equation (5.5) which is directly derived from (5.4). However, for the application of equation (5.5) the deviations due to the non-ideal optical set-up have to be taken into account.

$$B_z(x,y) = B_k \tan[\arcsin(\frac{1}{cM_s} \arcsin\sqrt{\frac{I(x,y) - I_1(x,y)}{I'(x,y)}}) + \Delta\alpha)] \tag{5.5}$$

Practically, the determination of calibration curves at each images position (x,y) is impossible. One determines a calibration curve at one position (x = a, y = b) within the image by measuring $I(H_{\mathrm{ext}})$ for an external field $H_{\mathrm{ext}} \parallel$ z. Afterwards, the function (5.5) is fitted to the measured $I(H_{\mathrm{ext}})$ curves with the fit parameters I' and$\Delta\alpha$. I_1(x,y) is a background image, which has to be subtracted from the I(x,y) data and the spatial distribution of the light reflected from the MOL I'(x,y) may be determined by normalization of the background image I_1(x,y) to I'(x,y) = I_1(x,y)I'(a,b)/I_1(a,b). Here (x = a, y = b) indicates the position within the image, where the calibration curve has been recorded.

Having determined all parameters and the distributions I_1(x,y) and I'(x,y), a spatially dependent calibration according to equation (5.5) is applied to the measured MO contrast I(x,y), in order to obtain the flux density distribution B_{z}(x,y). This now shown in Fig. 5.6.

Figure 5.6 shows the measured flux distribution (after calibration) of a square-shaped $YBa_2Cu_3O_{7-\delta}$ film (d = 200 nm, a = 1.5 mm) with application of an external field after zero–field–cooling of $\mu_{\circ} H_{\mathrm{ext}}$ = 50 mT at T = 7 K.

5.2.2.2 Determination of supercurrents

Imaging of the magnetic flux density distribution at the surface of superconductors provides qualitative insights into flux pinning and supercurrent distributions. In many cases, however, it is desirable to obtain quantitatively the magnitude and the directions of the flowing shielding and critical current densities. The general relation between the measured flux density distribution and the flowing supercurrent density j is given by Ampère's law

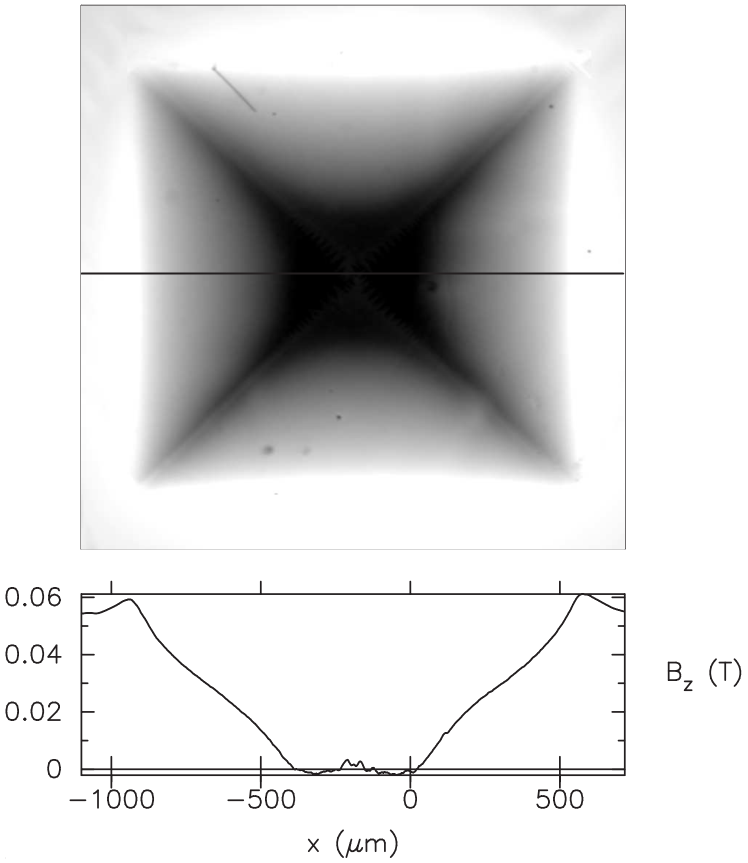

Figure 5.6: The measured flux distribution (after calibration) along the horizontal line for a square-shaped $YBa_2Cu_3O_{7-\delta}$ film (d = 200 nm, a = 1.5 mm) after application of an external field of $\mu_\circ H_{\rm ext}$ = 50 mT at T = 7 K.

$$\mu_\circ j = \nabla \times (B - \mu_\circ H_{\rm ext}). \tag{5.6}$$

In most flux imaging experiments, one has flat samples with finite sizes and the flowing supercurrent generates magnetic self-fields with strongly curved field lines. Consequently, the application of the original Bean model which is valid for long samples in parallel fields is not possible. It relates the current density to gradients in the parallel component of B and completely neglects the gradients of the other (curved) field components according to equation (5.6). However, for the application of Ampère's law one has to measure the spatial distribution of all three components of $B = (B_{\rm x}, B_{\rm y}, B_{\rm z})$. Even if it is in principle possible to measure in-plane components of B by applying the transverse Faraday effect, it is in practice difficult to measure their gradients by means of magneto-optics.

But it is sufficient for most practical situations to measure the normal component $B_{\rm z}$ at the sample surface if one proceeds from the local relation (5.6) to the integral relation between j and B.

The Biot–Savart law, representing the reversed Ampère's law, gives the integral relation between the current density and the magnetic field. For the measured B_z-component of the magnetic flux density one has

$$B_z(r) = \mu_\circ H_{ext} + \frac{\mu_\circ}{4\pi}\int_v \frac{j_x(r\prime)(y-y\prime) - j_y(r\prime)(x-x\prime)}{\mid r - r\prime \mid^3} d^3r\prime \tag{5.7}$$

The measurement of the perpendicular flux density distribution B_z(x,y,z) above the superconductor surface enables the determination of the planar current density j(x,y,z) = $e_x j_x$(x,y,z) + $e_y j_y$(x,y,z). Equation (5.7) may be used in two different ways for the quantitative analysis of the current distribution: either one uses models for the current distribution j(x,y) and compares the calculated B_z(x,y) distributions with the measured ones; or one directly inverts equation (5.7) by numerical methods. The latter provides a model independent method for the determination of j(x,y). In order to obtain an unambiguous mapping of the measured B_z(x,y) to j(x,y), the following additional restriction has to be considered: The determination of two current density components j_x and j_y from one measured field component B_z requires an additional relation between j_x and j_y, notably,

$$\nabla \cdot j = 0 \tag{5.8}$$

For an isolated superconductor where the supercurrents are created in a magnetization experiment in external magnetic fields, this is directly evident: the current streamlines are closed and one has no sources and drains for the current. Equation (5.8) is, however, also valid for transport currents which are transmitted through a superconductor. Due to the limited measurement area for B_z(x,y) in the x–y plane equation (5.8) cannot be applied at the image borders of the magneto-optical images.

Figure 5.7 shows the numerically calculated current density using Biot–Savart inversion. The left part (a) shows again a gray scale representation of the flux density with superimposeed current stream lines. It can clearly be seen that the direction of the currents is governed by the geometry of the film. The right image (b) shows a gray scale representation of the modulus of the current density. The two profiles below give the current density values j_y and $\mid j \mid$ along the solid black lines, respectively. This $YBa_2Cu_3O_{7-\delta}$ sample show j_c = 3×10^{11} A/m^2, this value is regarded as a standard for high quality YBCO thin films in literature.

5.3 SQUID magnetometery

The Superconducting QUantum Interference Device (SQUID) magnetometery may be the most sensitive measurement device known. It can measure magnetic flux of three

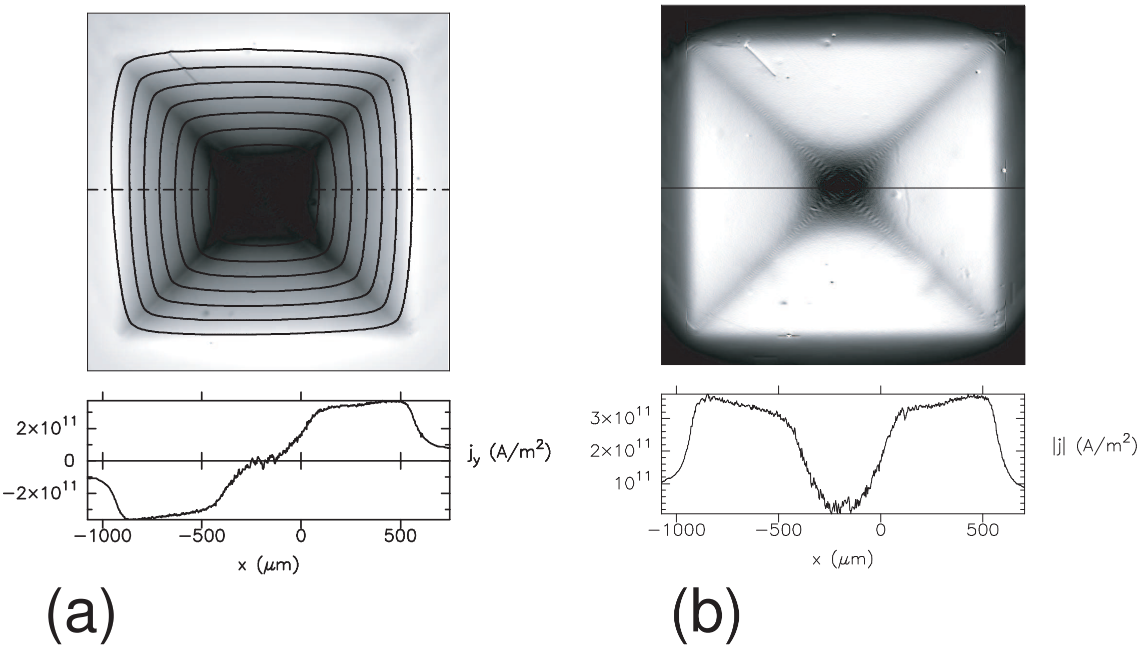

Figure 5.7: Numerical calculation of the current density distribution for the sample shown in Fig. 5.6. The current streamlines are shown in (a) and the current density profiles of j_c (b) are given at the positions of the black, horizontal lines.

orders of magnitude smaller than one flux quantum $\phi_\circ = \frac{h}{2e} = 2.0678\times10^{-15}$ Tm^2. A flux quantum can be visualized as the magnetic flux of the Earth's magnetic field (0.5 Gauss = 0.5× 10^{-4} Tesla) through a single human red blood cell (diameter about 7 microns).

It can measure extremely tiny magnetic fields. The energy associated with the smallest detectable change in a second, about 10^{-32} Joules, is about equivalent to the work required to raise a single electron 1 millimeter in the Earth's gravitational field.

The sensitivity of the basic SQUID can be increased by attaching it to a flat coil of superconducting wire, such as niobium. Called a "flux transformer", this increases the current induced in the junction and permits the detection of magnetic fields as small as 10^{-15} Tesla or one femto-Tesla. This is a resolution of some 10^{-11} times the Earth's magnetic field. By comparison, the auroral displays in Earth's polar region produce magnetic field fluctuations on the order of 1% of the Earth's field.

Taking 1 fT as the nominal resolution of the SQUID, it is capable of detecting changes in magnetic fields in the human body: Threshold for a SQUID: 1 fT, magnetic field of the heart: 50,000 fT, magnetic field of the brain: a few fT.

In Fig. 5.8 a sketch of a SQUID is shown. It consists of two superconductors separated by thin insulating layers to form two parallel Josephson junctions. The SQUID has as its active element one or more Joesphson junctions. A Josephson junction is a weak link between two superconductors that can support a supercurrent below a critical value I_c. The special properties of the Josephson junction cause the impedance of the SQUID loop

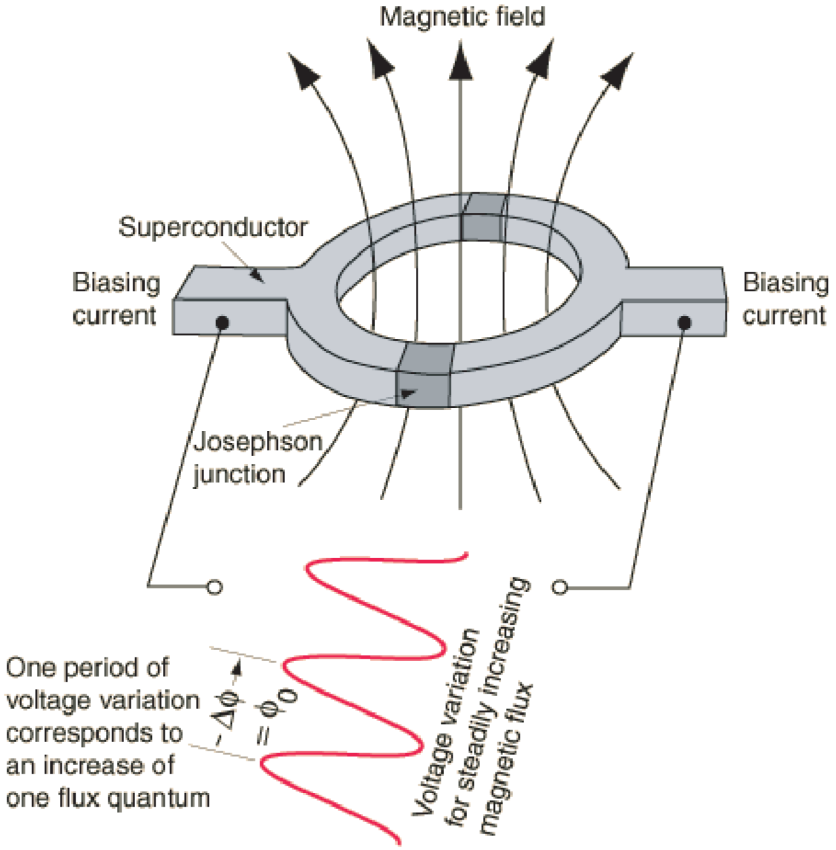

Figure 5.8: The superconducting quantum interference device (SQUID) consists of two superconductors separated by thin insulating layers to form two parallel Josephson junctions.

to be a periodic function of the magnetic flux threading the SQUID so that a modulation signal supplied to the bias current is used with a lock-in detector to measure the impedance and to linearize the voltage-to-flux relationship. The net result is that a SQUID functions as a flux-to-voltage converter with unrivaled energy sensitivity.

In most practical systems in use today, the SQUID is located inside a small cylindrical, superconducting magnetic shield in the middle of a liquid helium dewar. Superconducting pickup coils, typically configured as gradiometers that detect the difference in one component of the field between two points, are located at the bottom of the dewar, and the subject is placed beneath the magnetometer.

Resolutions on the order of 30 fT have been achieved with the $YBa_2Cu_3O_{7-\delta}$ type high-temperature superconductors with which the SQUID can be operated at liquid nitrogen temperature.

5.4 Photolithography and transport measurements

In this section the experimental methods used to obtain the photolithography process and transport measurements will be briefly discussed.

5.4.1 Photolithography process

Photolithography, literally meaning light-stone-writing in Greek, is the process by which patterns on a semiconductor or other material can be defined using light. It is the means by which the small-scale features of integrated circuits are created.

Before the resist is applied to the substrate (film + substrate), the surface is cleaned to remove any traces of contamination from the surface such as dust, organic, ionic and metallic compounds. The cleaned film is subject to priming, to aid the adhesion of the resist to the surface of the substrate material. Figure 5.9, shows the process schematically.

A resist is applied to the surface using a spin-coating machine. This device holds the substrate, using a vacuum, and spins it at high-speed (3000–6000 rpm) for a period of 15-30 seconds. A small quantity resist is dispensed in the center of the spinning substrate. The rotation causes the resist to be spread across the surface of the substrate with excess being thrown off. Close to the center of the substrate, the variation in the thickness of resist is around 30 nm. Preparation of the resist is concluded by a pre-bake, where the substrate is heated in a convection oven and then on a hotplate to evaporate the resist solvent and to partially solidify the resist.

The photomask is created by a photographic process and developed onto a glass substrate. The cheapest masks use ordinary photographic emulsion on soda lime glass, while Chrome on quartz glass is used for the high-resolution deep UV lithography.

The alignment of the mask is critical and must be achieved in for x-y as well as rotationally. Industrial photolithography machines use automatic pattern recognition to achieve the registration alignment.

Depending on the design of the photolithography machine, the mask may be in contact with the surface, very close to the surface or used to project the mask onto the surface of the substrate. These methods are called, contact, proximity and projection, respectively. Figure 5.9, shows a schematic diagram of the proximity method. The limit of the feature size is limited by the diffraction limit and depends on the size of the wavelength of light used to illuminate the mask. Systems using UV light are limited to feature sizes of 1 μm.

During the exposure process, the resist undergoes a chemical reaction. Depending on the chemical composition of resist, it can react in two ways when the light strikes the surface. The action of light on a positive resist causes it to become polymerized where it has been exposed to the light. A negative resist has the reverse property. Exposure to UV-light causes the resist to decompose. After the developing process, a negative of the mask remains as a pattern of resist. Although not necessary for all processing, to further harden

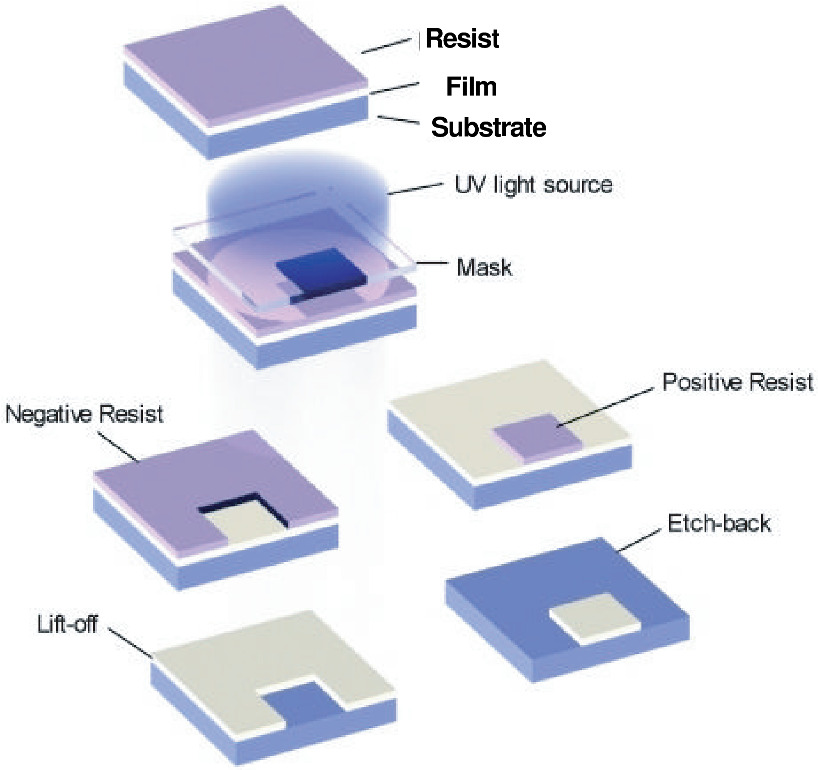

Figure 5.9: The main processes in the photolithography using the proximity method.

and remove any residue of the developer, the substrate undergoes a post-bake process. During this process, the resist temperature can be controlled to cause a plastic flow of the resist which can be desirable for tailoring sidewall angles. After either, deposition of gold layers or metal or etching down to selectively remove parts of the film, the resist can be removed. For positive photoresists, acetone, trichloroethylene and phenol-based strippers may be used. While negative resists are generally removed using, Methyl Ethyl Ketone (MEK) or Methyl Isobutyl Ketone (MIBK).

5.4.2 Transport measurements

A four–probe resistance measurement is a technique for determining the resistance of low resistance material. Unlike two probe resistance measurements where the voltage drop is measured by the same probe that does the current excitation, the four probe technique separates the voltage drop measurement probes from the current excitation probes. This separates the probe resistance from the actual sample resistance measurement. For low resistance measurements, such as for highly conductive metals and especially for superconductors, it is necessary to perform the resistance measurement using a four probe technique.

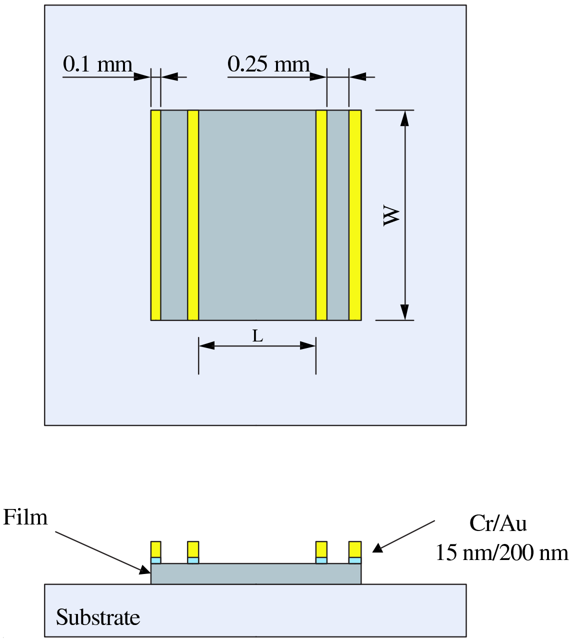

Figure 5.10: Sketch of the chosen sample geometry for four–probe measurements. The film is grown by pulsed laser deposition onto 5×5 mm^2 $SrTiO_3$ (100) single crystalline substrates. By means of chemical lithography the 5×5 mm^2 film area is etched down to 3×3 mm^2. Afterwards, 15 nm/200 nm Cr/Au are evaporated on top of the film as contacts for the attachment of Au wires.

Transport measurements since measuring the current-voltage characteristics by a four–probe method is a forward experimental technique, only some comments concerning the measurements on high–T_c superconductors materials will be made.

Probing the resistivity or the critical current density of $YBa_2Cu_3O_{7-\delta}$ thin films can be difficult because of high critical current densities that are exhibited at low temperatures and fields (j_c = 3×10^{11} A/m^2). As a result, low–ohmic current contact areas are necessary to prevent heating of the sample. This is accomplished by the thermal evaporation of Cr/Au (15 nm/200 nm) after the classical lithography method shown before. The contacts can then be realized by applying Ag-paint for the Au wire of 100 μm in diameter followed by a treatment at 150 $^\circ C$ for one hour. This way leads to a contact resistance of $R < 1\Omega$. Nevertheless, at low temperatures some heating of sample is observed $<$ 0.5 K. To prevent a possible heating of the sample, an intermittent measuring technique was employed. The current provided by a programmable *Keithley*–220 current source was reversed +/- with a time delay of 10 s. Close to the end of this interval the voltage was recorded by a *hp*–8440 nano–voltmeter, typically 2 times. After switching off the current, the background voltage was recorded and subtracted from the measured value. With this method +/- voltage are identical; close to noise level ($\leq$ 1 μV/cm). For the measured value the average between the +/- voltages $V_m = (V^+ - V^-)/2$ is taken. Knowing the real voltage values the resistivity of the film ρ can determined; $\rho = \frac{R \cdot A}{L}$; where the film area $A = d \times W$; d is the film thickness, W is the film width, and L is the distance between the voltage contacts, as shown in Fig. 5.10.

Chapter 6

Structural analysis of FM/HTSC heterostructure

In the first part of this chapter a structural data–base of all of the materials used in the thesis will be given. Afterwards, detailed results obtained by x-ray diffraction (XRD), atomic force microscopy (AFM), and high resolution transmission electron microscopy (HRTEM) are presented for bilayers and heterostructures. The crystalline and morphological properties of $YBa_2Cu_3O_{7-\delta}$ films deposited on $La_{2/3}Ca_{1/3}MnO_3$, $SrRuO_3$, and $LaNiO_3$ buffered $SrTiO_3$, $LaSrAlO_4$ and $LaSrGaO_4$ substrates are studied for various $YBa_2Cu_3O_{7-\delta}$ thicknesses and a fixed buffer layer thickness of d = 50 nm. Films deposited at T_s = 780^oC show the best superconducting properties. AFM on these films revealed uniform and well-connected grains.

6.1 Introduction

Selecting a substrate to grow a film on top there are a number of factors that are important. The selection of substrates for high temperature superconductors, which applies to the case of manganites as well, has to obey a several of conditions. Ideally the substrate should provide only mechanical support but not interact with the film except for sufficient adhesion, and in many cases the provision of a template for atomic ordering [135]. A list of important factors for general film growth and for epitaxial growth include.

- *Chemical stability and/or interdiffusion*. It is important, that there is no chemical reaction between film and substrate. Also, there should not be any reaction between the substrate and the oxygen atmosphere that is necessary to grow high–T_c superconducting or colossal magnetoresistive materials.

- *Match of thermal expansion coefficients*: If substrate and film have different thermal expansion coefficients they causes interfacial strain with the possibility of cracking of the film. A mismatch causes larger problems for films made out of brittle material. Also, a thinner film might conform to the substrate in situations where a thicker film will crack.

- *Surface quality*: A uniform surface is necessary in order to get a homogeneous film. Defects on the film surface can have a significant impact on the nucleation of the film and can influence the film morphology and structure [136].
- *Substrate cleanliness*: A clean surface is a requirement for reproducible results. Usually the cleaning procedure is a consequence of an empirical process. A good way is to put the substrate in acetone in an ultrasonic bath and dry it in argon flow. Any organic remains will be dissociated during the pre-deposition heating.
- *Substrate homogeneity*: If the substrate consists of a small amount of another phase than the predominant one, this might affect the surface and the film may not grow well on the whole substrate. Twin boundaries that propagate throughout the substrate are potential nucleation sites for competing crystalline directions.
- *Substrate thermodynamic stability*: It is important that the substrate does not undergo any phase transitions in the temperature range that is spanned during the preparation and growth process.

In order to grow epitaxial films there are more factors to be considered. Epitaxial means that there is a definite relation between the orientations of film and substrate.

- *Lattice match*: The difference of the in-plane lattice parameters should be minimized to get epitaxial films. Differences in lattice parameters generate strain and misfit dislocations and thus modify the properties of the film.
- *Coincidence sites*. Not only the lattice constants should be matched but the atoms that coincide should preferably have the same atomic size and valency. This means that a good substrate should have a similar structure to the film material.
- *Surface quality*: For epitaxial films this factor is even more important. Mis-oriented grains frequently nucleate on irregularities on the surface.
- *Structural quality*: Generally, one can say that the crystalline quality of the film will not be better than that of the substrate. Impurity phase inclusions and twins will likely effect the epitaxial quality.

The lattice parameters of cuprates or manganites depend on the dopant and the degree of doping. The $YBa_2Cu_3O_{7-\delta}$ structure depends on the oxygen content and in the $La_{2/3}Ca_{1/3}MnO_3$ manganite the Ca-content plays a crucial role. The composition that will be discussed mostly is listed in Table (6.1).

Table 6.1: The crystal structure data-base for all of the used materials.

Material	Lattice Parameter (nm) a	b	c	Structure	Space Group	ID
$YBa_2Cu_3O_{7-\delta}$	0.3817	0.3883	1.1682	orthorhombic	Pmmm(47)	88-2463
$La_{2/3}Ca_{1/3}MnO_3$	0.3868	0.3858	0.5453	orthorhombic	Pbnm(62)	87-1084
$La_{2/3}Sr_{1/3}MnO_3$	0.3882		1.3324	rhombohedral	R$\overline{3}$c(167)	51-0409
$SrRuO_3$	0.394			cubic		28-1250
$LaNiO_3$	0.3861			cubic	Pm$\overline{3}$m(221)	33-0710

We have mainly used three types of substrates, $SrTiO_3$, $LaSrGaO_4$ and $LaSrAlO_4$. All of these substrates have structures that can be classified as pseudocubic or tetragonal and they have similar structures to high–T_c superconducting and colossal magnetoresistive materials, so the coincidence is good. In Table (6.2) some basic information about the substrates is presented.

Table 6.2: The crystal structure data-base for all of the used substrates and their thermal expansion α.

Material	Lattice Parameter (nm) a	b	c	Structure	Space Group	ID	α $(10^{-6} K^{-1})$
$SrTiO_3$	0.3905			cubic	Pm$\overline{3}$m(221)	86-0178	7.4
$LaSrGaO_4$	0.3843		1.268	tetragonal	I4/mmm(139)	24-1208	10
$LaSrAlO_4$	0.3755		1.262	tetragonal	I4/mmm(139)	24-1125	7.5

An epitaxially grown $YBa_2Cu_3O_{7-\delta}$ thin film on top of a $La_{2/3}Ca_{1/3}MnO_3$ layer grows under tensile strain of $\varepsilon \approx 0.4$ %, where ε can be written as:

$$\varepsilon = \frac{(a_{sub.} \times b_{sub.})^{1/2} - (a_{film} \times b_{film})^{1/2}}{(a_{film} \times b_{film})^{1/2}} \tag{6.1}$$

Figure 6.1 shows the calculated ε values using equation (6.1) for all of the used materials on all used substrates. This is also shown in Table (6.3). All of the used materials grow under tensile strain on $SrTiO_3$ substrates except the $SrRuO_3$ layer. The films on all other substrates are grown under compressive strain as shown in Fig. 6.1. This can give rise to the fact that films grown under *tensile* strain show a reduction of the c-axis lattice parameter. In the other case films growing under *compressive* strain, should show an elongation in the c-axis lattice parameter. The calculation of the ε ratio for YBCO grown on other buffer layers is shown in Table (6.4).

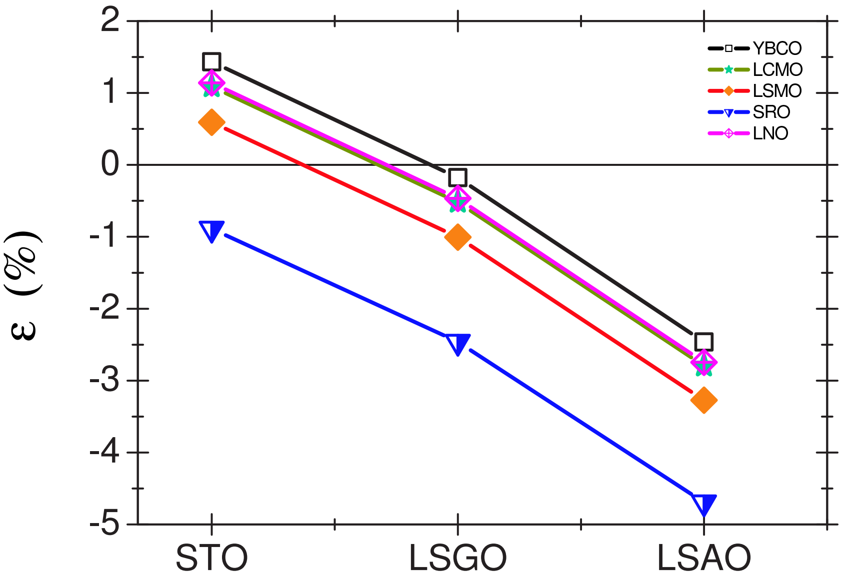

Figure 6.1: The calculated ε using equation (6.1) and the data-base for all of the used materials Table (6.1).

Table 6.3: The strain effect ratio ε calculated using equation (6.1) for all of the grown thin films materials on different substrates that are used in this thesis.

Material	ε (%)		
	STO	LSGO	LSAO
$YBa_2Cu_3O_{7-\delta}$	1.4	-0.2	-2.5
$La_{2/3}Ca_{1/3}MnO_3$	1.0	-0.5	-2.8
$La_{2/3}Sr_{1/3}MnO_3$	0.6	-1.0	-3.3
$SrRuO_3$	-0.9	-2.5	-4.7
$LaNiO_3$	1.0	-0.5	-2.8

Table 6.4: The strain effect ratio ε calculated using equation (6.1) for $YBa_2Cu_3O_{7-\delta}$ thin films grown on different buffer layers.

Material	ε (%)			
	LCMO	LSMO	SRO	LNO
$YBa_2Cu_3O_{7-\delta}$	0.3413	0.8349	2.3414	0.2894

6.2 Structural analysis

6.2.1 X-ray diffraction

X-ray diffraction (XRD) exploites the signal that is generated when an electromagnetic wave enters a crystal and is scattered by the electrons inside. For certain angles of inci-

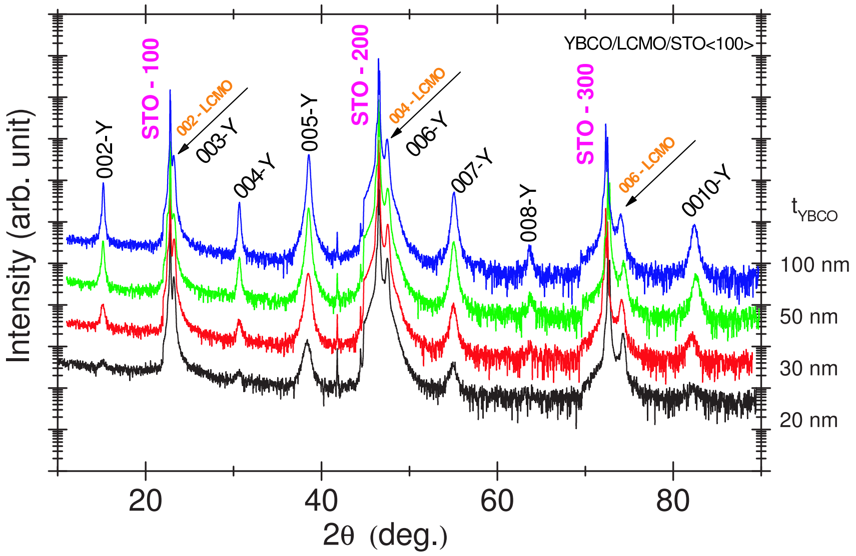

Figure 6.2: θ-2θ XRD scan for the YBCO/LCMO/STO(100) bilayer on a log scan. The thickness is 20 nm–100 nm/50 nm/substrate, respectively.

dence there will be constructive interference between the different scatterers, but for most angles destructive interference will cancel the diffracted beams. By measuring at which angles the constructive interference occurs it is possible to get informations about the geometrical ordering of the atoms inside the crystal. XRD is a useful nondestructive method of structure analysis. The most common uses of XRD in our type of work is: Check, if the sample consists of a single phase. Check the crystallinity of the sample. Is the sample polycrystalline or single–crystal like? Check, if the film is grown epitaxially or textured. Measure the in-plane and out-of-plane lattice parameters to learn more about the interface quality.

The x-ray source used emits Cu-K_α radiation with a wavelength of λ = 0.154056 nm. As detector a scintillation counter is used. Soller slits are used before and after the specimen. They consist of closely spaced parallel metal plates that define and collimate the beam. There is an aperture slit that limits the illuminated area of the sample (0.1×3 mm^2). On the other side of the sample there is an anti-scattering slit that makes sure only refections from the area of the specimen reach the detector. The aperture and the anti-scattering slit should have the same size, so the area that the detector “sees” is the same area that is illuminated. There is also a receiving slit that defines the width of the beam that is admitted to the detector. The size of this slit depends on the wanted resolution. A monochromator crystal is placed in front of the detector, which will reflect radiation with wavelengths different from K_α, mostly K_β, away from the detector. It effectively works as a K_β filter.

6.2.2 $\theta - 2\theta$ scan of bilayers

Different modes of operation of the setup described above lead to a number of different scans that can be performed. In this section XRD is used to characterize high–T_c superconducting /colossal magnetoresistive bilayers that have been prepared in the framework of this thesis. The bilayers consist of 20 nm to 100 nm of $YBa_2Cu_3O_{7-\delta}$ grown on 50 nm $La_{2/3}Ca_{1/3}MnO_3$ deposited on a single crystalline $SrTiO_3$ (100) substrate. The crystalline structure of all used materials is shown in Table (6.1).

The most common mode of operation of XRD is the $\theta - 2\theta$ scan. Here the incidence angle θ is varied, and the detector angle is adjusted to 2θ. This scan allows to see all reflections of all planes that are parallel to the sample surface. A $\theta - 2\theta$ diffraction pattern from the $YBa_2Cu_3O_{7-\delta}$ /$La_{2/3}Ca_{1/3}MnO_3$ /$SrTiO_3$ bilayers is shown in Fig. 6.2. The diffraction peaks observed are all due to YBCO and LCMO and are labelled according to which layer and order of reflection they belong. From this figure it can be seen that the sample consists of a single phase. We observe only (00ℓ) peaks for both layers of YBCO and LCMO, and thus, the film layers and the substrate are c-axis oriented.

For more details the zoom into both the (005)-YBCO and the (004)-LCMO peak is shown in Fig. 6.3a and b, respectively. With thicker YBCO films the width of the (005)-YBCO peak is getting more narrow and more intense, additionally it is shifted to larger angles 2 θ. Using Bragg's law: $n\lambda = 2d\sin\theta$; where d is the interplanar distance, and θ the detector angle divided by 2. We found the c-axis lattice parameter to be c = 1.1770 nm and 1.1653 nm for 20 nm and 100 nm YBCO film thicknesses, respectively. The thinnest YBCO film shows a distinct enhancement of the c-axis lattice parameter which can be explained by a compressively strained film in the ab–plane. Thicker films shows a relaxation of the strain fields and, thus, a c-axis parameter close to the bulk value of YBCO.

Figure 6.3b shows the (004)-LCMO peaks for the 50 nm LCMO buffer layer. Here width, intensity, and 2 θ angle position are approximately the same for all bilayers, as expected for a fixed LCMO film thickness.

Another type of scan is the so called rocking curve, or ω-scan. Here the detector is held at the position of a Bragg peak. The incidence angle is then varied around the θ angle that gives the reflection at that plane. The ω-scan of the (005)-YBCO and (112)-LCMO peaks for a 100 nm YBCO/50 nm LCMO bilayer are shown in Fig. 6.4. The rocking curve gives information about the spread in orientation of the crystallites. A larger spread in the orientation will give a wider rocking curve. The full width at half maximum (FWHM) values for the different curves are given in each figure. The FWHM values are very small compare to literature values for single layers for both peaks which reflects the excellent crystal structure of the films.

So far, only planes that are parallel to the film surface are concerned, so we have no information about the relative orientation of the a and b-axes of the layers. To measure this, one can use a *HKL*-scan, where the sample is rotated around the film plane normal.

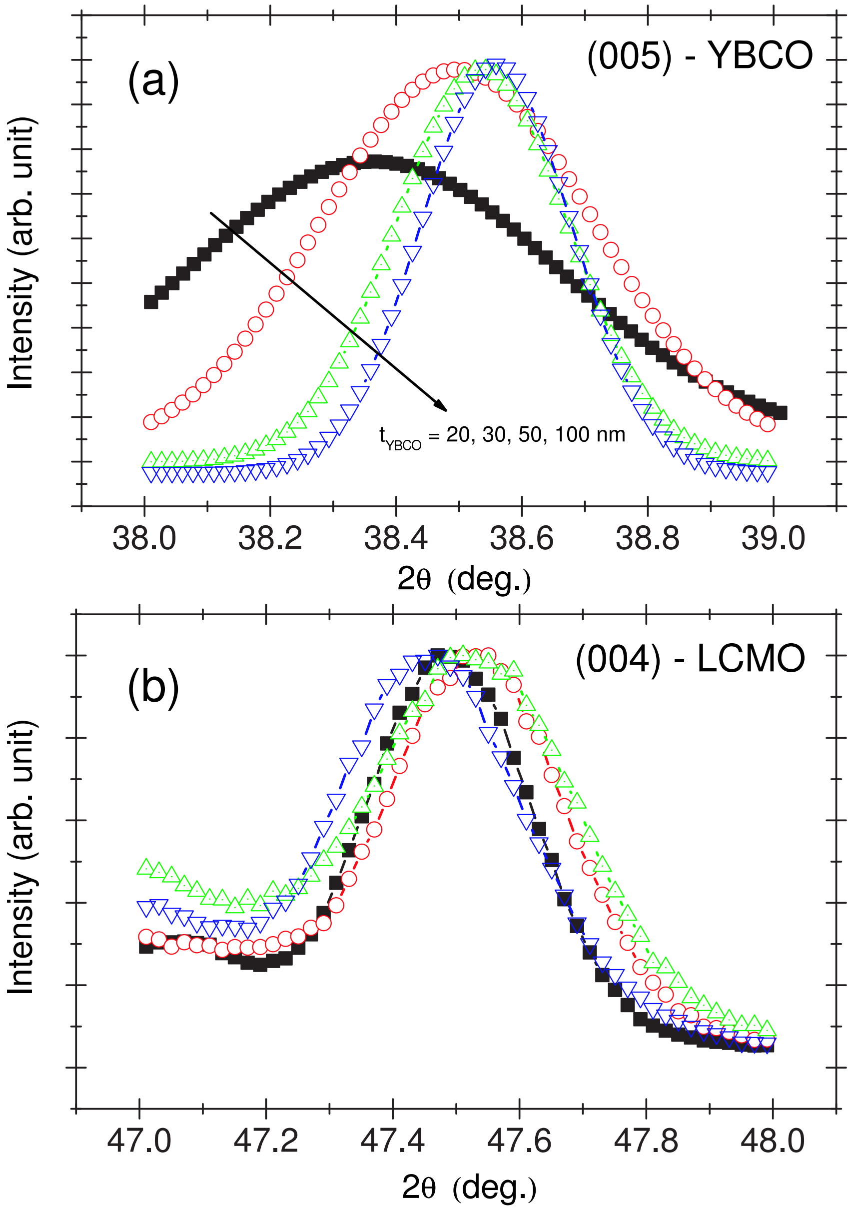

Figure 6.3: The zoom in for (005)-YBCO (a) and (004)-LCMO (b) for the same bilayer as shown in Fig. 6.2.

By setting the θ and 2θ angles in certain positions it is possible to see reflections from planes that do not lie in the film plane. However, reflections will only appear for certain angles. This is determined by the crystal symmetry and the plane that is observed from YBCO and LCMO without overlapping to each other. By observing this kind of reflection from film and substrate it is possible to determine the alignment of the in-plane axes relative. The width of these reflections shows the spread in *in-plane* orientation between different grains like rocking curves do for the film plane normals.

In Fig. 6.5 and 6.6 the *HKL*-scans of a bilayer are shown for two different planes of YBCO and LCMO. The planes are again denoted by their Miller indices. For each of

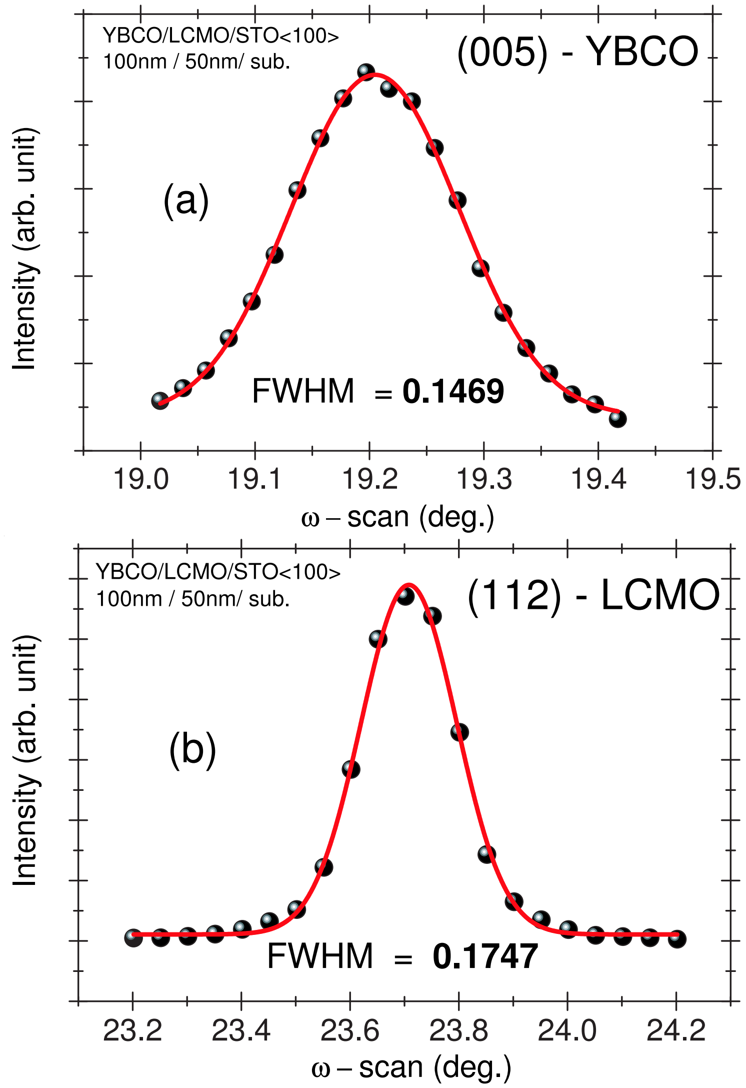

Figure 6.4: ω-scan for (005)-YBCO (a) and (b) for (112)-LCMO reflections. The calculated FWHM values using a Gaussian function (fitting curve) are written inside each figure.

these planes the θ and 2θ angles are set to the corresponding positions (θ, sample and 2θ, detector) then the sample is rotated by 360° around the film surface normal. A first look at the (115)-YBCO peak is shown in Fig. 6.5. The positions coincide with the exact expected reflection position for H and K in-plane scans with a very narrow FWHM of 0.0156 and 0.0096, respectively. The K-scan shows the c-axis projection of FWHM of 0.0147. This means that the YBCO film has its a and b–axis well aligned with the a and b–axis of the substrate.

The (112)-LCMO plane is shown in Fig. 6.6. This plane is rotated 45° relative to the (115)-YBCO planes and it can be seen that a and b–axes of the LCMO layer are also aligned like the YBCO and the STO substrate. So, there is also a good orientation of the lattice axes in the film plane. Because of difficulties in orienting the sample exactly

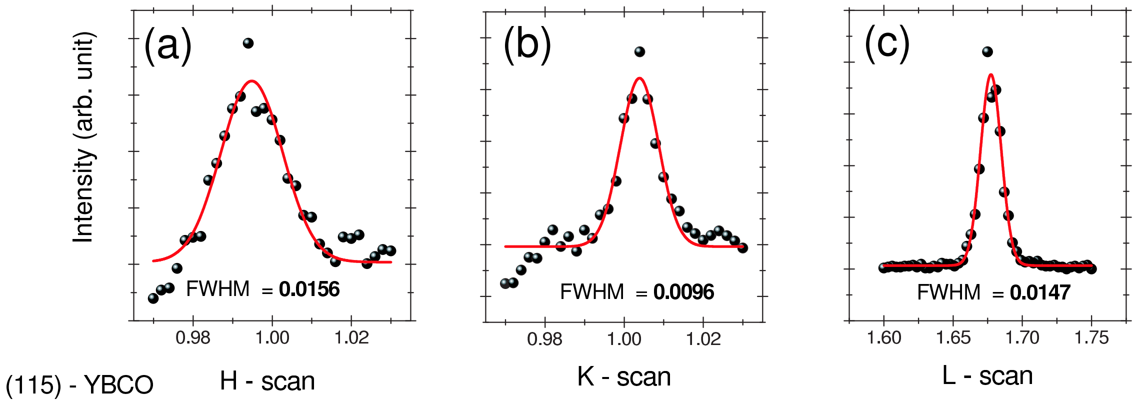

Figure 6.5: *HKL*-scans for the (115)-YBCO reflection. The calculated FWHM values using Gaussian function (fitting curve) are written inside each figure.

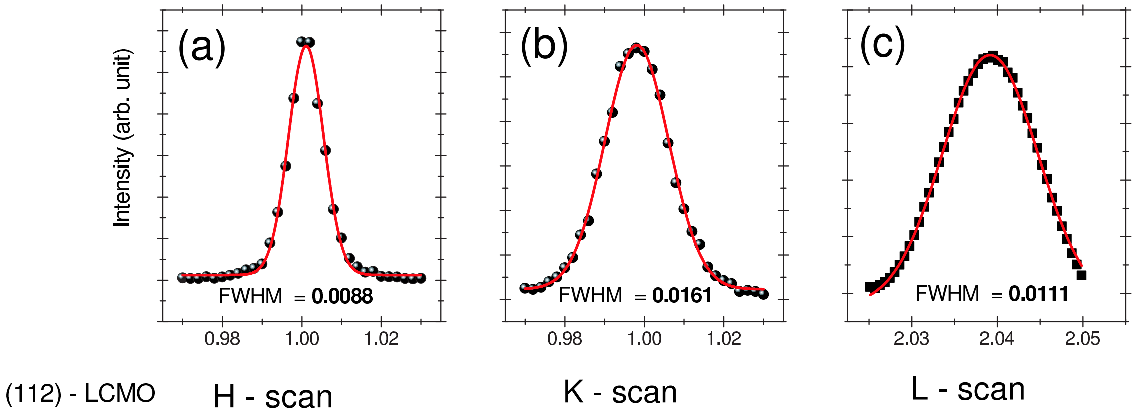

Figure 6.6: *HKL*-scans for (112)-LCMO reflection. The calculated FWHM values using Gaussian function (fitting curve) are written inside each figure.

parallel to the sample holder there are variations in the intensity of the different reflections.

In very thin films the destructive interference will not be complete, and then there are some interesting effects taking place. To examine this, the intensity of a Bragg peak is considered, where we assume that the area of the film is infinite but the thickness is finite:

$$I \approx \frac{\sin^2(kd\cos\theta_B\Delta\theta N)}{\sin^2(kd\cos\theta_B\Delta\theta)} \tag{6.2}$$

The intensity will impose an oscillating function on top of the peak when $\Delta\theta$ is small. If the film is thick, N will be large, and the oscillations will be narrow and averaged out. But if N is small the oscillations will be wider and there will appear satellite peaks around the main reflection, as shown in Fig. 6.7. The positions of the satellites around the main peak can be understood: The sine function has maxima when the argument is $\pm\frac{\pi}{2}$.

$$kd\cos\theta_B\Delta\theta N \approx \pm\frac{\pi}{2}, \tag{6.3}$$

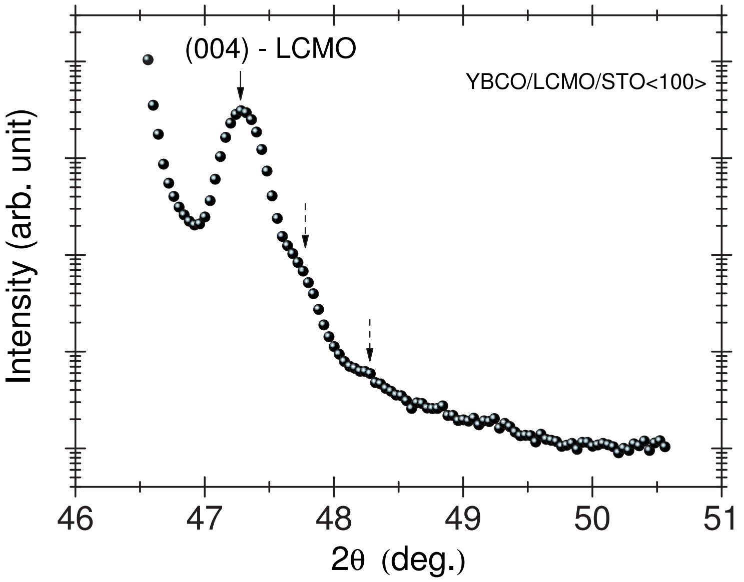

Figure 6.7: θ-2θ-long time scan (120 sec) for (004)-LCMO. The arrows indicate the satellite peaks appearing due to the finite thickness of the film.

which gives

$$2\theta = \frac{\lambda}{2t\cos\theta_B} \tag{6.4}$$

where $t = Nd$ is the thickness of the film and 2θ is the distance between the two peaks closest to the main peak.

In Fig. 6.7 the XRD pattern for a 100 nm YBCO/50 nm LCMO film grown on $SrTiO_3$ (100) is shown. We can see the characteristic oscillations of (004)-LCMO reflection that are discussed before. Using the distance between the two subsidiary peaks closest to the main peak one can calculate the thickness of the film using equation (6.4). We find a calculated thickness of the LCMO of d_{LCMO} = 42±5 nm which in good accordance to the nominal thickness. More important is, that such satellite peaks appear due to the modulation of the film thickness due to the *non*-perfect interface. This gives an information about the interface quality of the bilayers.

6.2.3 Oxygen content of $YBCO_{7-\delta}$ in bilayers

The physical properties of the cuprates in the superconducting and the normal state are largely determined by the density of holes in the CuO_2 planes. In $YBa_2Cu_3O_{7-\delta}$, the structurally adjacent charge reservoir block contains CuO chains, altering the occupancy of the O(1) oxygen chain sites, which affects the density of holes in the planes. Thus, YBCO shows a direct variation of carrier doping through a change in its oxygen composition.

As the doping δ increases, YBCO undergoes a transition from an orthorhombic superconductor to a tetragonal, antiferromagnetic insulator. The variation of the lattice parameters with oxygen doping have been determined by Jorgensen *et al.* [137] who found that the orthorhombic–tetragonal transition occurs at $\delta \approx 0.65$. The c-axis elongates smoothly as a function of δ. While it is possible that the lattice constants of thin films may be affected by epitaxial strain, thin-film studies also show an orthorhombic–tetragonal structural transition between δ = 0.6 and 0.7 and an elongation in the c-axis with increasing δ below the transition. In bulk samples the c-axis lattice parameter is more or less reproducible, and can roughly be used to determine the oxygenation δ. The following empirical formula can be used [138] for this purpose:

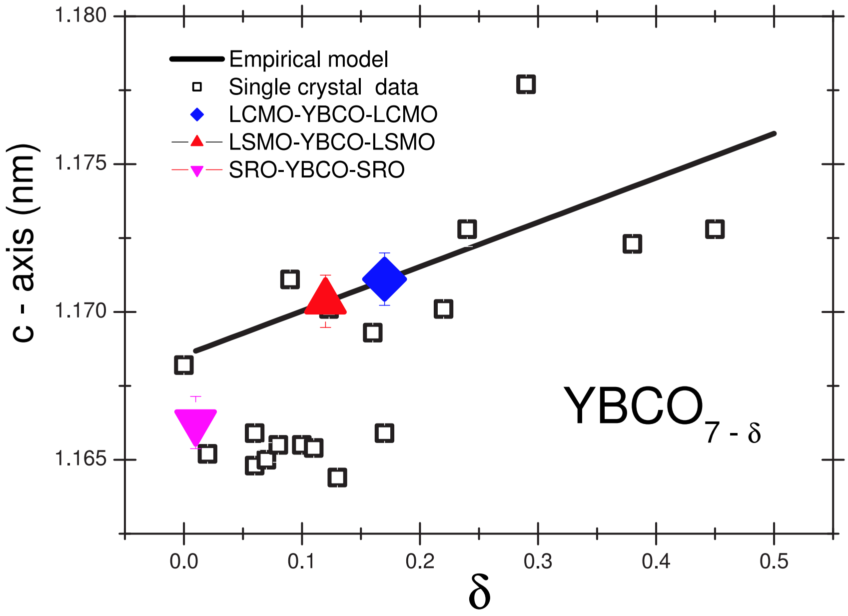

Figure 6.8: The lattice parameter versus doping δ for different single crystals presented in literature is shown. The solid line shows the empirical relation of Tranquada *et al.* [138]. The filled symbols represent the measured c–axis data of different heterostructures that are now put onto the empirical equation.

$$7 - \delta = \frac{12.736 - c}{0.1501} \tag{6.5}$$

Figure 6.8 shows the lattice parameter versus doping δ for different single crystals presented in the structure data-base of YBCO. The solid line shows the empirical relation of Tranquada *et al.* [138]. The filled symbols represent the measured c–axis data of different heterostructures that are now put onto the empirical equation (6.5). This investigation suggests, that the value of δ in these YBCO/manganite heterostructures is about $\delta \approx 0.15$, whereas the SRO heterostructure consists of optimally doped YBCO. This indicates that an adjacent manganite layer leads to an underdoping of YBCO. This information is later needed when the effects of spin–polarized quasiparticles into YBCO are discussed.

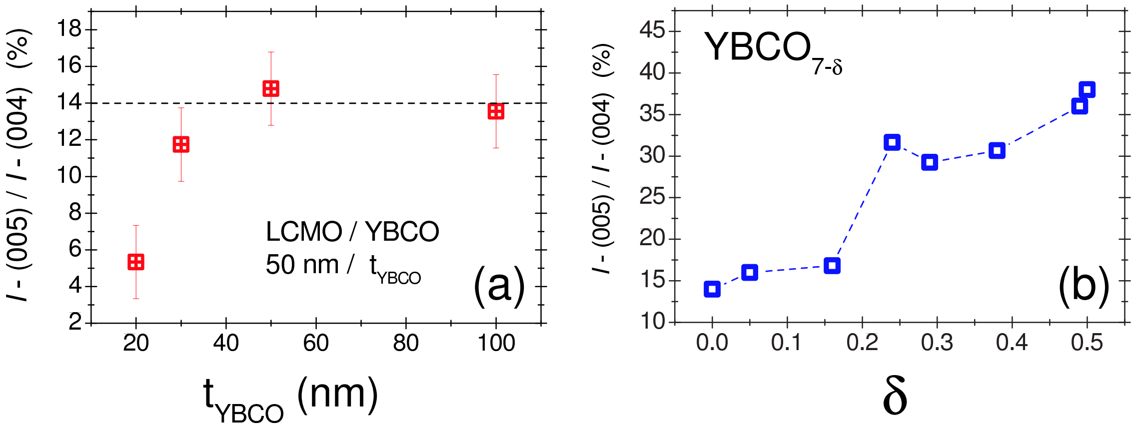

Figure 6.9: (a) Evolution of the relative intensity peaks ratios $I-(005)/I-(004)$ for different YBCO thicknesses grown as cap layer. (b)The relative intensity peaks ratios $I-(005)/I-(004)$ for different YBCO doping values extracted from the data base. Note the saturation of $I-(005)/I-(004)$ in (a) which reflects the stability of the oxygen content of YBCO in bilayers. The lines are guide for the eye.

Another method for determination the oxygenation of YBCO thin films grown as cap layer is the peak intensity ratio of the XRD peaks $I-(005)/I-(00\ell)$ [137, 139, 140]. The peak intensities changes systematically with doping. The relative intensities decrease with doping for ℓ = 2 and 7, whereas they increase for ℓ = 4 and 6. The ℓ = 3 ratio is almost invariant with doping. The most useful information is therefore contained in the ratios of the (004) and (007) peaks. Note, in particular, that the change of the ℓ = 4 and ℓ = 7 ratios is monotonic with doping. A comparison of these results with single crystal data are shown in Fig. 6.9. Notice, that the relative intensity ratios for bulk material is much higher compared to thin films. The different thicknesses of YBCO in bilayers show more or less the same relative intensity ratios. This reflects the stability of the oxygen content of YBCO in the considered bilayers.

Figure 6.9a shows the relative intensity ratio of $I-(005)/I-(004)$ for different thicknesses of a YBCO thin film grown on top of 50 nm LCMO. The same ratio also shown in Fig. 6.9b for the bulk YBCO with different doping values δ for single crystals presented in literature. Notice, the systematic enhancement in the relative intensity ratio as δ increases, Fig. 6.9b, for $I-(005)/I-(004)$.

The differences in $I-(005)/I-(004)$, Fig. 6.9a, are very small for all YBCO thicknesses, especially for the thicker films the values are more or less constant. This reflects an important information about the quality of YBCO as a cap layer, it indicates that the relative peak intensities may be used as reliable estimators of oxygenation. Comparing the saturation value of about 14% in Fig. 6.9a with the values that are found for single crystals in Fig. 6.9b it can be concluded again that δ of YBCO in the considered heterostructures is definitely smaller than $\delta = 0.2$.

6.3 Microscopic analysis using HR-TEM and AFM

After the XRD measurements which focused on the structural properties of heterostuctures in reciprocal space, now the real space properties are investigated by High Resolution Transmission Electron Microscopy (HR-TEM) and Atomic Force Microscopy (AFM).

6.3.1 HR-TEM

High Resolution Transmission Electron Microscopy (HR-TEM) can provide structural information with a spatial resolution of better than 0.2 nm [141]. In most crystalline inorganic materials, including ceramics, semiconductors and metals, the positions of individual atomic columns can be resolved, at least in low-index zones [142]. When recorded under optimum conditions, electron micrographs can be directly interpreted in terms of the projected crystal potential. In other cases, image simulations are necessary to match proposed structures to image features [143]. At lower resolution, amplitude contrast images can be used to observe material features in the 1μm - 0.5 nm range. Possible applications for the HR-TEM can be summarized as follows: Distribution and structure of defects, interfaces and grain boundaries, nano-crystalline features in amorphous films, small particle analysis in heterogeneous catalysts, sub-micron morphological and device features, and thermodynamic decomposition, diffusion and phase transformations.

With this technique, now the interface quality of the heterostructure is investigated. In Fig. 6.10 results for a 25×25 nm^2 scan area of a superlattice with modulation length Λ = (6 u.c. YBCO /5 u.c. LCMO)$_{20}$, where the unit cell denoted by u.c. mainly is the c-axis lattice parameter for each layer and 20 is the number of repeated bilayers. The bottom dark area represent the pure cubic structure of the single crystalline STO substrate. The first grown layer (YBCO) is controlled by the substrates top surface quality as mentioned above. Here, it is seen that in the first bright area YBCO is grown as a continuous line, in the c-axis direction and with good bonding in-plane. The second dark area represents the first LCMO layer. It deserves notice that also continuous interface is seen, in addition to the good in-plane bonding with the YBCO bottom layer. It can be seen that the interdiffusion takes place over *one* unit cell in both sides. The second bright area represents the second YBCO layer. It is seen that the interdiffusion takes place over more than *two* unit cells, but the layered structure of the c–axis oriented YBCO can clearly be seen.

The image shows that both the LCMO and the YBCO layers are grown *cube-on-cube*.

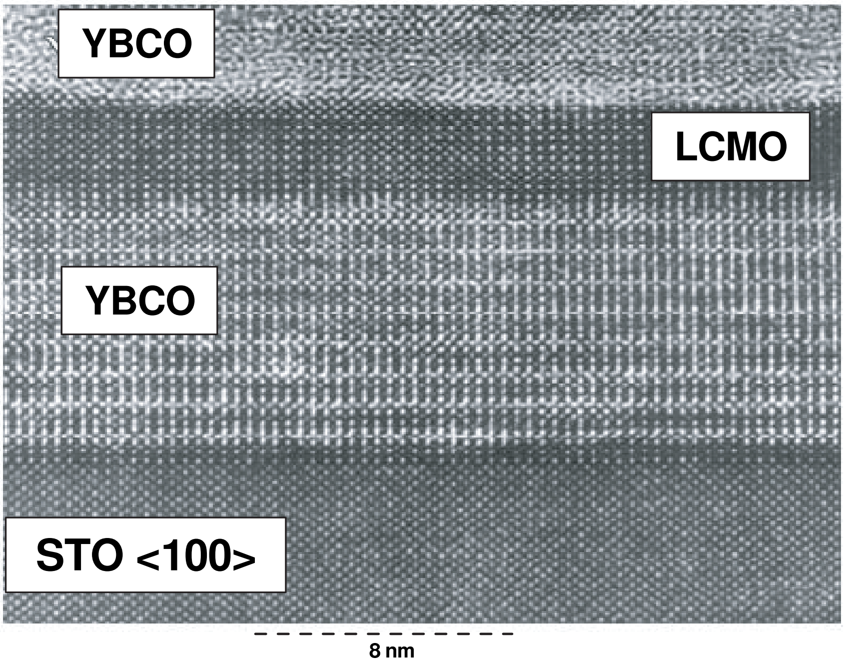

Figure 6.10: HR-TEM pattern for a YBCO/LCMO superlattice (8 nm/4 nm)$_{20}$ after Habermeier et al. [112].

Note, the ***sharpness*** of the interface between YBCO to LCMO layers in the image, which is not found with the same quality for large image areas. Nevertheless, this results agrees with the previous XRD results shown in Fig. 6.5.

6.3.2 AFM

The atomic force microscope (AFM) is one of about two types of scanned-proximity probe microscopes. All of these microscopes work by measuring a local property, such as height, optical absorption, or magnetism with a probe or “tip”placed very close to the sample [145–149]. The small probe-sample separation (on the order of the instrument’s resolution) makes it possible to take measurements over a small area. To acquire an image the microscope scans the probe over the sample while measuring the local property in question. AFM can achieve a resolution of 1 nm, and unlike electron microscopes, can image samples in air and under liquids. In principle, AFM resembles the record player as well as the stylus profilometer. However, AFM incorporates a number of refinements that enable it to achieve atomic-scale resolution: Sensitive detection, flexible cantilevers, sharp tips, high-resolution tip-sample positioning, and force feedback. The growth mechanism and roughness of the each layer in heterostructure is now to be extracted using AFM scan.

In Fig. 6.11 and 6.12 AFM scans of single layer films of YBCO and LCMO grown on $SrTiO_3$ (100) single crystalline substrates with the same substrate deposition temperature (T_d = 770°C) are shown.

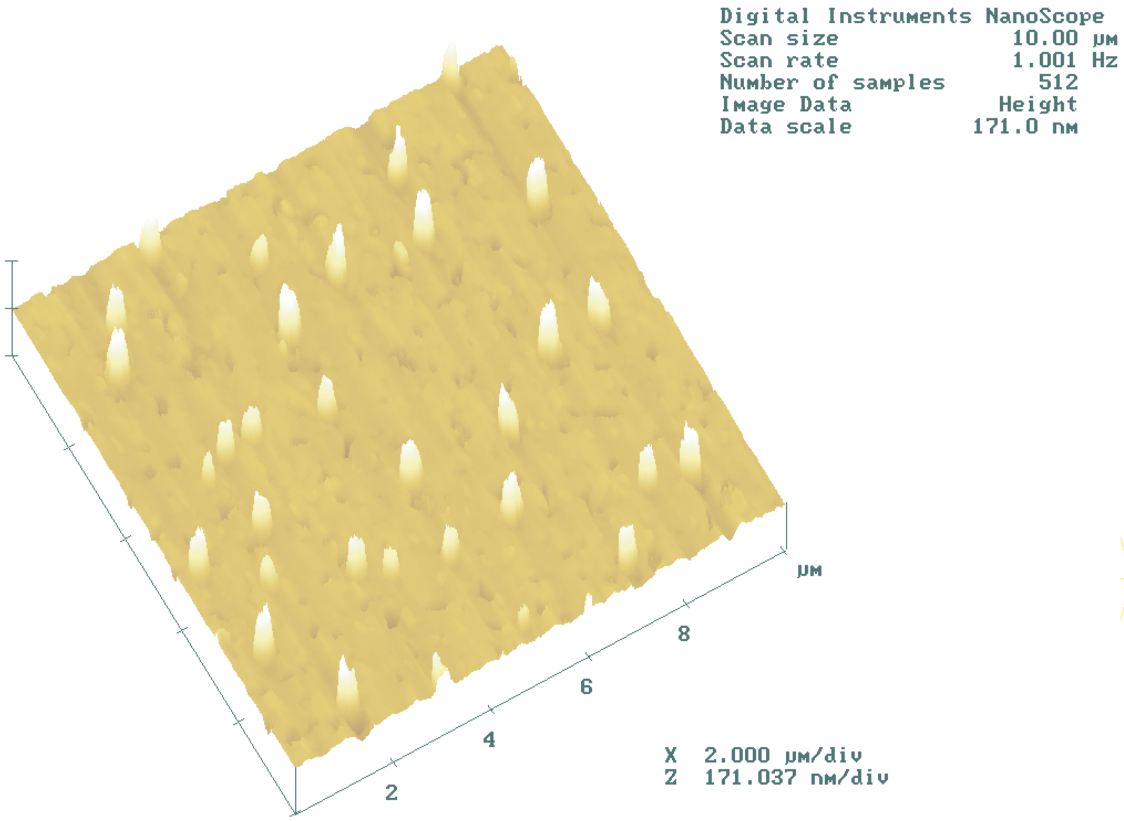

Figure 6.11: AFM image of the surface of YBCO single layer grown on $SrTiO_3$ single crystalline substrate (100). The $10\times10\mu$m scan shows a flat surface disturbed by several irregularly distributed, sharp hillocks with a hight of about 100 nm and a distance of about 1 μm.

The image of the YBCO film in Fig. 6.11 shows a homogeneous and flat surface which is interrupted by non–uniformly distributed surface perturbations with average surface roughness $R_\mathrm{a} \approx 2$ nm. These perturbations look like hillocks with a hight of about 100 nm and an average distance of about 1μm. This kind of surface is typical for the Stranshi–Krastanov growth mode, where the film grows layer–by–layer for the first few unit cells. Afterwards the intrinsic strain fields relax and a columnar and/or island growth establishes. This can be seen at the white structure in Fig. 6.11.

Figure 6.12 shows an AFM image of the surface of LCMO film grown on STO. Here a different topography occurs compared to the YBCO film. The AFM scan shows a smooth surface without perturbations with average surface roughness $R_\mathrm{a} \approx 1$ nm. This is related to the better lattice match of LCMO and STO, $\varepsilon \approx 0.4$ %, compared to YBCO, $\varepsilon \approx 1.4$ %. Here the strain fields in the film during growth are much smaller. That means the layer–by–layer growth can survive longer.

The growth mechanism of YBCO in bilayers or even heterostructures are different compared to single layers due to the fact that the YBCO has now different ε values $\approx$

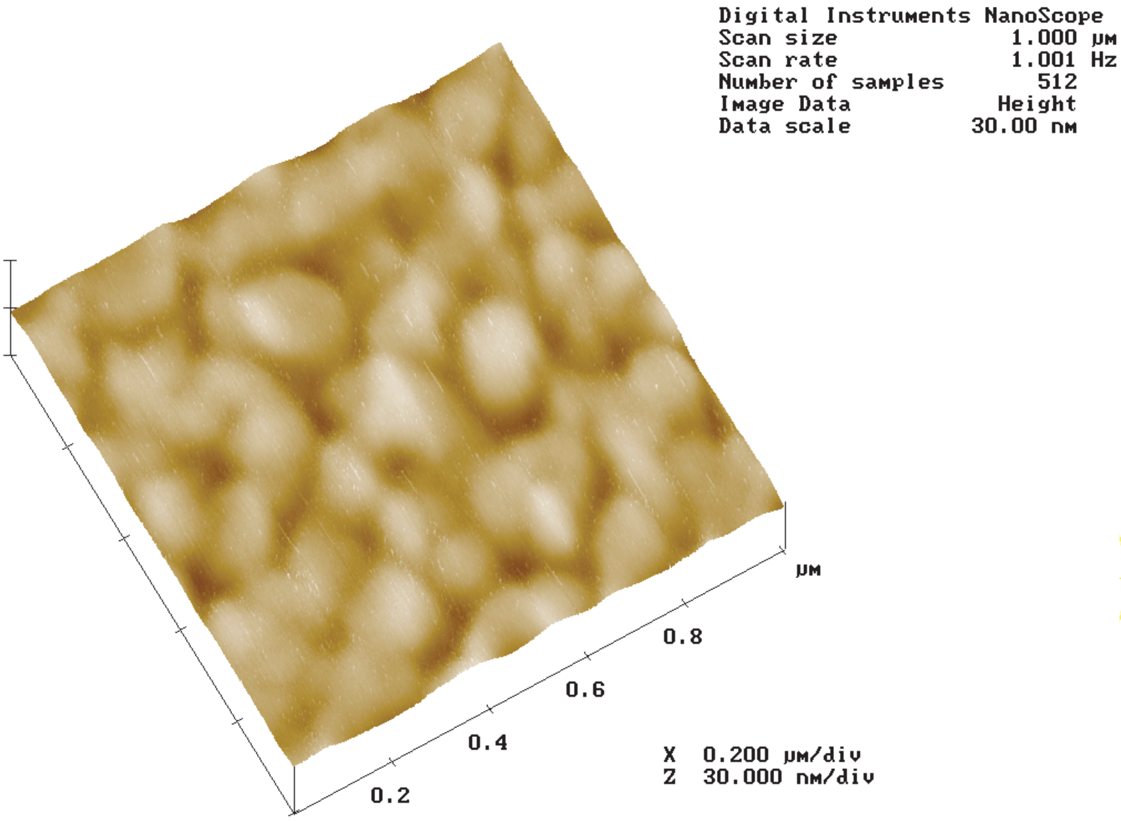

Figure 6.12: AFM image of the surface of LCMO single layer grown on $SrTiO_3$ single crystalline substrate (100). The $1\times1\mu$m scan shows a smooth surface and layer-by-layer growth with a roughness of about $R_a \approx$1 nm.

0.4 % when grown on an LCMO substrate as buffer layer. This means a different growth mechanism is expected. Indeed, YBCO behaves differently in this case compared to the growth of a single layer as shown in Fig. 6.13.

Figure 6.13 shows an AFM scan of a YBCO layer of 100 nm YBCO/50 nm LCMO bilayer. This image now shows a completely different surface topography in comparison to the single layers shown before. The surface consists of two different structures, there are island–like areas, that can be found with round shape and diameters of 1–2 μm, these islands are strictly interrupted by slab or stick–like heightings which are oriented only in two directions perpendicular to each other. These structures have a width of about 100 nm and a length of several micrometers. This result shows clearly that there is no layer–by–layer growth in these bilayers. At the moment there exists, however, no model which explains the observed structure in detail.

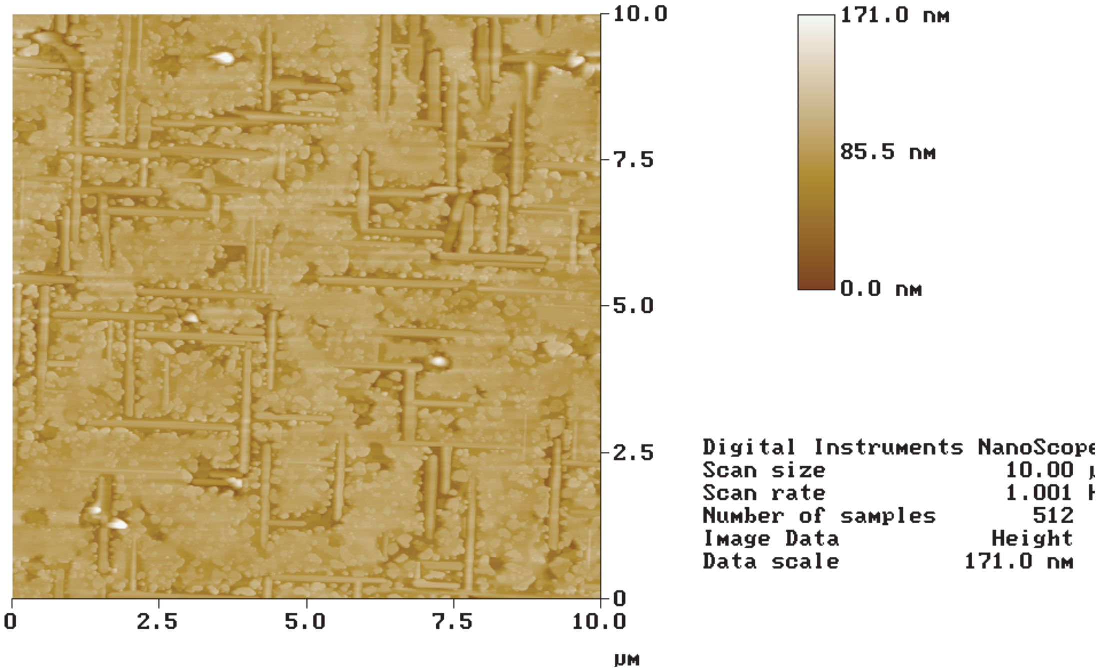

Figure 6.13: AFM image of 100 nm YBCO/50 nm LCMO bilayer grown on STO. The 10×10μm scan area shows that YBCO grows island–like interrupted by slab or stick–like heightings.

6.4 Summary

In this part the structural analysis of bilayers structures of manganites and cuprates have been investigated. Macroscopic (XRD) and microscopic (HR-TEM and AFM) analysis shows that LCMO/YBCO bilayers, heterostructures, and superlattices can grown epitaxially on each other. The oxygen content of the YBCO layer in bilayer more or less constant, with δ of about 0.2 AFM image shows for the YBCO layer in bilayer that different growth mechanism established compared to growth of single layer.

Chapter 7

Results

This chapter consists of three major sections. In the first section the experimental and theoretical determination of the spin diffusion length $\xi_{\rm fm}$ in LCMO/YBCO bilayers will be treated. Section 7.2 considers spin polarized quasiparticle injection effects in the normal and superconducting state of YBCO. In section 7.3 the critical currents in LCMO/YBCO bilayers are investigated with respect to magnetic flux pinning of the flux lines in the superconductor.

In the beginning a few characteristically properties of all the investigated samples will be discussed.

Samples geometry

A sketch of general geometry of the investigated samples is shown in Fig. 7.1. The samples consist of two epitaxial layers grown on single crystalline substrates. The structural quality of the bilayers is shown in Chapter 6 where x-ray diffraction measurements Fig. 6.2, and high resolution transmission electron microscopy (TEM) Fig. 6.10 is presented. As a result of this it is ruled out the structural imperfection dominate the physical properties of the bilayers.

Consequently we assume that possible perturbations created due to structural variations at the interface can be neglected.

In Fig. 7.2 shows the temperature dependence of the magnetization M(T) after zero–field cooling (ZFC) and field–cooling (FC) in an in–plane magnetic field $H_{\rm ext}$ = 10 Oe for a bilayer of $d_{\rm LCMO}$ = 50 nm and $d_{\rm YBCO}$= 100 nm. Both curves show the onset of positive magnetization signal at T $\approx$ 135 K, this temperature can be identified with the Curie temperature $T_{\rm Curie}$ of the ferromagnet. The ZFC curve give a clear diamagnetic signal starting at T $\approx$ 87 K, at this temperature the superconducting transition takes place. Below T $\approx$ 87 K both superconducting and ferromagnetic ordering is present in these bilayered systems.

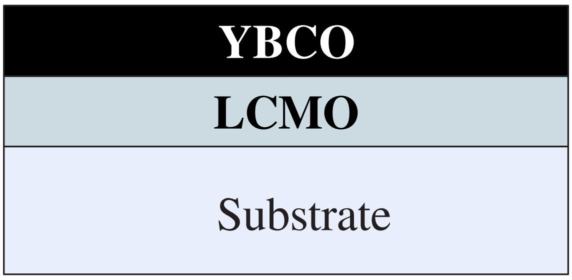

Figure 7.1: Sketch of the chosen sample geometry. $La_{2/3}Ca_{1/3}MnO_3$ (LCMO) and $YBa_2Cu_3O_{7-\delta}$ (YBCO) are grown by pulsed laser deposition onto $SrTiO_3$ (100) single crystalline substrates.

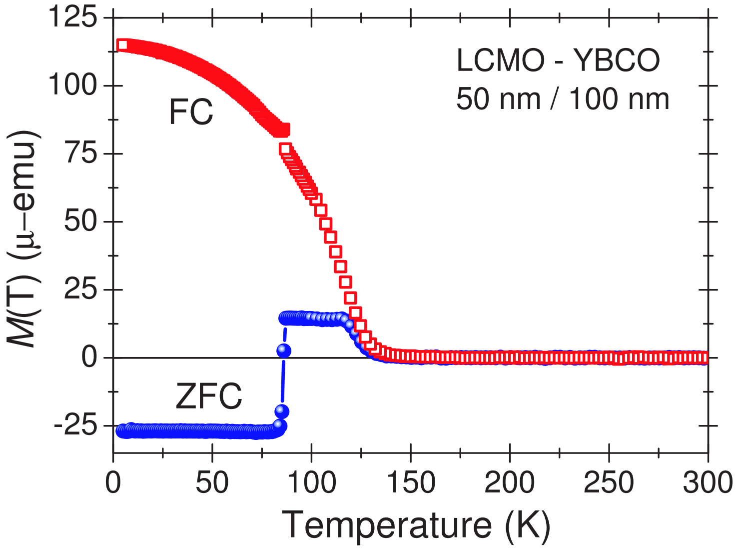

Figure 7.2: Temperature dependence of the magnetization M(T) after zero–field cooling and field–cooling in an in–plane magnetic field of H_{ext} = 10 Oe. Shown are the results for a bilayer of d_{LCMO} = 50 nm and d_{YBCO}= 100 nm.

7.1 Spin diffusion length determination

In this section experimental results and a theoretical estimation for the spin diffusion length ξ_{fm} of quasiparticles in heterostructures of cuprates and manganites will be given. This determination is able to describe properly the experimental results of bilayer structures and superlattices of CMR/HTSC.

The temperature-dependent magnetization of bilayers of LCMO and YBCO after zero-field cooling to T = 5 K has been measured to show if a coexistence of ferromagnetism and superconductivity at low temperatures occurs. In these experiments it is found that the superconducting transition temperature of the YBCO film decreases strongly for thicknesses of the superconductor of d_s = 30 nm and below. This is in contrast to YBCO single layers, where a thickness dependence of T_c occurs only for films with thicknesses

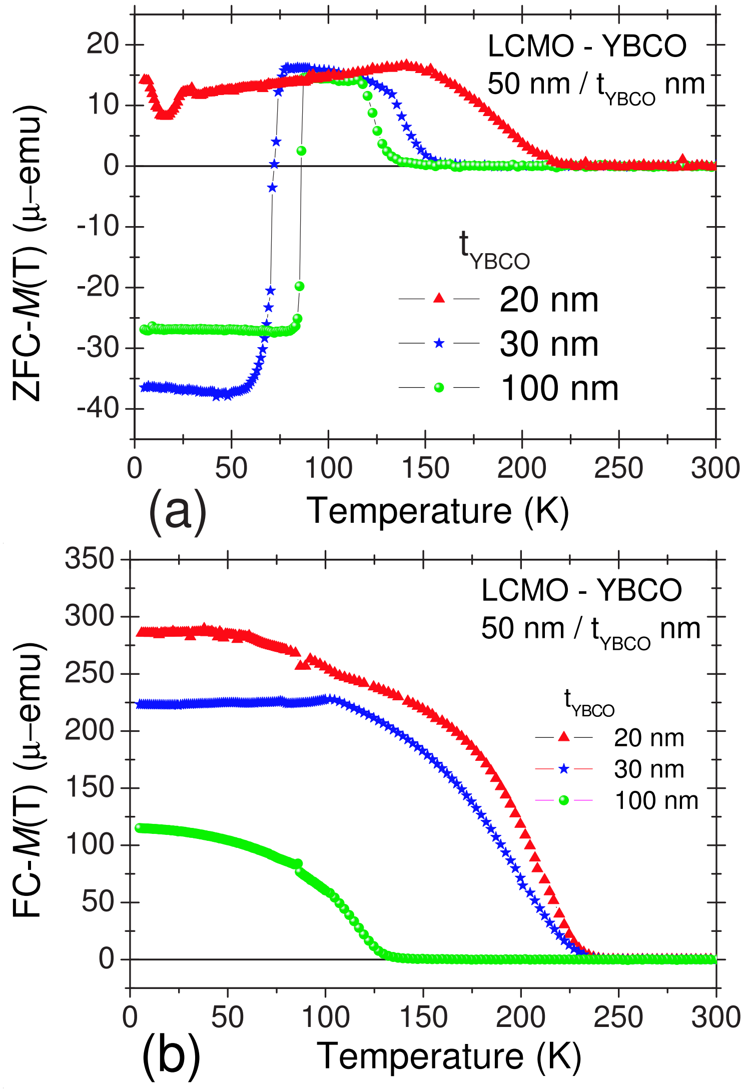

Figure 7.3: Temperature dependence of the magnetization M(T) after zero–field cooling (a) and field–cooling (b) in an in–plane magnetic field $H_{\rm ext}$ = 10 Oe. Shown are the results for bilayers of $d_{\rm LCMO}$ = 50 nm and $d_{\rm YBCO}$= 20 nm, 30 nm, and 100 nm. The 50 nm / 30 nm bilayer shows two ferromagnetic transitions in the zero–field–cooled measurement (a). The first at $T_{\rm Curie}$ = 229 K can not be seen in the figure the second one occurs at $T_{\rm Curie}$ =180 K. We attribute this behavior to a nonhomogeneous magnetic layer in that sample.

of well below 10 nm [150, 151].

7.1.1 Magnetization and Transport measurements

Figure 7.3a shows the magnetization M(T) as a function of temperature for three different bilayers. The measurements are performed after zero–field cooling to T = 5 K. Then, the magnetization is measured with increasing temperature in an in-plane external magnetic field of $H_{\rm ext}$ = 10 Oe. The three curves refer to three different bilayers with dimensions of

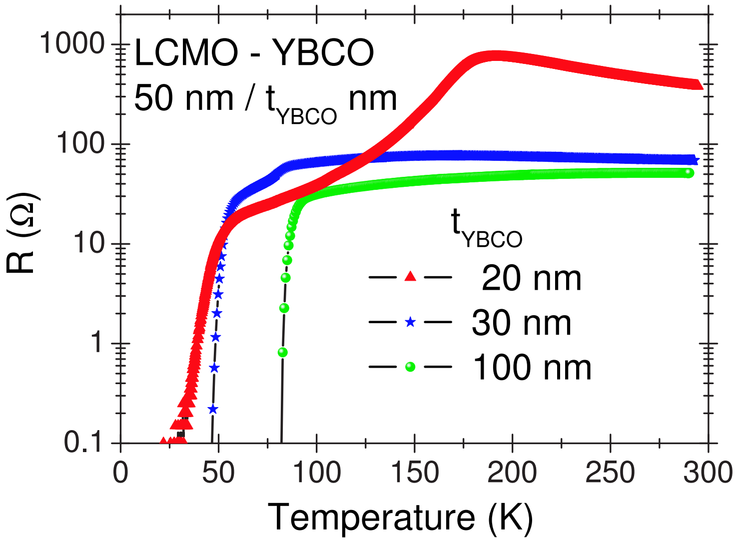

Figure 7.4: Temperature dependent in-plane resistance R(T) for the same samples as in Fig. 7.3a. The data are collected from standard four-probe measurements.

d_{LCMO} = 50 nm and d_{YBCO} = 20, 30, and 100 nm, respectively. In Fig. 7.3a starting at low temperatures, a negative magnetization is seen that refers to the diamagnetic signal of the dominant superconducting state. With increasing temperature the magnetization jumps to positive values. This temperature identifies the superconducting transition temperature T_{c}. Above the critical temperature T_{c}, which depends on the thickness of the YBCO layer, a positive magnetization is found that is caused by the ferromagnetic ordering in the LCMO layer. With increasing temperature the magnetization drops to zero. This temperature identifies the ferromagnetic transition temperature T_{Curie}.

To prove that the ferromagnetic ordering is also present below the superconducting transition, where the signal is governed by the diamagnetic response of the YBCO layer, also the field-cooled magnetization is measured. The results are given in Fig. 7.3b. It shows the magnetization M(T) as function of temperature for the three different bilayers. The field-cooled measurement M(T) is done in an in-plane external magnetic field of H_{ext} = 10 Oe. Here, two important features are found, first, ferromagnetism occurs in the whole temperature range; $T \leq T_{\mathrm{Curie}}$. Second, the ferromagnetic ordering shifts to lower temperatures with increasing thickness of the YBCO layer.

In addition to the magnetization data the electrical resistance R(T) has been measured for the bilayers as shown in Fig. 7.4. Three results are given for d_{LCMO} = 50 nm and d_{YBCO}= 20 nm, 30 nm, and 100 nm. In case of the thinnest bilayer a transition from a semiconductor–like behavior ($dR/dT < 0$) to a metallic–like ($dR/dT > 0$) around T = 180 K was found. This shows that the properties of the YBCO in the bilayer have to be strongly affected due to the presence of the LCMO layer. Otherwise the large difference in resistivity between YBCO [ρ_{YBCO}(T=300 K) $\approx$ 150 $\mu\Omega$cm] and LCMO [ρ_{LCMO}(T=300 K) $\approx$ 10 mΩcm] would lead to current flow only in the cuprate layer. But

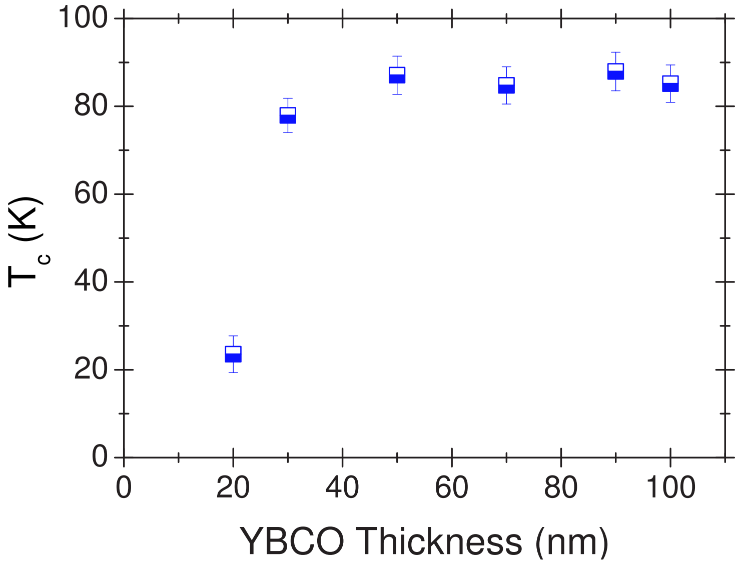

Figure 7.5: The superconducting transition temperature of bilayers on STO with varying thickness of the YBCO layer obtained from the diamagnetic on–set in the zero–field–cooling magnetization measurements.

this behavior can only be found in case of bilayers with thicknesses of the YBCO layer of d_{YBCO}= 30 nm and 100 nm, respectively. The different R(T) behavior of the 50 nm/20 nm bilayer is therefore related to a diffusion of spin–polarized quasiparticles from the LCMO layer into YBCO.

From the zero–field cooled magnetization curves M(T) the transition temperature T_{c} of the YBCO film is extracted. Here the diamagnetic signal is used to define T_{c}, the values are determined by the maximum of the first derivative of M(T). As a result a strong decrease of T_{c} is found for bilayers containing thin YBCO layers. In case of a 20 nm YBCO film we find T_{c}= 23 K, for the 30 nm film we find T_{c}= 76 K, whereas bilayers with thicker YBCO films show transition temperatures between T_{c} = 85 K and 90 K. A plot of the transition temperatures for different YBCO thicknesses is shown in Fig. 7.5.

Additionally, not only the transition temperature but also the critical current density [152–158] in the YBCO layer is affected by the magnetic layer. Detailed investigation about magnetic flux pinning inside the superconductor will be given in the next section.

Another interesting observation in the field–cooled magnetization M(T) in Fig. 7.3b is the increase of the ferromagnetic transition temperature with decreasing thickness of the YBCO layer. For a fixed CMR layer thickness of 50 nm, ferromagnetic transition temperatures T_{Curie} = 245 K, 240 K, and 117 K are found for YBCO thicknesses of 20, 30, and 100 nm, respectively. In Fig. 7.6 a plot of the ferromagnetic ordering temperature T_{Curie} of all of the bilayer structures as a function of the thickness of the YBCO layer is shown.

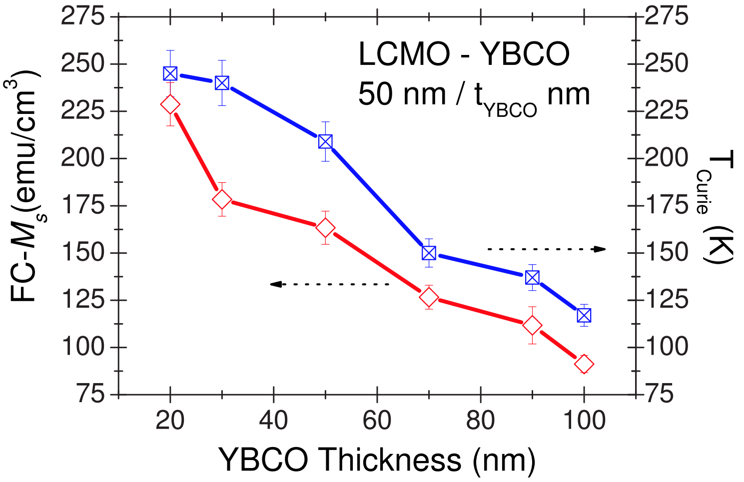

Figure 7.6: Ferromagnetic ordering temperature T_{Curie} and saturation magnetization M_s of bilayers with varying thickness of the YBCO layer. T_{Curie} is determined from the on–set of the ferromagnetic signal in Fig.7.3b. M_s is determined from the saturation signal $M(T)$ in Fig. 7.3b divided by the volume of the LCMO layer. T_{Curie} and M_{s} strongly decrease with increasing YBCO thickness. The error-par represents different series of samples results grown at different times.

The 1/3-Ca doped $\text{La}_{1-\text{x}}\text{Ca}_{\text{x}}\text{MnO}_3$ compound has a bulk value of $T_{\text{Curie-bulk}} \approx 275$ K, for thin films T_{Curie} = 245 K is measured [159]. The reduction of the ferromagnetic ordering temperature may be regarded as indication for a charge transfer from the ferromagnetic layer into the superconductor. However, evidence for this process can not be given from these experiments. Further information might be accessible by optical conductivity measurements. Concerning the coexistence of the two phenomena (ferromagnetism and superconductivity), the very low in–plane coherence length $\xi_{\text{ab}} \approx 1.6$ nm of the high-T_{c} materials probably rules out that such a coexistence can be found in more than 1 to 2 unit cells away from the interface.

7.1.2 Theoretical calculation of ξ_{fm}

In this sub–section a theoretical model is presented that is able to describe the observed reduction of the superconducting transition temperature in the investigated bilayer systems. The application of the model allows us finally to give an estimate for the spin diffusion length of spin polarized quasiparticles from the ferromagnet into the superconductor.

The decay length of the superconducting order parameter ξ_{prox} in the ferromagnetic layer (*proximity effect*) can be written as

$$\xi_{prox} = \frac{\hbar v_F}{\Delta J_{spin}} \tag{7.1}$$

where v_{F} is the Fermi velocity and ΔJ_{spin} the spin exchange splitting energy of the ferromagnetic layer.

So far, oscillations of the superconducting transition temperature T_{c} in the CMR / *d*-wave–HTSC superlattices have not been found experimentally [112, 113, 160, 161]. This can be understood from the following equation:

$$\xi_{sc} = \sqrt{\frac{\hbar D_{sc}}{k_B T_c}} \tag{7.2}$$

where ξ_{sc} is the coherence length; D_{sc} the electron diffusion coefficient in the superconductor; k_{B} is Boltzmann's constant and T_{c} the critical temperature. From equations (7.1) and (7.2) one can conclude that oscillations of the critical temperature T_{c} of the unconventional superlattices (CMR/*d*-wave SC) do not occur due to the large exchange energy $\Delta J_{\mathrm{spin}} \approx$ 3 eV [114] for the hole-doped rare–earth manganites in conjunction with the short coherence length $\xi_{\mathrm{ab}} \approx$ 1.6 nm, $\xi_{\mathrm{c}} \approx$ 0.3 nm for YBCO. Additionally, a very small spin diffusion length ξ_{fm} into the superconducting layer is expected. The nearly full spin polarization (spin↑ or spin↓) at the Fermi level of LCMO leads to the quenching not only of the *Andreev reflections* [79] but also of the *proximity effect*, since it prevents the Cooper-pairs to tunnel into the magnetic layer. This also leads to the absence of oscillations of T_{c} in these CMR/HTSC superlattices. Nevertheless, next section results will show a weak kind of oscillation on T_{c}, which just exists in case of SPQ injection with additional injection energy, more details will be given later.

The pair breaking in CMR/HTSC due to the injection of quasiparticles (QPI) into the superconducting layer has been taken into account by different groups [116, 156]. This phenomenon has been very early investigated by Parker [117] and can be written as:

$$\frac{\Delta(n_{qp})}{\Delta(0)} \approx 1 - \frac{2n_{qp}}{4N(0)\Delta(0)} \tag{7.3}$$

where $\Delta(n_{\mathrm{qp}})$ is the energy required to suppress the order parameter of the superconductor due to the density of spin polarized quasiparticles n_{qp}. N(0) and Δ(0) give the density of states and the order parameter at T = 0 K, respectively. n_{qp} is generated by self-injection along the *c*-axis across the highly transparent interface and is governed by the high exchange spin splitting energy $\Delta J_{\mathrm{spin}} \approx$ 3 eV of the magnetic layer, see equation (7.1). The QPI is a temperature dependent function and can be derived in the following form [158, 166]:

$$n_{qp}(T) \approx 4N(0)\Delta(0)\sqrt{\frac{\pi}{2}\frac{\Delta(T)k_B T}{\Delta^2(0)}}\; e^{\frac{-\Delta(T)}{k_B T}} \tag{7.4}$$

The spin diffusion length ξ_{fm} can now be determined after Ref. [116] analogous to a classical FM/SC structure as:

$$\xi_{fm} \approx \sqrt{\ell_o v_F \tau_s} \tag{7.5}$$

Here ℓ_o(T = 0 K) $\approx$ 20 nm is the mean free path in YBCO [156], the spin diffusion relaxation time τ_s is given by:

$$\tau_s \approx 3.7 \frac{\hbar k_B T_c}{\Delta J_{spin} \Delta(T)} \tag{7.6}$$

where:

$$\Delta(T) \sim \Delta(0) \sqrt{1 - (\frac{T}{T_c})} \tag{7.7}$$

with $\Delta(0)$ $\approx$ 20 meV for YBCO [156]. From equation (7.3), we end up with a relation where the temperature dependence and the length scale of the spin diffusion length ξ_{fm} is included.

First, the spin density in the superconductor has to be to considered. It is assumed that spins in high–temperature superconductors can be described as unitary scatterers. From Zn doping in YBCO it is known that a critical doping in the range of 2-10 % strongly reduces T_{c} [162–164]. This critical density of spins is achieved at a distance of d = α ξ_{fm} , with α $\approx$ 3. This d is now identified with the YBCO film thickness. This enables us to model the experimental data by:

$$d = \alpha \xi_{fm} \cong 3.7 \frac{\alpha m^* \hbar v_F^2}{\Delta(0) \Delta J_{spin} n_{qp}(0) e^2} \frac{\sqrt{T/n_{qp}(T)}}{\sqrt[4]{1 - (T/T_c)}} \tag{7.8}$$

m^* and e are the electron effective mass and charge.

Introducing now n_{qp}(T) from equation (7.4) we are able to fit our experimental data using the quasiparticle density as the only free parameter. This parameter n_{qp}(T) describes the decrease of the energy gap Δ(n_{qp}) [117, 165]. In our case we find the best fitting for n_{qp}(T)$\approx$ 0.36, 0.35, and 0.13 for T/T_{c} = 0.01, 0.3, and 0.9, respectively, which agrees with other theoretical calculations of n_{qp}(T)$\approx$ 0.32, 0.31, and 0.09 at the same temperature ratio for *d*-wave superconductors [166, 167]. Figure 7.7 shows the experimentally determined transition temperatures normalized to the $T_{\mathrm{c-bulk}}$=91 K for different film thicknesses on two different substrates $SrTiO_3$ (STO) and $LaSrGaO_4$ (LSGO) and the fit to the theoretical model. Note, the results of the bilayers grown on LSGO was at different times (1.5 years in between) comparing to the bilayers grown on STO. Which prove the reproducibility of the effect.

The description fits to the experimental results and suggests that the recovery of the transition temperature T_{c} of the YBCO top layer takes place at about 30 nm which leads to a spin diffusion length of $\xi_{fm} = d/\alpha$ $\approx$10 nm. This finding is in good agrement with

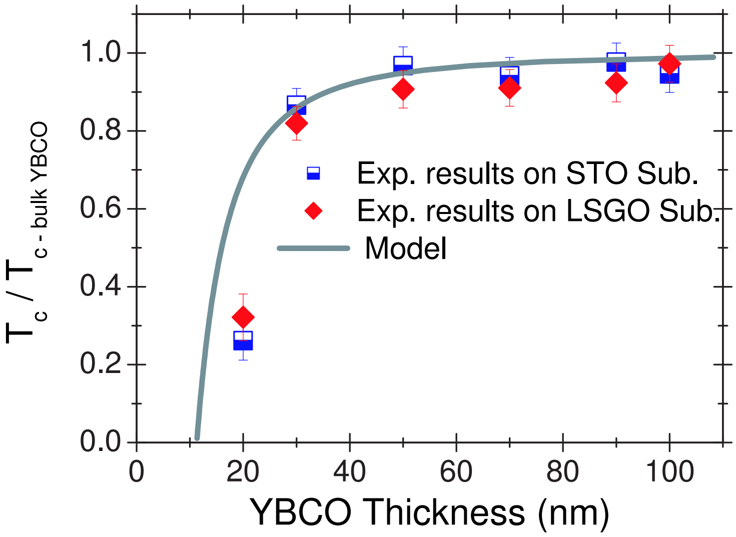

Figure 7.7: The normalized superconducting transition temperature of bilayers with varying thickness of the YBCO layer on STO and LSGO substrates obtained from the diamagnetic on–set in the zero–field–cooling magnetization measurement (squares). The solid line represents the model according to equation (7.8). A good description of the experimental data is achieved.

results that have been estimated [168, 169] from optically investigated LCMO/YBCO superlattices. These results provide an evidence that the free carrier response is strongly suppressed in these superlattices as compared to pure YBCO and LCMO films, and they estimate that a critical thickness for the YBCO is in the range of 20 nm. Note, that in case of superlattices the spin–polarized quasiparticles penetrate from both sides into to the superconducting film. The accordance between the results shown in this section and other groups using different experimental techniques gives rise to a spin diffusion length ξ_{fm} from LCMO into YBCO in the order of 10 nm at low temperatures.

7.1.3 Summary

In this part the effects of the diffusion of spin–polarized quasiparticles in bilayer structures of manganites and cuprates have been investigated experimentally and theoretically. Transport and magnetization measurements show the coexistence of ferromagnetism and superconductivity at low temperatures in these structures. The transition temperature of the superconducting film drastically decreases with thinner $\mathrm{YBa_2Cu_3O_{7-\delta}}$ films. The development of a simple model allows the explanation of the experimental data and the determination of the spin diffusion length of spin–polarized quasiparticles from $\mathrm{La_{2/3}Ca_{1/3}MnO_3}$ into $\mathrm{YBa_2Cu_3O_{7-\delta}}$ to be in the range of $\xi_{\mathrm{fm}} \approx 10$ nm.

7.2 Spin–polarized quasiparticle injection effects in YBCO thin films

After studying the self diffusion of spin–polarized quasiparticles (SPQ) in the last section, now the HM–CMR layer is used as source for SPQ injection with external energy. The effect of SPQ injection into the *ab*-plane and along the *c*-axis of YBCO will be discussed in two parts. The results show two interesting features: (i) a drop in the *ab*-plane resistance $R_{\rm ab}$(T) in the normal state of YBCO around a characteristic temperature $T_{\rm d}$ in case of the injection along the *c*-axis that might be related to the opening of a pseudogap. This result will be discussed in the framework of the spin–charge separation model as suggested by P.W. Anderson [30]. And (ii) a spin dependent shift of $T_{\rm c}$ for spin-polarized quasiparticle injection (SPQI).

7.2.1 Samples geometry

For the purpose of spin injection, two special designs have been used for the SPQI along the *c*-axis and into the ab-plane of YBCO thin films in heterostructure junctions. All of the samples consist of three epitaxial layers of LCMO, YBCO, and LCMO, in the following the configuration of the two setups is presented in detail:

(i)*c-axis injection sample design:* The geometry is given in Fig. 7.8. Using conventional lithography we fabricated 3 contact strips for current injection on both LCMO layers with widths of 200μm (contacts numbers 1,4, and 7), and four contact strips for resistance measurement on the YBCO layer (contacts numbers 2,3,5, and 6). As contact materials evaporated chromium/gold (Cr/Au) 15 nm/100 nm are used.

(ii)*ab-plane injection sample design:* The geometry is given in Fig. 7.9. Injection and measurement contacts are made on both, the LCMO top layers, and the free area of the YBCO layer, contact numbers 1 and 6 have been prepared on the LCMO layer. Four contacts are placed on the YBCO layer for the resistivity measurement (2,3,4, and 5). As contact materials evaporated chromium/gold (Cr/Au) 15 nm/100 nm are used.

7.2.2 SPQ injection effects in normal state of YBCO

For spin–polarized quasiparticle injection along the *c*-axis ($I_{\rm inj-c}$) the setup of Fig. 7.8 is used. In addition to the injection current, a current is applied directly through the YBCO layer with $I_{\rm YBCO}$ = 0.1 mA, passing through the contacts 2,6 and the voltage is picked–up through 3 and 5.

Figure 7.10a shows the resistance $R_{\rm ab}$(T) as a function of temperature for different spin–polarized quasiparticle (SPQ) injection currents along the *c*-axis of YBCO ($I_{\rm inj-c}$ = 0.0, 0.3, 0.4, 0.5, 0.75 mA). Starting at room temperature in Fig. 7.10, we see that with

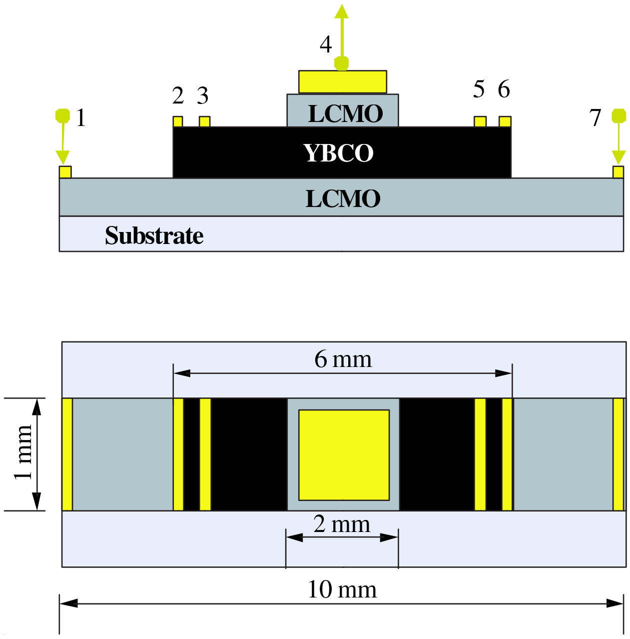

Figure 7.8: Sketch of the sample geometry chosen for the injection of spin–polarized quasiparticles along the c–axis of YBCO. The 50 nm $La_{2/3}Ca_{1/3}MnO_3$ (LCMO), 100 nm $YBa_2Cu_3O_{7-\delta}$ (YBCO), and 50 nm $La_{2/3}Ca_{1/3}MnO_3$ (LCMO) are grown by pulsed laser deposition onto $SrTiO_3$ (100) single–crystalline substrates. The width of the structure is 1 mm.

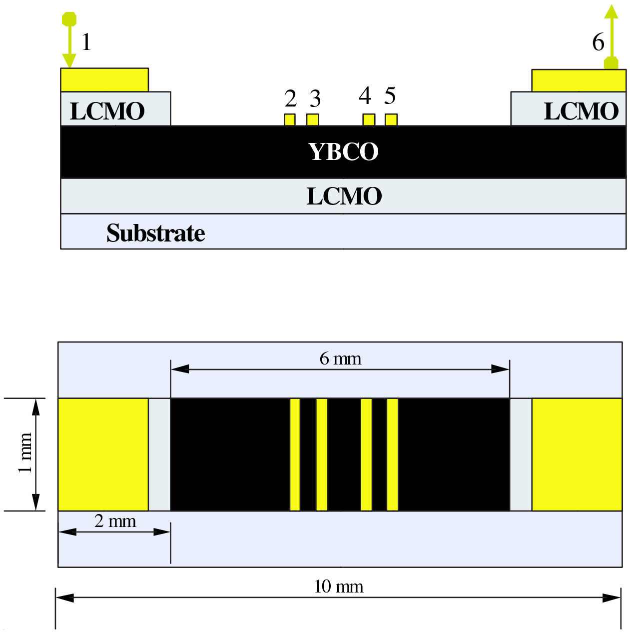

Figure 7.9: Sketch of the sample geometry chosen for the injection of spin–polarized quasiparticles along the *ab*-plane of YBCO. The films have the same thickness and the width is again 1 mm.

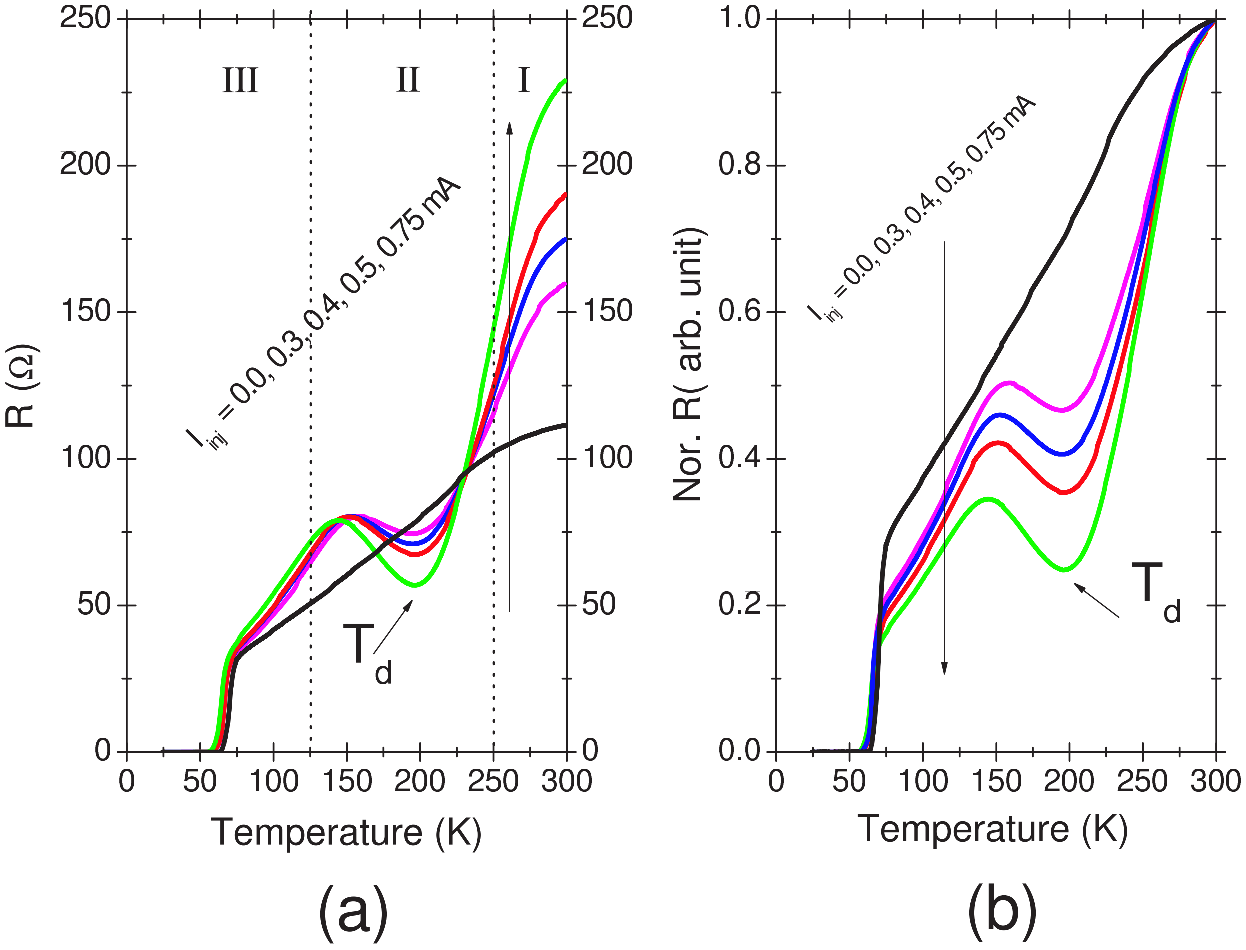

Figure 7.10: Temperature–dependent in-plane resistance R(T) for the YBCO layer in setup Fig. 7.8, for different SPQ currents values $I_{\mathrm{inj-c}}$ = 0.0–0.75 mA (a). The data are collected from standard four-probe measurements. Notice, that an enhancement of the SPQ current causes an increase in the resistance at room temperature, but a drop in the resistance is found around the temperature T_{d} of the order of 25%. Additionally, a shift from 63 K to 54 K is found in the transition temperature T_{c}. (b) Normalization of the temperature–dependent in–plane resistance to the room–temperature resistance.

enhanced SPQ current a pronounced enhancement in the resistance at room temperature (R_{room}) is found (region I). This enhancement of R_{room} from 112 $\Omega \leq R_{\mathrm{room}} \leq$ 225 Ω for 0.0 mA $\leq I_{\mathrm{inj-c}} \leq$ 0.75 mA, respectively, reflects on the one hand the scattering process of the quasiparticles in the YBCO layer at room temperature. On the other hand, an additional voltage drop due to the current injection cannot be avoid completely. But this effect is temperature independent therefore a rescaled representation normalized to the room temperature resistance is given in Fig. 7.10b. Applying the SPQ current, a pronounced drop of the resistance can be seen in region (II). This drop of the resistance from 74 Ω to 55 Ω for $I_{\mathrm{inj-c}}$ = 0.0 mA and $I_{\mathrm{inj-c}}$ = 0.75 mA, respectively, gives rise to a 25 % reduction in resistance around T_{d}, where T_{d} denotes the temperature at which the minimum in the resistance in the normal state is found (region (II)in Fig. 7.10a). On the other hand, T_{d} is shifted to higher temperatures, 195 K $\leq T_{\mathrm{d}} \leq$ 207 K for an enhanced SPQ current density (see Fig. 7.10b). Region (III) in Fig. 7.10a, shows the effect of the SPQ on the transition temperature T_{c}. Also, a pronounced shift to lower temperatures is found; 63.5 K $\leq T_{\mathrm{c}} \leq$ 54 K; for an enhancement of the SPQ current density 0.0 mA $\leq I_{\mathrm{inj-c}} \leq$ 0.75 mA.

Growing YBCO as a cap layer onto LCMO leads to a decrease of the transition temperature T_{c} compared to YBCO single layers. The observed decrease of T_{c} is considered to have two reasons. *First*, the magnetization of the ferromagnet leads to pair–breaking in the superconductor [170]. *Second*, the self diffusion of spin-polarized quasiparticle into YBCO layer as shown in section 7.1.

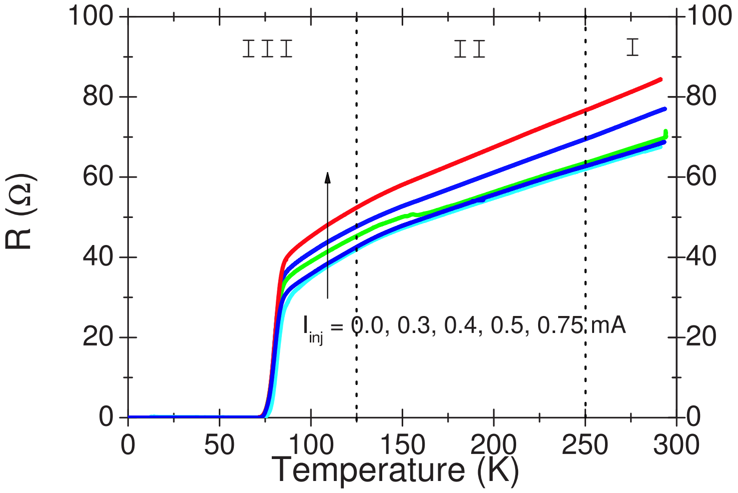

Figure 7.11: Temperature–dependent in-plane R(T) for the YBCO layer for the sample geometry given in Fig. 7.9, the *ab*-plane injection. The data are collected from standard four-probe measurements. We also find a shift in both T_{c} and R_{room} due to the quasiparticle injection, but no additional minimum in the R(T) curves occurs between T = 150 K and 200 K.

Figure 7.11 shows the experimental results of the SPQ injection into the *ab*-plane of the YBCO film using the setup shown in Fig. 7.9. Note, that the SPQ current is injected through point 1 and 6, and the YBCO current I_{YBCO} = 0.1 mA through 2 and 5. The YBCO voltage is picked–up through 3 and 4. This configuration allows us to detect the effect of the SPQ into the *ab*-plane of the YBCO layer. R_{room} changes between 70 $\Omega \leq R_{\mathrm{room}} \leq$ 85 Ω for $I_{\mathrm{inj-ab}}$ = 0.0 mA to 0.75 mA as seen in region (I) in Fig. 7.11. In region (II) no effect can be found which is similar to the *c*-axis injection experiment (Fig. 7.10). This is expected due to the fact the SPQ has finite length ξ_{fm} of spin conservation [170]. In region (III) of Fig. 7.11 the effect of the SPQ injection is pronounced not only in the reduction of the transition temperature T_{c} from 74.5 K to 70 K, but also in the shape of R(T) in the normal state. Note, that the transition temperature without current injection is higher than in Fig. 7.10, because the YBCO film has only one interface to a LCMO layer, whereas the sample for c–axis injection has two.

To clarify whether the observed effect is related to the SPQ injection into YBCO, different junctions have been designed and grown keeping the thickness of the heterostructures constant, only changing the source materials for the quasiparticles:

First, $SrRuO_3$ (SRO) has been selected to replace the LCMO layer in the heterostructures. $SrRuO_3$ is a ferromagnet with a lower Curie temperature T_{Curie} = 165 K compared to 1/3–Ca doped LCMO (T_{Curie} = 275 K), and a lower polarization (10-30 %) for the conduction electrons [171]. *Second*, the paramagnetic metal $LaNiO_3$ (LNO) compound is replacing the LCMO layer in the heterostructures.

Figure 7.12 shows the experimental results of the SRO/YBCO/SRO (a) and LNO/YBCO/LNO (b) heterostructure with thicknesses of 50 nm/100 nm/50 nm, respectively. The results show, that replacing LCMO by SRO, or LNO, there is *no* effect around the characteristic temperature T_{d}. The only matching between the junctions is a higher resistance at room temperature and a shift of the transition temperature T_{c} to lower values. It is very important to note that, the injection of *non–polarized* quasiparticles from the LNO layer enhances the scattering process in YBCO in the whole temperature range to the transition temperature T_{c}. Concerning the quasiparticle scattering this result shows similar results compared to the other results of the LCMO/YBCO/LCMO heterostructure in Fig. 7.10. The difference between both junctions is the drop of the resistance around the temperature T_{d}. This drop only appears in case of the injection of *spin–polarized* quasiparticles. Finally, a heterostructure is prepared that consists of a thin $SrTiO_3$ layer separating LCMO and YBCO. Also the introduction of such an electronic decoupling layer that blocks the transport of SPQ leads to an absence of the resistance drop.

The relevant experimental results may be summarized as follows: 1) Increasing resistance of the YBCO layer R_{room} with increasing injection current of SPQ or normal QP along the c–axis or into the *ab*-plane of the YBCO layer . 2) Increase of the resistance drop around T_{d} and shift to higher values in case of SPQ injection along the c–axis of the YBCO layer. 3) Absence of the drop in the case of SPQ injection into the *ab*-plane of the

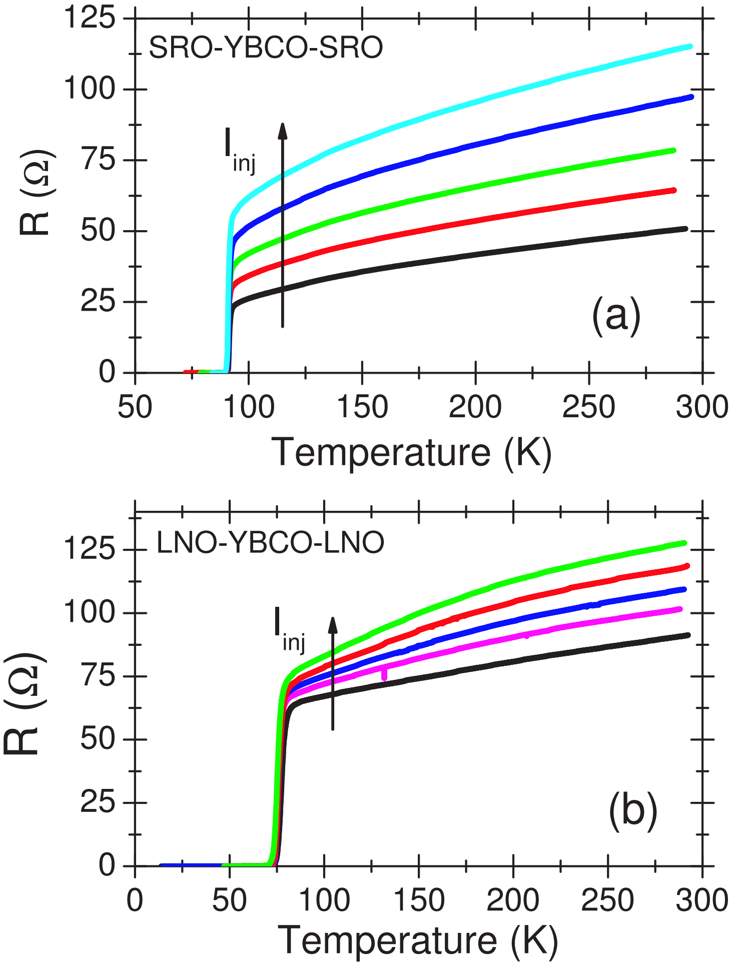

Figure 7.12: Temperature dependent in-plane resistance R(T) for the YBCO layer for the sample geometry given in Fig. 7.8, replacing LCMO layer by SRO (a) or LNO (b). The data are collected from standard four-probe measurements. Notice, that with enhanced injection currents an increase in the resistance from room temperature to the transition temperature is found, in addition to that no effect for the *non–polarized* QP or *lower* polarized QP around the pseudogap temperature can be seen.

YBCO layer. 4)QP spin dependent shift of T_c of the YBCO layer to lower values with increasing I_inj in all the samples.

7.2.2.1 Spin dependent shift of T_c of YBCO

The shift of T_c in Fig. 7.13 with increasing I_inj is explained by the following model. Pair–breaking due to quasiparticle injection (*or proximity effect*) was suggested by Parker [117] (7.3). On the other hand, the proximity effect (i.e. the penetration of Cooper-pairs into the neighboring layer) can be ignored for the reduction of T_c in our heterostructures. The large spin exchange energy J_spin of the magnetic layer (J_spin of LCMO $\simeq$ 3 eV) [114] prevents Cooper-pairs from tunnelling into the LCMO film. Arguments related to the T_c

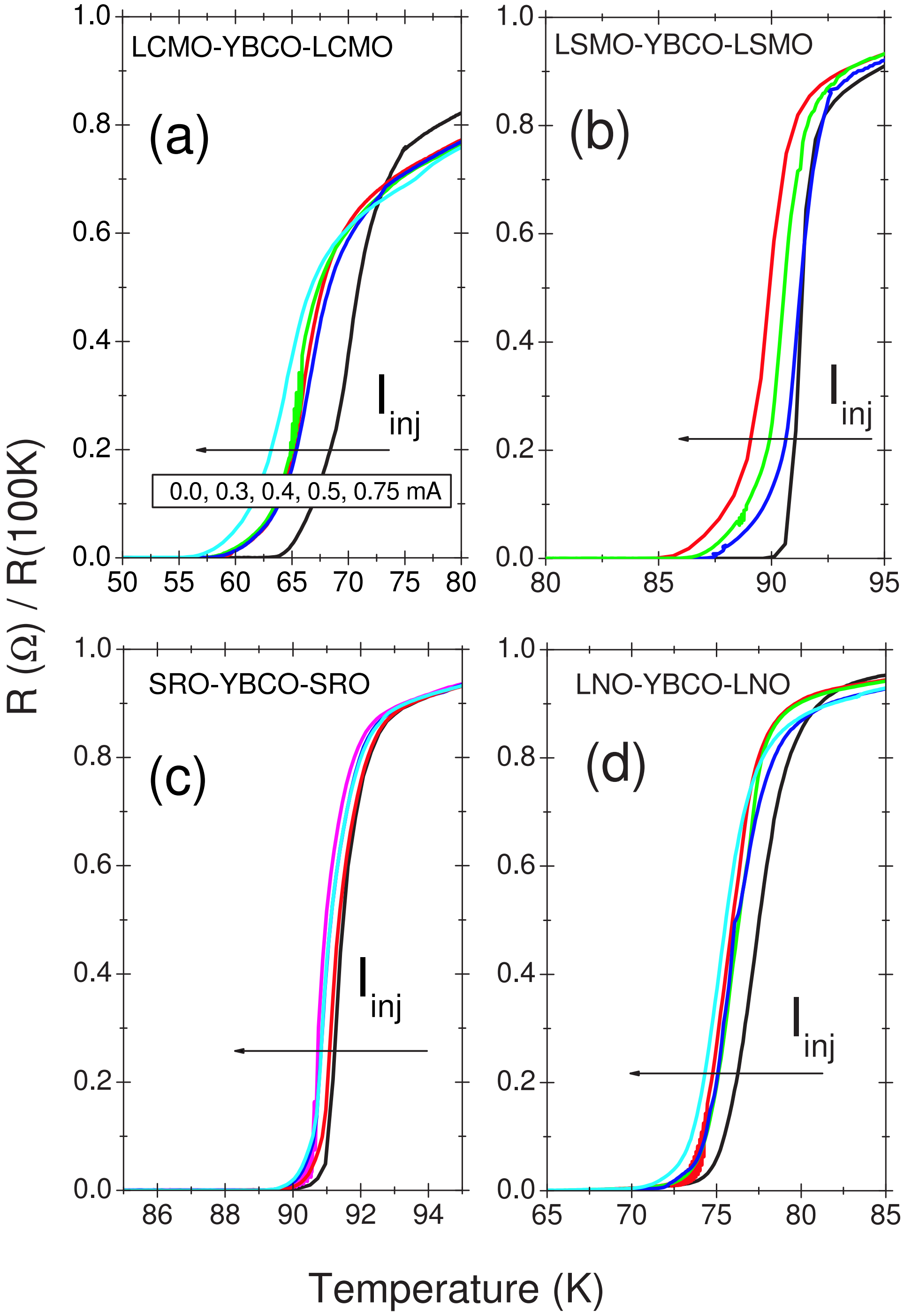

Figure 7.13: Normalization of the temperature dependent in-plane resistance R(T)/R(100 K) for the YBCO layer for the sample geometry given in Fig. 7.8. With an enhancement of $I_{\mathrm{c-inj}}$ different effects on T_{c} are found. The reduction of T_{c} is more pronounced in case of SPQP injection (a) and (b) and less pronounced for the *lower*-polarized QP or *non*-polarized QP (c) and (d), respectively.

reduction with the pair–breaking model have been elaborated in a previous section [170].

Especially, the two heterostructures that contain manganite layers exhibit a distinct difference in T_c: For the LCMO/YBCO/LCMO structure, Fig. 7.13a, a transition temperature of T_c = 63.5 K is found, whereas the LSMO/YBCO/LSMO samples, Fig. 7.13b, show $T_c \approx 91$ K. Three reasons can be found to explain this finding.

First, the higher coercive field of a LCMO single layer ($H_c \approx 180$ Oe) compared to LSMO ($H_c \approx 130$ Oe) causes a strong suppression of the Cooper–pair density due to magnetic–field induced pair–breaking.

Second, LCMO and LSMO show a substantial difference in the magnetic domain pattern if the materials are part of a heterostructure with YBCO. This strongly affects the distribution of the magnetic stray fields and, thus, the interaction with the YBCO film. The role of the magnetic domain patterns will be addressed in more detail in the next section.

Third, the difference of the chemical potential μ at the interface between LCMO and YBCO, and LSMO and YBCO, respectively, is not equivalent. This may lead to charge redistribution of the YBCO film near the interface.

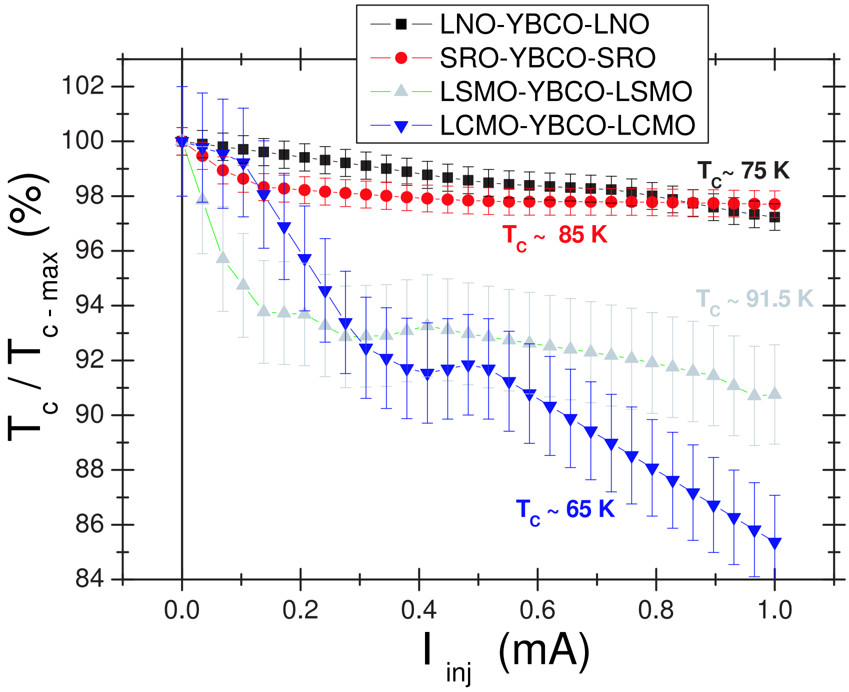

Figure 7.14: Transition temperature $T_c/T_{c-\max}$ versus $I_{c-\mathrm{inj}}$; where $T_{c-\max}$ is the superconducting transition temperature without injection current $I_{c-\mathrm{inj}}$ = 0.0 mA for heterostructures with the geometry given in Fig. 7.8. The error–bars refer to the onset and the offset of the transition, the symbols show the transition midpoint.

Figure 7.14 shows a systematic investigation of the shift of T_c due to QP injection along the *c*-axis of YBCO layer in the setup of Fig. 7.8. The heterostructures show different superconducting transition temperatures T_c, related to the type of contact layers. Here the normalized values $T_c/T_{c-\max}$ are shown, where $T_{c-\max}$ is the transition temperature without QP injection.

Figure 7.14 shows four different curves, two of them belong to *non*–polarized QP as a source for QP injection such as SRO/YBCO/SRO and LNO/YBCO/LNO heterostructures. The other two curves belong to full *spin*–polarized QP as a source for QP injection such as LSMO/YBCO/LSMO and LCMO/YBCO/LCMO heterostructures. A first look on the result yields a clear difference in the normalized $T_{\rm c}/T_{\rm c-max}$ values of *non*–polarized QP injection effects and full *spin*–polarized QP injection effects. In case of a QPI current density of $I_{\rm c-inj}$ = 1 mA from LNO or SRO as source materials, respectively, a drop of $T_{\rm c}$ of about 2% is found. On the other hand, the same QPI current density of $I_{\rm c-inj}$ = 1 mA injected from full *spin*–polarized conduction electron materials as a source shows a drop of 9% in case of LSMO and of 14% in case of LCMO. The only difference is the polarization of the QPI. This result clearly shows that the current injection from a spin–polarized material causes a much stronger decrease of $T_{\rm c}$ of YBCO than a non–polarized current injection. **This result is a direct evidence for spin injection into high–temperature superconductors.**

7.2.2.2 The role of $T_{\rm d}$ and normal state of YBCO

After the influence of spin–polarized quasiparticle injection on the superconducting transition temperature, now the normal state properties and current induced drop in resistivity are discussed in the following.

Two particular effects have been found in Fig. 7.10. The normal state resistivity shows an injection induced minimum around a characteristic temperature $T_{\rm d}$ and this $T_{\rm d}$ shifts to higher temperatures if the injection current is enhanced.

In Fig. 7.15 the phase transition line between the superconducting and the normal state of $\rm YBa_2Cu_3O_{7-\delta}$ is depicted in a doping level/temperature diagram. The superconducting transition temperatures $T_{\rm c}$ extracted from the injection experiment in Fig. 7.10b are now placed on this transition line. Additionally the corresponding $T_{\rm d}$ values are plot into the same diagram, under the assumption that a current injection leads to a shift of an effective doping level. It can be seen from Fig. 7.15 that the behavior of $T_{\rm d}$ leads very similar to the shape of the pseudogap temperature $T^*(\delta)$ in the generic phase diagram of hole doped HTSC. Due to that analogy the relation between T^* and $T_{\rm d}$ is discussed in the following.

For $T_{\rm c} \leq T \leq T^*$, the non-Fermi liquid (NFL) region, it is generally accepted, that in high–temperature superconducting materials unconventional normal–state properties are found. This leads to the model of spin–charge separation proposed by Anderson [30] and supported by Nagaosa and Lee [31, 32]. It is assumed that spins are bound together to form spin–singlets and the energy required to split them apart leads to the formation of a spin–gap [32]. Experimental results suggest that T^* is related to the occurrence of a spin–gap in the high-$T_{\rm c}$ materials [33–35].

On the other hand, it is proposed that superconductors with a low carrier density are characterized by a relatively small phase stiffness and thus, the poor screening implies a significant role of phase–fluctuations [36–45]. The phase–fluctuation scenario explains quite natural the strongly enhanced Nernst signal [21] above the critical transition temperature T_c in the underdoped HTSC materials. It was proposed by Emery and Kivelson [36] that the proximity to the Mott–insulating phase implies a strongly reduced phase stiffness V_o; where $V_\mathrm{o} \sim \rho_\mathrm{s}(0)/m^*$; with $\rho_\mathrm{s}(0)$ being the superfluid density and m^* the effective mass. The phase stiffness in this model is much smaller compared to the usual BCS case. This causes the phase ordering temperature $T^\mathrm{phase} \sim V_\mathrm{o}$ to be much lower than the mean–field pair–binding temperature T_c. Several authors interpret their experimental results suggesting that the pseudogap has a superconducting nature; i.e. Cooper-pairs are formed at T^* without phase coherence [21–29].

In fact the experimental results address the theoretical models aimed to describe the normal state properties of HTSC such as:

a) Phase fluctuations and SPQ injection into HTSC: The SPQ injection would enhance phase fluctuations due to two reasons: *first*: It is known that $T_c^{-1} \propto \tau_{pf}$ where τ_pf is the time scale of Cooper–pair phase fluctuations which might be present below T^* ($\tau_\mathrm{pf} \approx$ ps) [172]. On the other hand, a typical scattering time τ_s of the SPQ is in the fs range and related to the spin exchange energy $J_\mathrm{spin}^{-1} \propto \tau_s$ of the SPQ. Due to the short time scale of the SPQ scattering compared to Cooper–pair phase fluctuations the SPQ injection acts as perturbation of the system and thus enhances phase fluctuations. *Second*: If the superconductivity is driven by antiferromagnetic (AFM) correlations [173] and/or precursors of Cooper-pairs around T^* [36–45], SPQ injection would also effect these AFM correlations in terms of spin frustration and reorientation. This can lead to an enhancement of Cooper–pair phase fluctuations by SPQ injection. The result in Fig. 7.10 shows no tendency for such an argument due to the fact that T_d is shifted to higher values with enhanced density of the SPQ. On the other hand, we could not explain the up–turn of the resistance of the part below T_d. Therefore, the phase fluctuations model seems not to be supported by our experimental results.

b) Spin–charge separation and SPQ injection into HTSC: The SPQ injection enhances the polarization of the quasiparticles in the $\mathrm{CuO_2}$–plane. The pseudogap phenomenology is well explained by a cartoon picture which emerges from the RVB (resonating valence bond) theory of Anderson [30]. The spins are paired into singlets. However, the pairs are not static but are fluctuating (quantum spin liquid). The singlet formation explains the appearance of a spin–gap and the reduction of spin–entropy. The carriers are holes that appear as vacancies in the background of singlet pairs and can carry a current without energy gap [32]. As proposed by Si [49] according to the spin–charge separation model, the total resistivity in the normal state of the HTSC material could be written as $\rho_\mathrm{total} \approx \rho_\mathrm{spin} + \rho_\mathrm{charge}$ where ρ_spin is the spin resistivity and ρ_charge is the charge resistivity. Experimentally, the charge part is measured. It is assumed that, the SPQ injection along

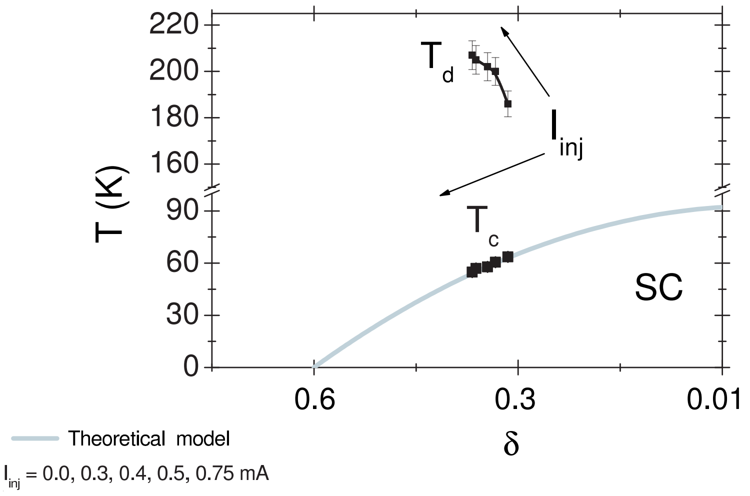

Figure 7.15: The gray line depicts the phase transition line between the superconducting and the normal conducting state in a doping level/temperature diagram for $YBa_2Cu_3O_{7-\delta}$. The measured T_c and the drop temperature T_d values as function of the injection current along *c*-axis I_{inj-c} are put in the same diagram.

c–axis of the YBCO layer interrupts the ρ_{spin} part by filling the spin–gap and/or open additional conduction channels in the CuO_2–plane. Hence, this leads to a reduction of the spin resistivity ρ_{spin} and this reduction appears in the charge part. This fits qualitatively to the drop of the resistance around T_d in Fig. 7.10.

Due to the effect of SPQ injection along the c–axis of the YBCO layer, an electron is removed from the CuO_2–plane and replaced by a SPQ. The intermediate state is an electron which carries spin 1/2 and therefore it is necessary to break a singlet pair and pay the spin–gap energy. This spin–gap energy, causes the up–turn in the measured resistance R(T). In addition, the SPQ has two characteristic properties, the life time (τ), and the spin diffusion length ξ_{fm}. After the SPQ has lost its polarization for length scales $> \xi_{fm}$, it behaves like a normal quasiparticle but still keeping the magnetic background in memory. In our opinion, both samples for the c–axis and the *ab*-plane injection into the underdoped YBCO support the spin–charge separation model.

7.2.3 Summary

In this part the investigation experimentally of the effects of spin–polarized quasiparticle (SPQ) injection in heterostructures of manganites and cuprates have been described. The transition temperature of the superconducting film decreases with an enhancement of the spin–polarized quasiparticles injection density. The SPQ injection along the *c*-axis of the YBCO layer shows a pronounced reduction in the *ab*-plane resistance of the YBCO around the pseudogap temperature. This result can be explained by spin–charge separation in the normal state of the HTSC materials.

7.3 Critical currents in bilayers of ferromagnets and YBCO

As mentioned before, this section deals with the magnetic interaction of HTSC/FM bilayers epically with the flux-line pinning effect. By means of quantitative magneto–optical (MO) imaging and SQUID magnetometery the critical current density $j_{\rm c}$ of the YBCO layer in NM and FM/HTSC bilayer structures has been determined. As FM layer $La_{2/3}Ca_{1/3}MnO_3$, $La_{2/3}Sr_{1/3}MnO_3$, and $SrRuO_3$ buffer layers have been used. The results are compared with a paramagnetic/superconducting bilayer.

7.3.1 Sample geometry

The as grown bilayer structure on $SrTiO_3$ single crystalline substrates have a dimension of 5×5 mm^2. By means of conventional lithography the 5×5 mm^2 bilayers are patterned to 1×1 mm^2, as shown in Fig. 7.16.

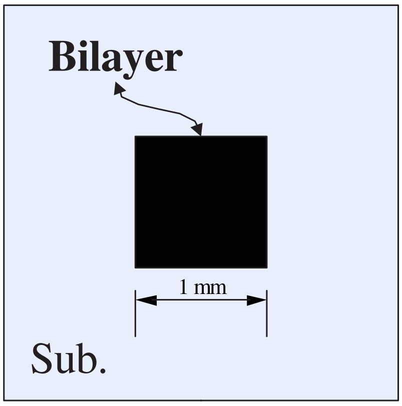

Figure 7.16: Sketch of the chosen sample geometry for magneto–optical measurements. $La_{2/3}Ca_{1/3}MnO_3$ (LCMO) and $YBa_2Cu_3O_{7-\delta}$ (YBCO) are grown by pulsed laser deposition onto 5×5 mm^2 $SrTiO_3$ (100) single crystalline substrates. By means of chemical lithography the 5×5 mm^2 film area is patterned to 1×1 mm^2.

7.3.2 LCMO/YBCO bilayers

Previous magneto-optical as well as transport current experiments to determine $j_{\rm c}$ in single layer YBCO films deposited on $SrTiO_3$ single crystals revealed a homogeneous $j_{\rm c}$ distribution with typical values (at 5 K) of $j_{\rm c}$= 3×10^{11} A/m^2 [174]. This value is regarded as a standard for high quality YBCO thin films in literature.

In Fig. 7.17(a) and (b) the magnetooptically determined current density distribution of a 50 nm LCMO/50 nm YBCO bilayer is shown in an external magnetic field of $\mu_\circ H_{\rm ext}$ = 3 mT applied perpendicular to the film plane at T = 7 K. The image in Fig. 7.17a is taken

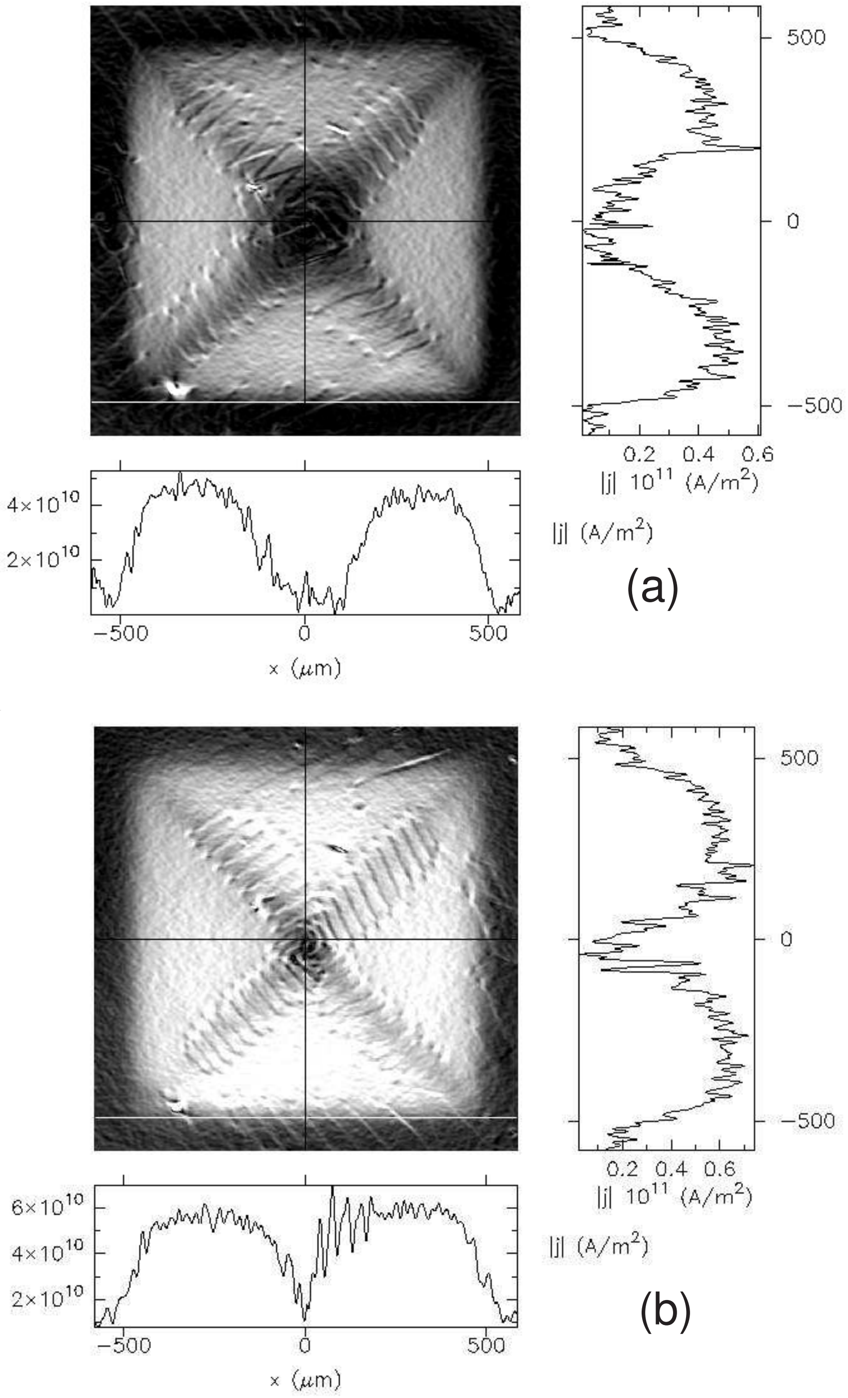

Figure 7.17: Magnitude of the critical current density in LCMO/YBCO 50 nm/50 nm bilayers at T = 7 K, using an external field of $\mu_\circ H_{\rm ext} \approx 3$ mT after ZFC (a) and by decreasing the field from 200 mT (b). The gray scale refers linearly to values of $j_{\rm c}$ = 5×10^9A/m^2 (black) and $j_{\rm c}$ = 6×10^{10}A/m^2 (white).

after zero–field–cooling (ZFC) whereas Fig. 7.17b represents the current distribution in decreasing field after applying $\mu_\circ H_{\rm ext}$ = 200 mT again at $\mu_\circ H_{\rm ext}$ = 3 mT. The gray scale representation shows an increase of the current density of $j_{\rm c}$ = 4×10^{10}A/m^2 (a) to $j_{\rm c}$ =

6×10^{10}A/m^2 (b). Only the part with penetrated flux which is in the critical state has to be considered.

It is to remark that both images show zig-zag structures along the sample diagonals. These patterns are generated by domains in the indicator film. Usually, the contrast generated by the currents in the superconductor is much stronger than the magnetic contrast of the domains. But in this case a thin film with low current density, the method is close to the experimental limit, and these domain patterns appear. Nevertheless, these domain patterns do not effect the flux line system in the superconductor. The domains are easily movable and their position is governed by the position along the samples diagonals.

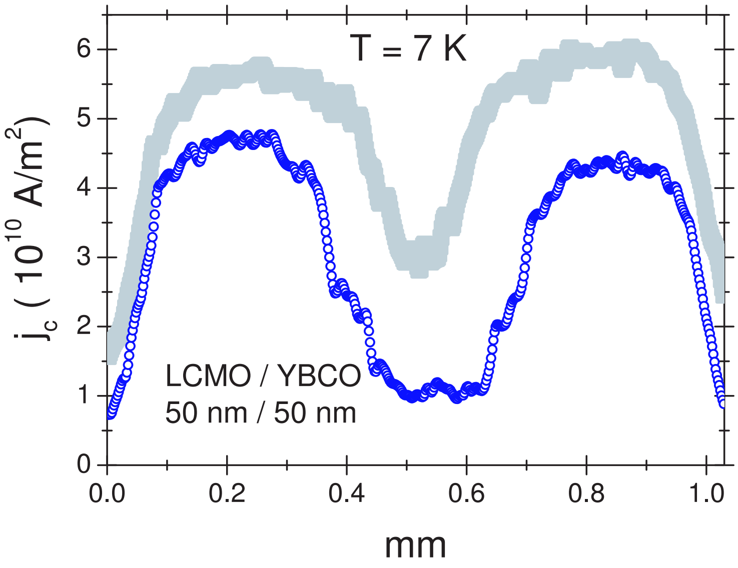

Figure 7.18: Averaged current density profiles along a horizontal line in the center of the two images in Fig. 7.17a and b. The lower curve refers to the zero-field cooling measurement.

For a quantitative comparison now two profiles are taken along the solid black lines of both measurements and are plotted in the same diagram in Fig. 7.18. The lower profile in Fig. 7.18 corresponds to the ZFC measurement, whereas the upper one is determined after the application of $\mu_\circ H_{\rm ext}$ = 200 mT and then reduced to 3 mT. The averaged enhancement Δj_c = 1.5 $\times10^{10}$ A/m^2 corresponds to an additional pinning force density per length of 30 μNm^{-1}, and is due to the magnetic history of the ferromagnetic layer.

That the “magnetic history” is the only difference between the two measurements it can be ruled out that a field-dependence of the critical current density causes the above effect. In this case the increase of the critical current density of the superconductor has its origin in the magnetic state of the ferromagnetic LCMO layer. It has been shown that the vicinity of magnetic domain walls can cause a pinning force on the flux lines in the superconductor [175, 177–179, 182].

Qualitatively, the enhancement of j_c can be associated with the magnetic domain structure and its magnetic stray field interacting with that of the flux-line lattice.

For a deep understanding of this effect an experimental approach is performed addressing the following topics:

- a) dependence of j_c on the YBCO thickness.
- b) dependence of the domain structure (material).
- c) electronically decoupling of the layers by a magnetically transparent spacer.

The contributions of magnetic pinning in bilayer structures should vary with the relative size of the interaction volume of flux lines and magnetic structure; i.e. the effect is expected to be dependent on the YBCO film thickness.

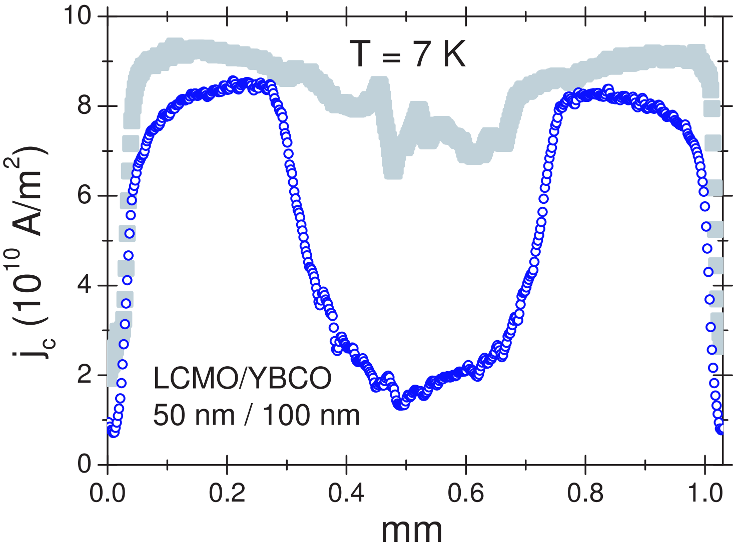

Figure 7.19: Averaged current density profiles for a 50 nm LCMO/100 nm YBCO bilayer. The lower curve refers to the zero-field cooling measurement.

MOI measurement of j_c on 50 nm LCMO/100 nm YBCO reveal $\Delta j_c = 0.8\times10^{10}$ A/m^2 as shown in Fig. 7.19. It is just about half of the value of 50 nm LCMO/50 nm YBCO bilayers, Fig. 7.18. It is important to note that the critical current density itself depends on the layer thickness of YBCO. In case of the thicker bilayer a value of j_c of around 8–9$\times10^{10}$ A/m^2 is found which is a substantial increase to the j_c of the 50 nm/50 nm bilayer depicted in Fig. 7.18.

The decreasing influence of the ferromagnet with increasing YBCO layer leads to the fact that the effect is generated by properties near the interface between both layers. The interaction of the magnetic domain structure of the ferromagnet and the flux lines in the superconductor causes an additional constant pinning force on the flux lines and therefore an enhancement of the critical current.

7.3.3 SrRuO$_3$ /YBCO bilayer

For a comparison with the experiments using the colossal magnetoresistance material LCMO, similar samples with SrRuO$_3$ as another ferromagnetic layer have been studied. The main results shown here are performed on 50 nm SRO/100 nm YBCO bilayers.

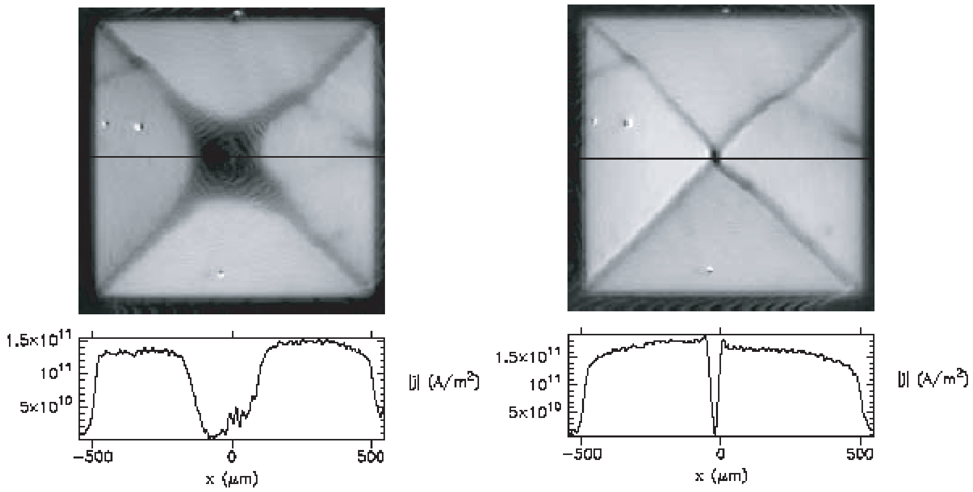

Figure 7.20: Gray scale representations of the magnitude of the critical current density of a 50 nm SRO/100 nm YBCO bilayer. The corresponding profiles are taken along the solid black lines. The left image refers to an external field of $\mu_\circ H_{\text{ext}}$ = 16 mT after zero-field cooling, the right image is taken at $\mu_\circ H_{\text{ext}}$ = 16 mT after having applied an external field of $\mu_\circ H_{\text{ext}}$ = 200 mT. Bright parts indicate a high current density.

Figure 7.20a and b show the gray scale representation of the magnitude of the critical current distribution and the corresponding profiles along the solid black lines. There is a clear difference in the averaged values for j_c measured at 16 mT in the case of zero field cooled samples (left image) and in 16 mT after applying an external field of $\mu_\circ H_{\text{ext}}$= 200 mT (right image). A quantitative analysis of the averaged values reveals an enhancement of Δj_c = 3×10^{10} A/m^2 with an average value for j_c = 1.3×10^{11} A/m^2 for the measurement after zero field cooling.

Figure 7.21 shows two current density profiles for the measurements after zero-field cooling (bottom) and in decreasing field (top). A distinct increase in the critical current is found for the second measurement after the application of a high external field of $\mu_\circ H_{\text{ext}} \approx$ 200 mT. The kinks in the left part of the profiles are is related to a defect in the YBCO film.

For a more detailed analysis the current density in the superconducting film is determined while systematically changing the magnetized state of the ferromagnetic layer. In particular, the sample is cooled to T = 7 K in zero field, afterwards the critical current in the superconductor is determined while performing a magnetic hysteresis loop in terms

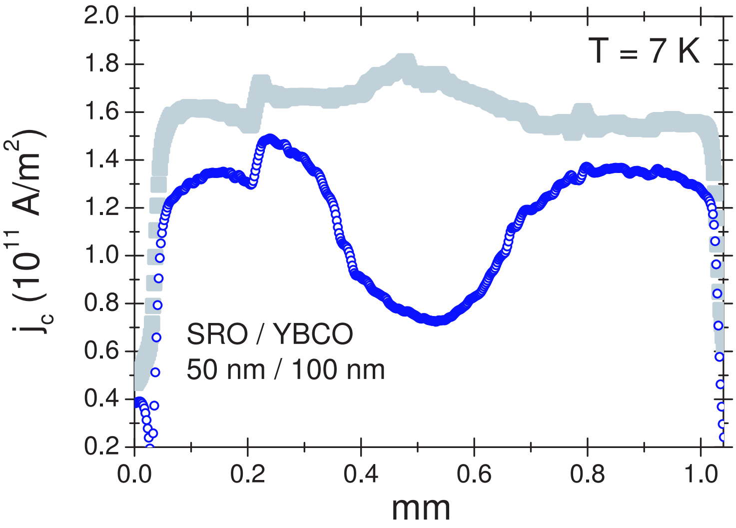

Figure 7.21: Averaged current density profiles for the two measurements in Fig. 7.20. The profiles were taken over a 200 μm wide, horizontal strip across the center of the sample. The bottom profile refers to the measurement after zero-field cooling, the measurement in decreasing field is shown by the upper curve.

of the external field. The external field cycle is performed to an upper value of $\mu_\circ H_{\rm ext}$ = 200 mT whereas the current density is determined below external fields of $\mu_\circ H_{\rm ext}$ = 50 mT to avoid saturation of the magneto-optical layer.

Figure 7.22 shows the dependence of the critical current density on the external magnetic field. The results were obtained by averaging the magnitude of the current density in the flux penetrated areas of the sample which are in the critical state.

Two branches of the critical current density appear in the measurement. The lower branch refers to the increase of the external magnetic field after zero-field cooling. It is found that the current density increases with increasing external magnetic field up to a value of about 1.4×10^{11} A/m^2. After the application of $\mu_\circ H_{\rm ext}$ = 200 mT the external field is gradually reduced and the current density shows higher values which is depicted in the upper branch in Fig. 7.22. As long as the external field is positive the current density has a value of about 1.5×10^{11}A/m^2. With the external magnetic field changing sign the current density reduces slightly to a value of about 1.3×10^{11} A/m^2 for a negative field of $\mu_\circ H_{\rm ext}$ = -16 mT. Note, that the magnitude of the magnetic field refers to the *external* field, the relation between critical current and *local* magnetic field shows that the hysteretic effect is not caused by the pinning properties of the superconductor itself.

Figure 7.22 demonstrates that the critical current density in ferromagnet/superconductor bilayers is unambiguously related to the magnetization state of the ferromagnetic layer. The critical current density can show an enhancement of about $\Delta j_{\rm c} \approx 3{\times}10^{10}$A/m^2 induced by a favorable magnetization of the ferromagnet. This is related to an additional pinning force of $F_{\rm p} = 6{\times}10^{-12}$ N per flux line or a force density per length of $f_{\rm p}$ =

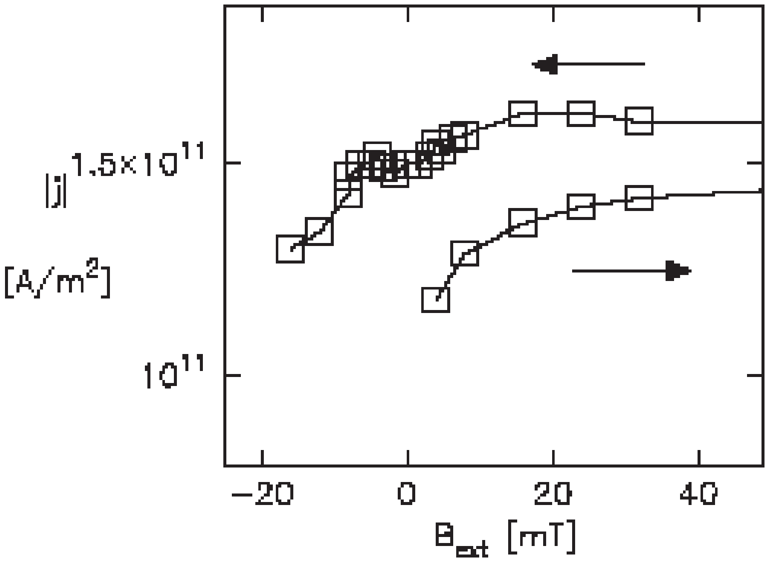

Figure 7.22: Hysteresis of the critical current density in the superconducting layer while performing a loop of the external magnetic field. The lower branch corresponds to a rising field after zero-field cooling, the upper branch shows the current density for a gradually reduced field after the application of $\mu_\circ H_{\text{ext}}$ = 200 mT.

60 μN/m, respectively. Helseth *et al.* found an upper limit for the flux line pinning force of a Bloch wall in the range of $F_{\text{p}} \approx 1 \times 10^{-10}$N [177] which can nicely explain the experimental data.

7.3.4 LaNiO$_3$ / YBCO bilayer

Qualitatively, it is demonstrated that the magnetic buffer layer causes a hysteretic behavior in j_{c} and an enhancement of j_{c} after magnetizing the LCMO or SRO film perpendicular to the film plane. The reference sample LaNiO$_3$ /YBCO does not show the hysteretic effect, and displays the features of a single layer YBCO film.

The gray scale images in Fig. 7.23 as well as the profiles given below clearly show two features. First, the current density has a magnitude of about $j_{\text{c}} \approx 2 \times 10^{11}$A/m^2 which is comparable to current densities that are found in single layer YBCO films. The important point of the measurements shown in Fig. 7.24 is, however, that no distinct difference occurs between the two scenarios before and after magnetizing the bilayer system. This clearly indicates that the current enhancement, that has been detected for the ferromagnet/superconductor bilayers is directly connected with a magnetization process in the ferromagnetic layer.

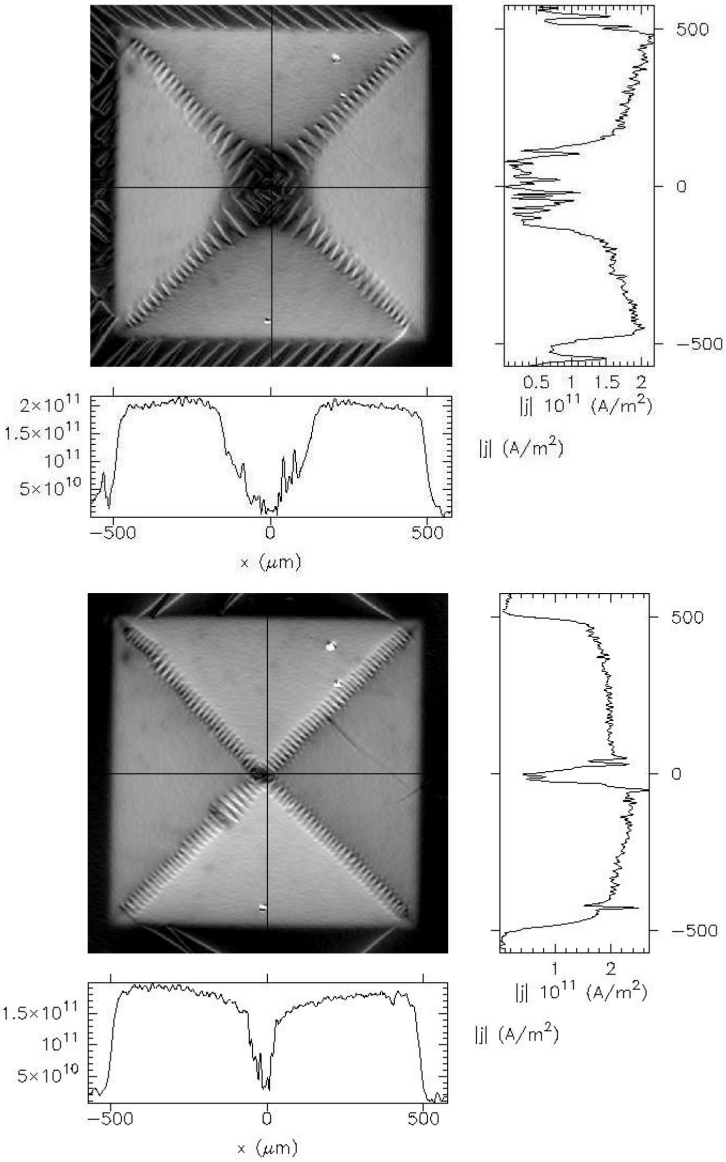

Figure 7.23: Gray scale representations of the magnitude of the critical current density of a 50 nm LNO/50 nm YBCO bilayer. The corresponding current profiles are taken along the solid black lines. The top image refers to an external field of $\mu_\circ H_\mathrm{ext}$ = 12 mT after zero-field cooling, the bottom image is taken at $\mu_\circ H_\mathrm{ext}$ = 12 mT after having applied an external field of $\mu_\circ H_\mathrm{ext}$ = 200 mT. Bright parts a indicate a high current density.

7.3.5 Electronic decoupling and temperature dependence

The ferromagnet/superconductor bilayers investigated sofar have been grown on top of each other. This means they are coupled to each other electronically and magnetically. To rule out electronic interaction between both layers, in the next step an interlayer of insulation $SrTiO_3$ is grown between the layers to achieve an electronic decoupling.

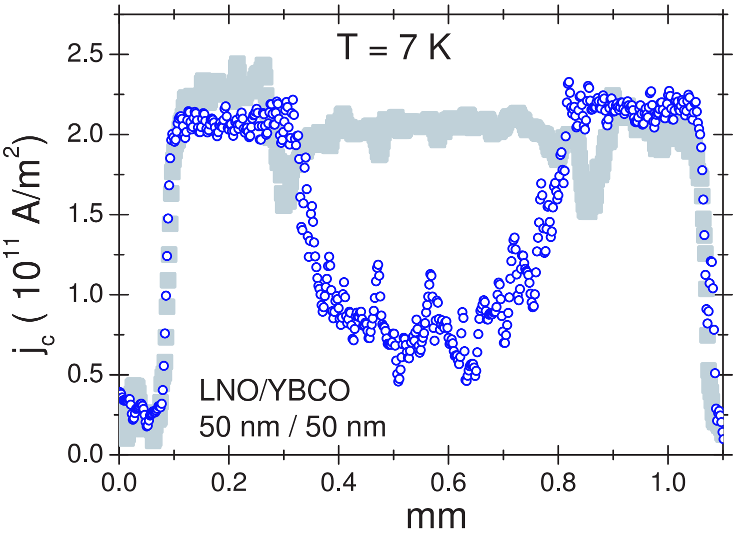

Figure 7.24: Averaged current density profiles for the two measurements in Fig. 7.23. The profiles were taken over a 200 μm wide, horizontal strip across the center of the sample. The black profile below refers to the measurement after zero-field cooling, the measurement in decreasing field is depicted gray.

7.3.5.1 Sample geometry

$SrTiO_3$ single-crystalline (100) oriented substrates (STO) and $LaSrGaO_4$ (LSGO) are used to grow thin LCMO films with a typical thickness of d_{fm} = 50 nm. The important difference between the used substrate materials is the lattice constant which leads to films under *tensile* strain in case of the STO substrate and under *compressive* strain in case of the LSGO substrate, as shown in Fig. 6.1. To rule out any electronic interaction or spatially varying proximity effects that can lead to additional pinning effects [180] a thin layer of 5 nm $SrTiO_3$ is grown directly onto the LCMO film. A sketch of the geometry of the used samples is given in Fig. 7.25.

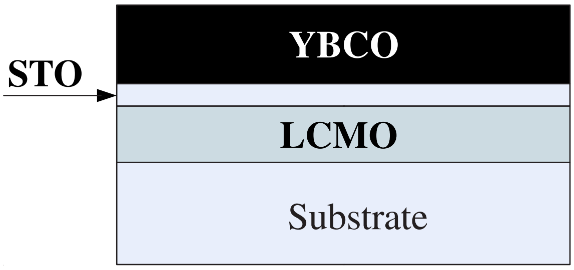

Figure 7.25: Sketch of the geometry of the heterostructures consisting of a LCMO layer, a decoupling STO layer with a thickness of 5 nm and a YBCO layer, all grown by pulsed laser deposition.

7.3.5.2 Decoupling of FM and HTSC layers

In a first experiment the temperature-dependent magnetization of a sample consisting of a LCMO layer with a thickness of d_{LCMO} = 50 nm, a 5 nm STO decoupling layer and a YBCO layer with a thickness of d_{YBCO} = 100 nm is shown in Fig. 7.26. The measurement has been performed after zero-field cooling to T = 5 K in an afterwards applied external field of H_{ext} = 10 Oe. The orientation of the field is parallel to the film plane. The magnetization is measured with a SQUID magnetometer up to T = 300 K (bottom curve) and back down (top curve) to T = 5 K whereas the external field remains constant at H_{ext} = 10 Oe.

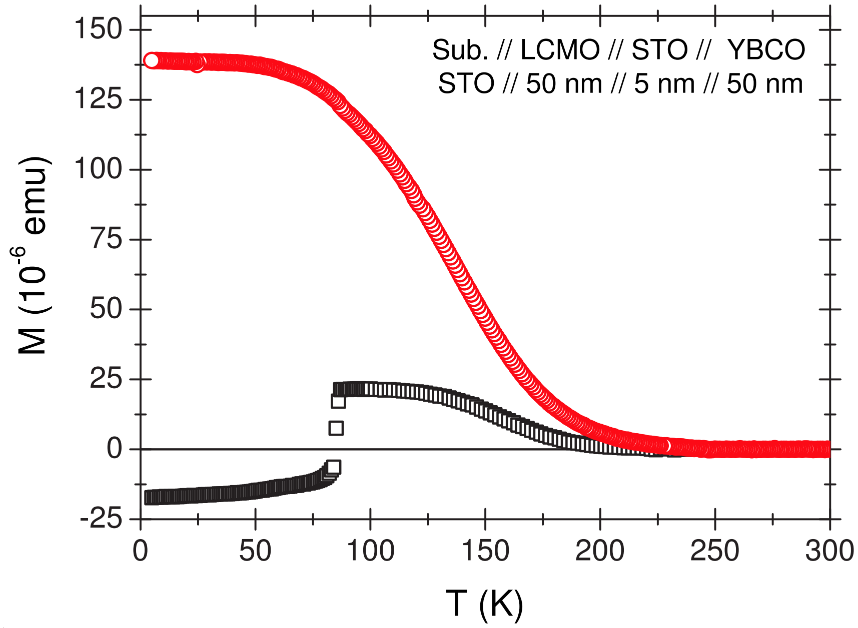

Figure 7.26: Temperature-dependent magnetization of a heterostructure of 50 nm LCMO/5 nm STO/100 nm YBCO on a $SrTiO_3$ substrate. The upper curve shows the field-cooled the lower the zero-field cooled, measurement. The in-plane external field for detection is $H_{\text{ext}} = 10$ Oe. The results show a ferromagnetic ordering in the heterostructure at $T_{\text{Curie}} = 245$ K and a superconducting transition at $T_c = 87$ K.

The data in Fig. 7.26 clearly show that the sample orders ferromagnetically at around T_{Curie} = 245 K and at T = 87 K a transition to superconductivity occurs. This can be seen from the diamagnetic signal that occurs below T = 87 K in the zero-field cooled measurement (bottom curve). This result clearly demonstrates that below T = 87 K both superconducting and magnetic ordering are present in the sample. The same bilayer structure with thicknesses of the compound of d_{LCMO} = 50 nm and d_{YBCO}= 50 nm without $SrTiO_3$ decoupling layer shows a lower ferromagnetic ordering $T_{\text{Curie}} \geq 135$ K, and $T_{\text{sc}} \geq 87$ K, Fig. 7.2. This indicates that the $SrTiO_3$ decoupling layer switches off the electronic interaction.

The focus is now on the critical current density of the superconducting film at low temperatures. For this purpose, magnetic hysteresis loops are measured at T = 5 K is depicted in Fig. 7.27. The sample is cooled at zero field to T = 5 K and an external field oriented perpendicular to the film plane is swept up to H_{ext} = 3 kOe, then to H_{ext} = -3 kOe and back to H_{ext} = 3 kOe again. The measured magnetization shows a behavior typical for a high-temperature superconductor with strong pinning. Starting at H_{ext} = 0 a diamagnetic signal of the sample is found that is saturated around 100 Oe (virgin curve). At this field the superconductor achieves the fully flux penetrated state and the modulus of the magnetization $|M|$ is proportional to the critical current density j_{c} of the sample. If the critical current density was constant, a square-shaped hysteresis loop would be obtained. The decrease towards higher magnetic fields is related to field-dependent flux line pinning. However, the loop in Fig. 7.27 is only symmetric with respect to the origin and asymmetric to the $H = 0$ axis. The magnetization at a fixed external field clearly depends on the direction of the field sweep. This means not only the magnitude of the external field influences the current density also the direction of field changes plays a substantial role.

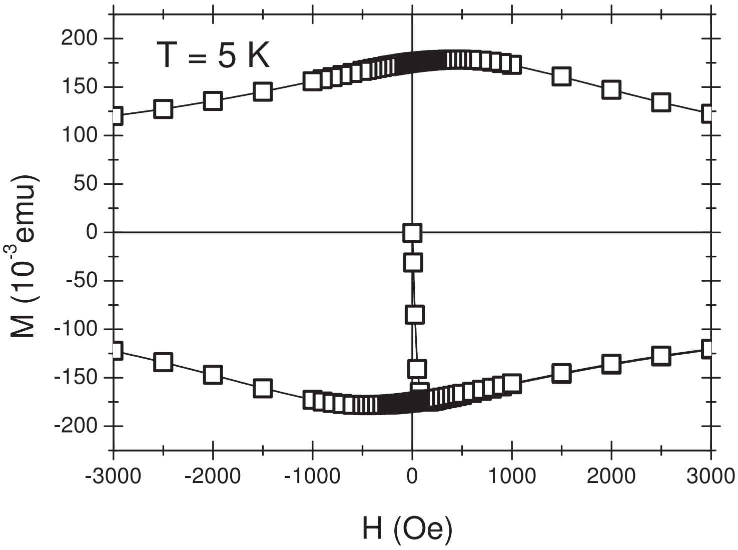

Figure 7.27: Magnetization loop of a heterostructure consisting of 50 nm LCMO and 100 nm YBCO with decoupling layer obtained at T = 5 K. The hysteresis loop shows no axial symmetry with respect to the vertical axis.

A better way to present this magnetic effect is plotting the difference of the magnitude of the magnetization $\Delta |M|$ and thus the critical current density at fixed external fields. This is done in Fig. 7.28.

This curve shows two distinct maxima of $\Delta |M|$ that are located symmetrically to H = 0. The maximum value of $\Delta \mid M \mid$ is about $\Delta \mid M \mid$ = 0.017 emu which is in the order of 10% of the entire magnetization. This difference can now be identified with the pinning of

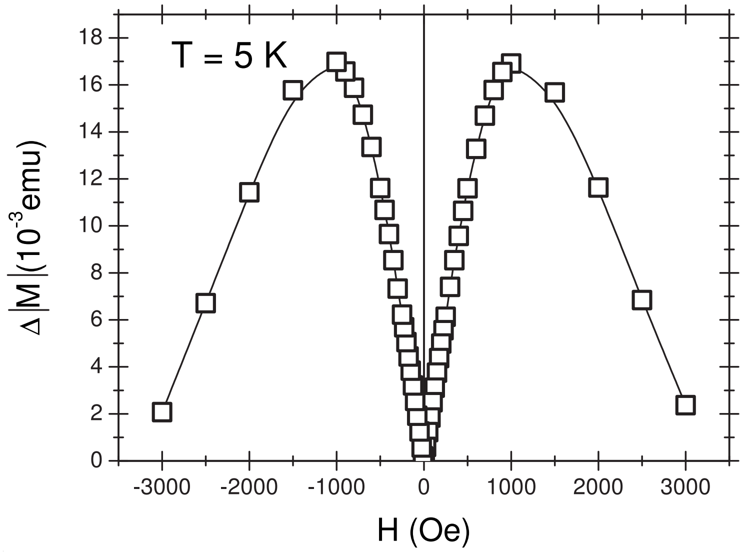

Figure 7.28: Modulus of the difference $\Delta\,|M|$ between the two branches of the magnetization loop shown in Fig. 3. This represents the contribution of magnetic flux line pinning in the heterostructure.

flux lines due to the vicinity of the ferromagnetic layer. Note, that the magnetization of the ferromagnet is of course also included in Figs. 7.27 and 7.28. However, a measurement of a comparable single layer of LCMO gives magnetization values in the order of 10^{-4} emu which is at least more than one order of magnitude smaller than the observed effect. Additionally, it is not possible to explain a pronounced maximum symmetric to H = 0 of the curve in Fig. 7.28 by ferromagnetic ordering.

With this knowledge we can directly conclude that the observed effect is originated by magnetic pinning of the flux lines in the superconductor. The magnetic pinning force that acts on an individual flux line can be extracted by applying the Bean model on the magnetization data. The Bean model allows the determination of the critical current density in the superconducting film by assuming a homogeneous and constant current density throughout the whole sample. In case of the presented data of the bilayer consisting of a 100 nm YBCO film we find a critical current density of about $j_c \approx 1.0 \times 10^{11}$A/m^2 which is in very good accordance to magneto–optical measurements at systems without decoupling layer Fig. 7.19. Additionally, the corresponding magnetic pinning force on an individual flux line can be determined to $F_\mathrm{p} \approx$ 1.5 pN. Similar values are found for magnetic pinning forces in interacting systems of ferromagnets and classical superconductors [175].

The interaction of the flux line lattice in the YBCO film and the magnetic domain structure in the ferromagnetic LCMO depends, of course, strongly on the orientation of the domains. The local magnetization of a thin LCMO layer with a thickness of d_fm = 50 nm can be controlled by using substrates with different lattice parameters to create various strain fields during epitaxial growth. It has been shown that LCMO thin films that grow under compressive strain show an out-of-plane orientation of the magnetization whereas a growth with no strain or under small tensile strain fields leads to an in-plane magnetization in these films [181]. The orientation of the easy axis of the LCMO film should therefore lead to different magnetic pinning properties of bilayers containing these manganite films.

Figure 7.29 shows the magnetic pinning $\Delta |M| / |M|$ for four different kinds of bilayers. First, the bilayer consisting of 50 nm LCMO and 100 nm YBCO grown on STO that already has been introduced in Figs. 7.27 and 7.28, second and third, the same structure with a thinner and a thicker YBCO layer with d_{sc} = 50 nm and d_{sc} = 150 nm, respectively, and finally, a bilayer structure containing a 50 nm LCMO and a 50 nm YBCO film grown under compressive strain on a LaSrGaO$_4$ (LSGO) substrate.

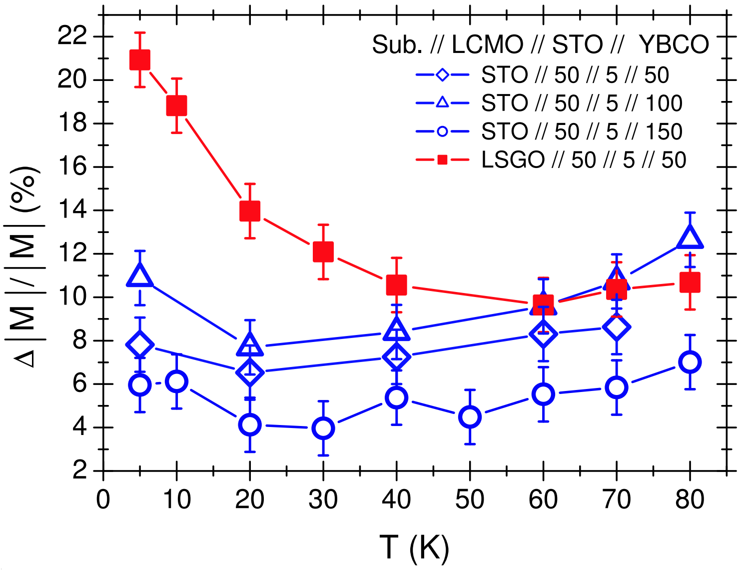

Figure 7.29: Temperature dependence of the magnetic pinning effect $\Delta |M| / |M|$ for different heterostructures. Samples grown on STO (open symbols) show a nearly constant effect over the whole temperature range which decreases for a YBCO thickness larger than 100 nm. The temperature dependence in case of the heterostructure grown under compressive strain on LSGO (full squares) shows a distinctly different behavior.

The results in Fig. 7.29 clearly show that all structures grown on STO substrates under tensile strain show a very similar behavior. For the two thinner structures we observe a nearly constant contribution of the magnetic pinning in the order of 10 % over the whole temperature range. The thickest bilayer shows also a temperature-independent magnetic pinning contribution of about 5-6 % which can easily be understood concerning the thicker YBCO film where the magnetic structures are smeared out over the thickness. A totally different behavior exhibits the structure that is grown under compression strain on the LSGO substrate. At low temperatures we find a magnetic contribution to the flux line pinning of more than 20 %, this value decreases monotonically to about $\Delta\left|M\right|/\left|M\right|$=10 % above T = 50 K. This increase of the effect in case of a perpendicular magnetization of the ferromagnet is also predicted by theoretical considerations [182]. The results presented in Fig. 7.29 directly show that a change of the domain pattern in the ferromagnet directly affects the properties of the magnetic pinning effect. This strongly supports the model that the magnetic stray fields of the domain pattern in the ferromagnet cause a substantial pinning force density on the flux lines in the superconductor.

The results presented so far concern the flux pinning in bilayers while performing full magnetic hysteresis loops. It has been found in magneto–optical measurements that the critical current density in bilayers without decoupling layer exhibits strong differences between the zero-field cooled state and the field-cooled state, Figs. 7.18 and 7.21. This effect should also appear in the virgin curve of the magnetic hysteresis loop. Although one has to be careful because the magnetization is only a measure of the critical current density if the whole superconductor is in the critical state, i.e. magnetic flux is fully penetrated into the sample.

Fig. 7.30 shows the magnetization with respect to the external magnetic field for a bilayer with decoupling layer that consists of a 50 nm LCMO film and a 50 nm YBCO film grown on a STO substrate. The magnetization loop is measured at T = 70 K, at this temperature the fully penetrated state is achieved at an external field of about H = 30 Oe.

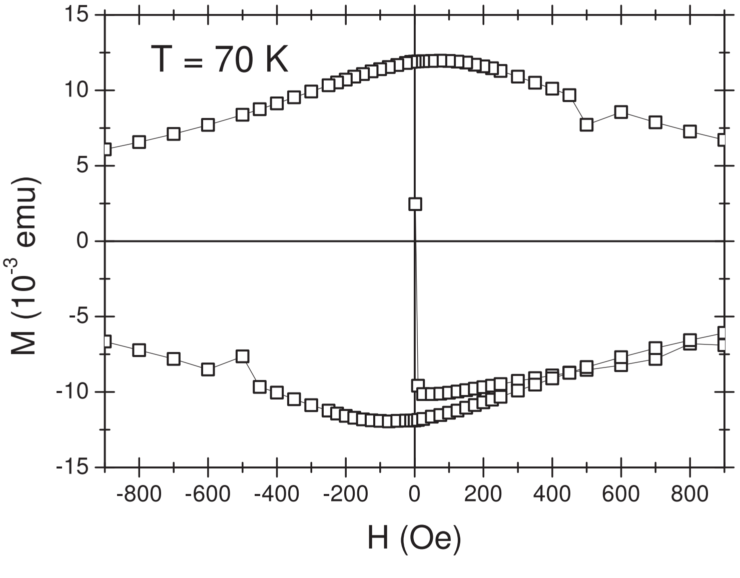

Figure 7.30: Hysteresis loop of a 50 nm LCMO/5 nm STO/ 50 nm YBCO heterostructure on a STO substrate, obtained at T = 70 K. In this measurement a substantial reduction of the magnetization in the virgin branch occurs.

In contrast to the result presented in Fig. 7.27 a distinct difference between the virgin curve and the complete magnetization loop is found. The maximum of the magnetization in the virgin curve is about 25 % smaller. This is strongly related to the results that are found in the magneto–optical measurements of bilayers without decoupling layer that are mentioned above. Up to now, this behavior can not be explained in detail, it is suggested that the formation of the magnetic domains in the LCMO layer is strongly affected by the flux line lattice in the superconductor, especially at temperatures between T = 50 K and T_c of the YBCO film. Detailed knowledge about this mechanism can only be found by imaging the development of the domain structure under varying magnetic fields in these heterostructures but this purpose has not been realized so far.

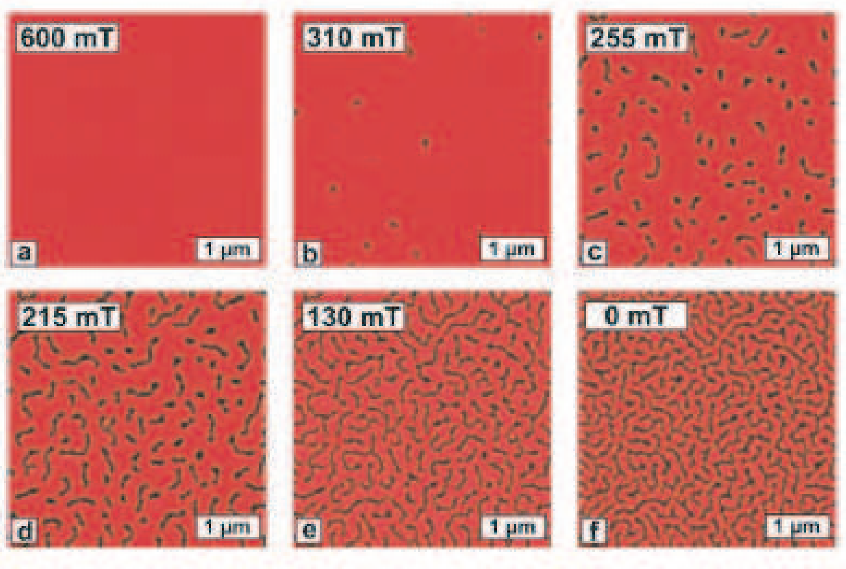

Figure 7.31: Domain structures of a $La_{2/3}Sr_{1/3}MnO_3$ thin film recorded along the decreasing branch of the major hysteresis loop after Schwarz *et al.* [183].

7.3.6 Magnetic domain structures of the ferromagnetic layer in FM/HTSC bilayers

A detailed investigation is done to see the magnetic domains of ferromagnetic layer, *first* in single a layer, *second* in a bilayer. The main question here is, if the magnetic domain structure of the FM layer behaves similar in both the single layer and the bilayer?

The magnetic domain structure obtained by magnetic force microscopy (MFM) for a single layer of LSMO taken from Ref. [183] is shown in Fig.7.31. Figure 7.31 displays six exemplarily obtained MFM images recorded on the decreasing branch of the hysteresis loop. Bright and dark regions correspond to attractive and repulsive magnetostatic interactions between the gradient of the tip stray field and the magnetic poles at the surface. In saturation, Fig. 7.31a, the contrast is homogeneous. At $\mu_\circ H_{\text{ext}}$ = 310 mT,

Fig. 7.31b, several circular domains are already nucleated. After reducing the field further, Figs. 7.31c—7.31e, the domains become elongated. In remanence Fig. 7.31f, about 44.7% (7.152μm^2) of the scan range (16μm^2) reversed their polarization. A maze type pattern with a mean domain width of 79 nm has evolved.

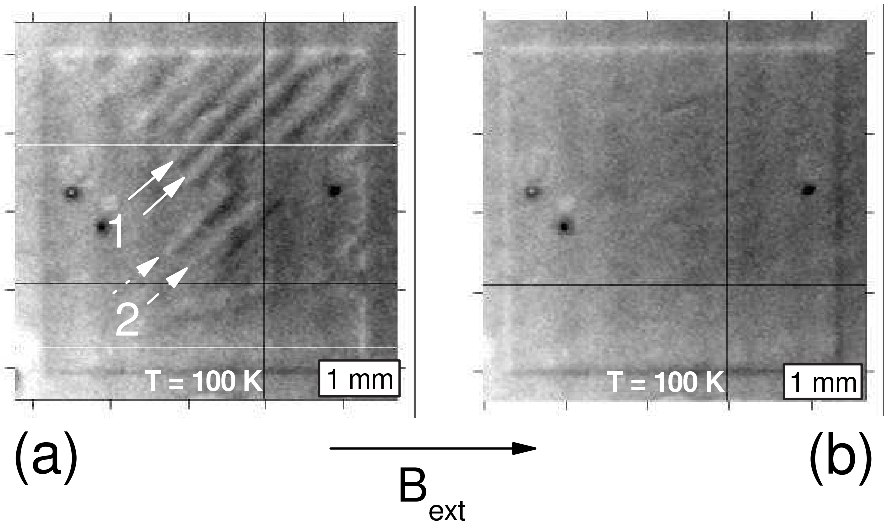

Figure 7.32: Magnetic domain structures of La$_{2/3}$Sr$_{1/3}$MnO$_3$ thin film (top layer) at T = 100 K (a) using the MO technique in LSMO/YBCO/LSMO heterostructure. (b) Removing the magnetic domains by applying a small in–plane magnetic field of some tens of millitesla. Note, that the width of the domains is with $w \approx 50$ μm nearly 3 orders of magnitude larger than for the LSMO single layer.

In contrast to the single layer of La$_{2/3}$Sr$_{1/3}$MnO$_3$ a much larger magnetic domain structure has been found for a LSMO/YBCO/LSMO heterostructure using the magnetooptical–technique as shown in Fig. 7.32a and b. The image shows parallel magnetic domains, Fig. 7.32a, in the upper part of the sample that are oriented along the film diagonal (pointed with arrows). These domains are oriented out–of–plane and can be removed by applying a small in–plane magnetic field of some tens of millitesla as shown in Fig. 7.32b.

Figure 7.33 shows the development of the out–of–plane magnetic domain by changing the temperature of the film. Figure 7.33 shows four different images taken in the remanet state at T = 30 K and 70 K (below the superconducting transition) and at T = 100 K and 125 K (above the superconducting transition). Two important things can be seen, the magnetic domain structure is present below and above the superconducting transition and the width of the domains is constant in the whole temperature range.

These magnetic domains in bilayer structures suggest that the ferromagnetic ordering is completely different compared to a manganite single layer.

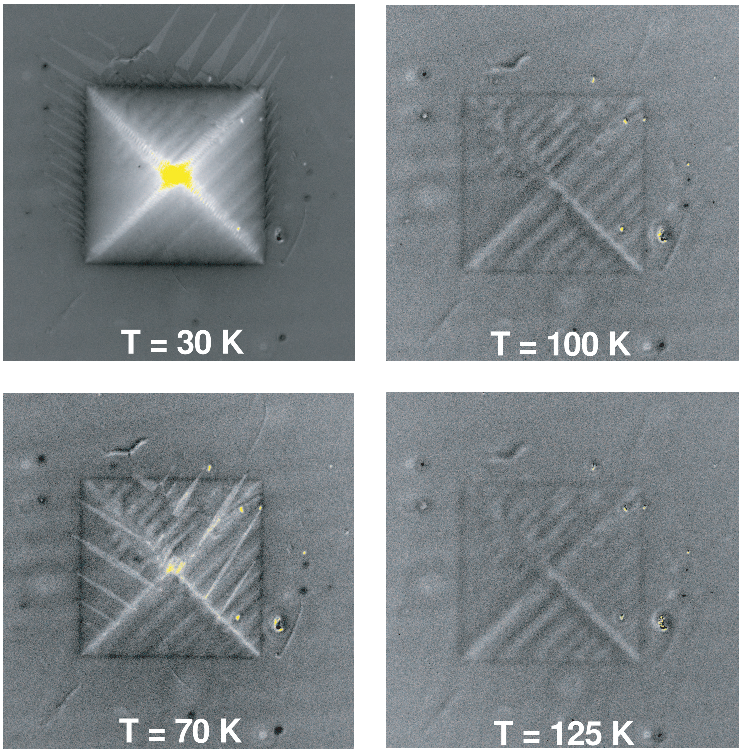

Figure 7.33: Magnetic domain structures in remanent state versus temperature of a LSMO/YBCO/LSMO heterostructure at T = 30 K, 75 K, 100 K, and 125 K using the MO technique. Note, with increasing temperature from far below superconducting transition temperature T_c into far above T_c the size of magnetic domains is fixed to roughly $w \approx 50$ μm.

Not only the magnetic domain size has been modified due the YBCO layer but also the coercive field H_c of the magnetic layer has increased. For LCMO and/or LSMO single layer $H_c \approx 140$ Oe is modified to $H_c \approx 200$ Oe in bilayer structures.

These results shows that it is not possible to describe a bilayer of manganites and YBCO by a dominant ordering mechanism (superconductor or ferromagnet with small perturbation of the other component. The combination of these materials in thin epitaxial structures leads to a material that has completely new properties. In recent investigations by neutron scattering experiments, it seems to be likely that even an antiferromagnetic layer can be present at the interface between LCMO and YBCO [184]. Such an antiferromagnetic layer would also show a substantial influence on the properties of the flux line lattice in the superconductor and he domain pattern in ferromagnet.

7.3.7 Summary

The superconducting critical current density in bilayers consisting of high-temperature superconducting YBCO and ferromagnetic LCMO strongly depends on the magnetization state of the ferromagnetic layer. The contribution of magnetic pinning to the critical current density can achieve values of up to 30 % and is present over the whole temperature range. Inserting a thin insulating layer in the bilayer structure leads to an electronic decoupling of both films and identifies the magnetic stray fields of the ferromagnetic layer as origin for the observed effects. It is found that a modification of the magnetic properties of the manganite layer by substrate induced strain fields leads to a change of the temperature dependence of the magnetic pinning force density.

Chapter 8

Summary

The interaction of ferromagnetism and superconductivity is studied in multilayers of the ferromagnet $La_{2/3}Ca_{1/3}MnO_3$ and the superconductor $YBa_2Cu_3O_{7-\delta}$. The fact that the *ab*-plane lattice parameters of these materials are very similar allows an epitaxial growth of LCMO/YBCO bilayers, heterostructures, and superlattices with structurally sharp interfaces. These LCMO/YBCO structures represent adequate model systems to investigate the interaction of the two antagonistic ordering phenomena.

All samples in this work are grown by pulsed laser deposition. The best preparation conditions are found to grow LCMO/YBCO bilayers or superlattices on $SrTiO_3$ single crystals at a temperature of T_s = 780°C with a background oxygen pressure of 0.4 mbar in case of LCMO and 0.6 mbar in case of YBCO. X-ray diffraction measurements show a highly ordered *c*-axis oriented growth of both materials and results from *ab*-plane investigations of the films show also an alignment of the *in*-plane axes.

These bilayers and multilayers with high structural quality are investigated experimentally to study the interaction between the ferromagnetic ordered LCMO with high spin-polarization and the high-temperature superconducting YBCO.

The main results of this thesis can be subdivided into three parts:

First, the diffusion of spin-polarized quasiparticles into the superconductor is investigated on bilayers consisting of 50 nm LCMO and varying YBCO thicknesses:

- Using SQUID magnetometery and transport measurements it is found that all LCMO/YBCO bilayers show ferromagnetic and superconducting ordering at low temperatures.
- The critical temperature T_c of YBCO in LCMO/YBCO bilayers is strongly suppressed for thicknesses d_YBCO smaller than 30 nm.
- A theoretical model is developed that, based on the Parker-model for nonequilibrium superconductivity, is able to describe the experimentally found transition tem-

peratures for different YBCO thicknesses.

- With this model it is possible to determine the spin diffusion length (ξ_{fm}) into YBCO to be $\xi_{\mathrm{fm}} \approx 10$ nm at low temperatures.

Second, a sophisticated geometry for a LCMO/YBCO heterostructure is developed, that allows the injection of spin-polarized quasiparticles into the YBCO layer:

- The injection of currents through spin-polarized LCMO into YBCO leads to a pronounced drop of T_{c} , which is four times stronger compared to the injection current through non-spin polarized materials. This is regarded as evidence for injecting spins into YBCO.

- It is found that spin-polarized quasiparticles injection leads to a drop of the normal state resistivity $\rho_{\mathrm{ab-plane}}$(T) of YBCO at temperatures around T_d = 200 K.

- This drop of resistivity can be explained by an opening of the pseudogap in the YBCO film. The spin-charge separation model after P.W. Anderson suggest an interaction of the injected spin-polarized quasiparticles with the gap which leads to an enhanced conductivity.

- The drop of the resistivity is not found if the spin-polarized electrodes are either replaced by non-polarized materials or if a thin insulating $SrTiO_3$ layer decouples LCMO and YBCO.

Third, the critical current density j_{c} of YBCO in bilayers is determined locally using a quantitative magneto-optical technique:

- The critical current density j_{c} in ferromagnet/superconducting bilayers is strongly reduced compared to a YBCO single layer.

- Changing the magnetization state of the LCMO thin film influences directly the critical current density in the superconductor . This effect can originate a variation of j_{c} of up to 50%.

- The electronic decoupling of LCMO and YBCO by a thin $SrTiO_3$ layer does not change this scenario substantially. This identifies a magnetic interaction between the flux line lattice in the YBCO film and the domain pattern in the LCMO film as the origin of this effect.

This presented work can not be regarded to be a complete consideration of interactions between ferromagnets and high-temperature superconductors, even not for the more specific case of LCMO and YBCO. Especially, some open questions are now mentioned that should encourage further efforts on this issue:

- The drop in the normal state resistivity of YBCO under spin-polarized quasiparticle injection appears around the pseudogap temperature T^*. Using heavily underdoped YBCO, T^* shifts substantially and the resistivity drop should also.
- It is discussed that an antiferromagnetic phase is present at the interface of LCMO and YBCO. A confirmation of this phase by systematic exchange bias investigations would be very interesting.
- A substrate induced change of the domain structure of the ferromagnet should directly affect the magnetic flux line pinning. This could be done by using structured or vicinal cut substrates to grow the heterostructures on.

In conclusion, it has been shown that bilayers grown out of spin-polarized LCMO and superconducting YBCO show a variety of new physical phenomena. The transition temperatures T_c and T_Curie, the critical current density in the superconductor j_c and even the normal state resistance can be influenced by external parameters and/or the sample geometry. These bilayers might be good candidates for technical applications in the near future.

Bibliography

[1] K. Onnes, Leiden Commun. **124c** (1911).

[2] J. Bardeen, L. Cooper, and J. Schrieffer, Phys. Rev. **108**, 1175 (1957).

[3] W. Meissner and R. Ochsenfeld, Naturwiss **21**, 787 (1933).

[4] G. Bednorz and K. A. Müller, Z. Phys. B **64**, 18 (1986).

[5] F. London and H. London, Proc. Roy. Soc. A **149**, 71 (1935); F. London and H. London, Physica **2**, 341 (1935).

[6] V.L. Ginzburg and L.D. Landau, J.E.T.P. USSR **20**, 2064 (1950).

[7] G.M. Eliashberg, Sov. Phys. JETP 11, 696 (1960).

[8] W.L. McMillan, Phys. Rev. **167**, 331 (1968).

[9] N. L. Saini, H. Oyanagi, A. Lanzara, D. Di Castro, S. Agrestini, A. Bianconi, F. Nakamura, and T. Fujita, Phys. Rev. B **64**, 132510 (2001).

[10] L. Alff, et al., Nature **422**, 698 (2003).

[11] M. Kugler, O. Fischer, C. Renner, S. Ono, and Y. Ando, Phys. Rev. Lett. **86**, 4911 (2001).

[12] J. M. Harris, Z.-X. Shen, P.J. White, D.S. Marshall, M.C. Schabel, J.N. Eckstein, and I. Bozovic, Phys. Rev. B **54**, R15665 (1996).

[13] N.J. Curro, P.C. Hammel, B.J. Suh, M. Hucker, B. Buchner, U. Ammerahl, and A. Revcolevschi, Phys. Rev. Lett. **85**, 642 (2000).

[14] H. Takagi, B. Batlogg, H.L. Kao, J. Kwo, R.J. Cava, J.J. Krajewski, and W.F.P. Jr, Phys. Rev. Lett. **69**, 2975 (1992).

[15] B. Bucher, P. Steiner, J. Karpinski, E. Kaldis, and P. Wachter, Phys. Rev. Lett. **70**, 2012 (1993).

[16] A.N. Lavrov, Y. Ando, and S. Ono, EuroPhys. Lett **57**, 267 (2002).

[17] K. Takenaka, K. Mizuhashi, H. Takagi, and S. Uchida, Phys. Rev. B **50**, 6534 (1994).

[18] J.L. Tallon and J.W. Loram, Physica C **349**, 53 (2001).

[19] J. Orenstein, G.A. Thomas, A.J. Millis, S.L. Cooper, D.H. Rapkine, T. Timusk, L.F. Schneemeyer, and J.V. Waszczak, Phys. Rev. B **42**, 6342 (1990).

[20] A. Puchkov, D.N. Basov, and T. Timusk, J.Phys. Cond. Matt. **8**, 10049 (1996).

[21] Y. Wang, Z.A. Xu, T. Kakeshita, S. Uchida, S. Ono, Y. Ando, and N.P. Ong, Phys. Rev. B **64**, 224519 (2001).

[22] Yu.N. Ovchinnikov, S.A. Wolf, and V.Z. Kresin, Phys. Rev. B **63**, 064524 (2001).

[23] Yu.N. Ovchinnikov and V.Z. Kresin, Phys. Rev. B **65**, 214507 (2002).

[24] E.V.L. de Mello, M.T.D. Orlando, J.L. Gonzalez, E.S. Caixeiro, and E. Baggio-Saitovich, Phys. Rev. B **66**, 092504 (2002).

[25] E.V.L. de Mello, E.S. Caixeiro, and J.L. Gonzalez, Phys. Rev. B **67**, 024502 (2003).

[26] G.Q. Zheng, W.G. Clark, Y. Kitaoka and K. Asayama, Y. Kodama, P. Kuhns, and W.G. Moulton, Phys. Rev. B **60**, R9947 (1999).

[27] K. Gorny, O.M. Vyaselev, J.A. Martindale, V.A. Nandor, C.H. Pennington, P.C. Hamme, W.L. Hults, J.L. Smith, P.L. Kuhns, A.P. Reyes, and W.G. Moulton, Phys. Rev. Lett. **82**, 177 (1999).

[28] G.Q. Zheng, H. Ozaki, W.G. Clark, Y. Kitaoka, P. Kuhns, A.P. Reyes, W.G. Moulton, T. Kondo, Y. Shimakawa, and Y. Kubo, Phys. Rev. Lett. **85**, 405–408 (2000).

[29] P. Pieri, G.C. Strinati, and D. Moroni, Phys. Rev. Lett. **89**, 127003 (2002).

[30] P.W. Anderson, Science **235**, 1196 (1987), Phys. Rev. Lett. **64**,1839(1990); P.W. Anderson, Physica C **341-348**, 9 (2000), and P.W. Anderson, in *“The Theory of Superconductivity in the High–T_c Cuprates”*, edited by P.W. Anderson, Princeton Univ. Press, Princeton, NJ (1997).

[31] N. Nagaosa and P.A. Lee, Phys. Rev. B **45**, 966 (1992).

[32] P.A. Lee and N. Nagaosa, Phys. Rev. B **46**, 5621 (1992); P.A. Lee, Physica C **317**, 194 (1999); P.A. Lee, Physica C (in the press).

[33] J.H. Koo and G. Cho, Jou. Phys-Condens Mat. **15** (46), L729 (2003).

[34] C. Bernhard, D. Munzar, A. Golnik, C.T. Lin, A. Wittlin, J. Humlíček, and M. Cardona, Phys. Rev. B **61**, 618 (2000).

[35] R.S. Markiewicz, Phys. Rev. Lett. **89**, 229703 (2002).

[36] V.J. Emery and S.A. Kivelson, Nature **374**, 434 (1995).

[37] V.J. Emery, S.A. Kivelson, and O. Zachar, Phys. Rev. B **56**, 6120 (1997).

[38] J. Schmalian, S. Grabowski, and K.H. Bennemann, Phys. Rev. B **56**, R509 (1997).

[39] F. Schäfer, J. Schmalian, and K.H. Bennemann, Phys. Rev. B **58**, 15177 (1998).

[40] J. Schmalian, D. Pines, and B. Stojkovic, Phys. Rev. B **60**, 667 (1999).

[41] D.E. Sheehy, P.M. Goldbart, J. Schmalian, and A. Yazdani, Phys. Rev. B **62**, 4105 (2000).

[42] B. Giovannini and C. Berthod, Phys. Rev. B **63**, 144516 (2001).

[43] D. Manske, T. Dahm, and K.H. Bennemann, Phys. Rev. B **64**, 144520 (2001)

[44] C. Meingast, V. Pasler, P. Nagel, A. Rykov, S. Tajima, and P. Olsson, Phys. Rev. Lett. **86**, 1606 (2001).

[45] C. Timm, D. Manske, and K.H. Bennemann, Phys. Rev. B **66**, 094515 (2002).

[46] A.J. Millis and H. Monien, Phys. Rev. Lett. **70**, 2810 (1993).

[47] B.L. Altshuler, L.B. Ioffe, and A.J. Millis, Phys. Rev. B **53**, 415 (1996).

[48] J. Bobroff, H. Alloul, P. Mendels, V. Viallet, H.F Marucco, and D. Colson, Phys. Rev. Lett. **78**, 3757 (1997).

[49] Q. Si, Phys. Rev. Lett. **78**, 1767 (1997), and Physica C **341-348**, 1519 (2000).

[50] D.H. Martin, *"Magnetism in Solids"*, MIT Press (1967).

[51] L.-P. Levy, *"Magnetism and Superconductivity"*, Springer-Verlag (2000).

[52] G.T. Rado and H. Suhl, editors, *"Magnetism"*, volume IV, Academic Press (1966).

[53] G. Ortiz et al., Phys. Rev. Lett. **82**, 5317 (1999).

[54] J.C. Slater, Phys. Rev. **49**, 537 (1936).

[55] B.C. Stoner, Proc. Roy. Soc. **165A**, 372 (1938).

[56] J. Kübler, *"Theory of Itinerant Electron Magnetism"*, Oxford University Press, (2000).

[57] G.H. Jonker and J.H. Van Santen, Physica **16**, 337 (1950).

[58] J.H. Van Santen and G.H. Jonker, Physica **16**, 599 (1950).

[59] G.H. Jonker, Physica **22**, 707 (1956).

[60] J. Volger, Physica **20**, 49 (1954).

[61] S.-W. Cheong and H.Y. Hwang, *"Ferromagnetism vs Charge/Orbital Ordering in Mixed-Valent Manganites"*, in *"Colssal Magnetoresistance Oxides"*, edited by Y. Tokura, Gordon and Breach, Monographs in Condensed Matter Science, London (2000).

[62] E.O. Wollen and W.C. Koehler, Phys. Rev. **100**, 545 (1955).

[63] C. Zener, Phys. Rev. **81**, 440 (1951).

[64] C. Zener, Phys. Rev. **82**, 403 (1951).

[65] C. Zener, Phys. Rev. **83**, 299 (1951).

[66] P.W. Anderson and H. Hasegawa, Phys. Rev. **100**, 675 (1955).

[67] P.-G. De Gennes, Phys. Rev. 118, 141 (1960).

[68] R. Von Helmolt, J. Wecker, B. Holzapfel, L. Schultz, and K. Samwer, Physical Review Letters, **71**, 2331 (1993).

[69] K. Chahara, T. Ohno, M. Kasai, and Y. Kozono, Appl. Phys. Lett. **63**, 1990 (1993).

[70] S. Jin, T.H. Tiefel, M. M.Cormack, R.A. Fastnacht, R. Ramesh, and L.H. Chen, Science **264**, 413 (1994).

[71] Y. Tokura, *"Colssal Magnetoresistance Oxides"*, Gordon and Breach, Monographs in Condensed Matter Science, London (2000).

[72] E. Dagotto,*"Nanoscale Phase Separation and Colossal Magnetoresistance"*, Springer, Berlin, Heidelberg (2003).

[73] Z. Jirák, S. Vratislav, and J. Zajícek, Phys. Stat. Sol. (a) **52**, K39 (1979).

[74] S. Chikazumi, *“Physics of Ferromagnetism”*, Oxford, Clarendon (1997).

[75] I.I. Mazin, Phys. Rev. Lett. **83**, 1427 (1999).

[76] N.F. Mott, Proc. R. Soc. A **156**, 368 (1936).

[77] R. Meservey and P.M. Tedrow, Phys. Rep. **238**, 173 (1994).

[78] I.A. Campbell and A. Fert, *“Ferromagnetic Materials”* vol. 3, ed E.P. Wohlfarth, Amsterdam, North-Holland (1982).

[79] A.F. Andreev and Zh. Eksp, Sov. Phys. JETP **19**, 1228 (1964).

[80] R.J. Soulen, J.M. Byers, M.S. Osofsky, B. Nadgorny, T. Ambrose, S.F. Cheng, P. R. Broussard, C.T. Tanaka, J. Nowak, J.S. Moodera, A. Barry, and J.M.D. Coey, Science **282**, 85 (1998).

[81] D.J. Monsma and S.S. Parkin, Appl. Phys. Lett. **77**, 720 (2000).

[82] T. Miyazaki, N. Tezuka, S. Kumagai, Y. Ando, H. Kubota, J. Murai, T. Watabe, and M. Yokota, J. Phys. D: Appl. Phys. **31**, 630 (1998).

[83] B. Sinkovic, E. Shekel, and S.L. Hulbert, Phys. Rev. B **52**, R8696 (1995).

[84] J.S. Moodera,L.R. Kinder, T.M. Wong, and R. Meservey, Phys. Rev. Lett. **74**, 3273 (1995).

[85] S.K. Upadhyay, A. Palanisami, R.N. Louie, and R.A. Buhrman, Phys. Rev. Lett. **81**, 3247 (1998).

[86] A. Rampe, D. Hartmann, W. Weber, S. Popovic, M. Reese, and G. Güntherodt, Phys. Rev. B **51**, 3230 (1995).

[87] W. Eib and S.F. Alvarado, Phys. Rev. Lett. **37**, 444 (1976).

[88] R. Meservey, D. Paraskevopoulos, and P.M. Tedrow , Phys. Rev. B **22**, 1331 (1980).

[89] G. Busch, M. Campagna, P. Cotti, and H.Ch. Siegmann, Phys. Rev. Lett. **22**, 597 (1969).

[90] J.-H. Park, E. Vescovo, H.-J. Kim, C. Kwon, R. Ramesh, and T. Venkatesan, Phys. Rev. Lett. **81**, 1953 (1998).

[91] P. Seneor, A. Fert, J.-L. Maurice, F. Montaigne, F. Petroff, and A. Vaur‘es, Appl. Phys. Lett. **74**, 4017 (1999).

[92] S.F. Alvarado, W. Eib, F. Meier, D.T. Pierce, K. Sattler, H.C. Siegmann, and J.P. Remeika, Phys. Rev. Lett. **34**, 319 (1975).

[93] D.C. Worledge and T.H. Geballe, Phys. Rev. Lett. **85**, 5182 (2000).

[94] D.C. Worledge and T.H. Geballe, Appl. Phys. Lett. **76**, 900 (2000).

[95] M. Viret, M. Drouet, J. Nassar, J.P. Contour, C. Fermon, and A. Fert, Europhys. Lett. **39**, 545 (1997).

[96] V.L. Ginzburg, Sov. Phys. JETP **4**, 153 (1957).

[97] A.W. Aschroft and N.D. Mermin, *"Solid State Physcis"*, Holt, Rinehardt, and Wiston (1976).

[98] K. Shimizu *et al.* , Nature **412**, 316 (2001).

[99] B.T. Mathias, H. Suhl, and E. Corenzwit, Phys. Rev. Lett. **1**, 92 (1958).

[100] N.F. Berk and J.R. Schrieffer, Phys. Rev. Lett. **17**, 433 (1966).

[101] V.L. Ginzburg, editor *"Superconductivity, Superdiamagnetism, Superfluidity"*, Mir (1987).

[102] G.T. Rado and H. Suhl, editors *"Magnetism"*, volume V, Academic Press (1973).

[103] L. Bauernfeind, W. Widder, and H.F. Braun, Physica C **254**, 151(1995).

[104] C. Bernhard,J.L. Tallon, C. Niedermayer, T. Blasius, A. Golnik, E. Brücher, R.K. Kremer, D.R. Noakes, C.E. Stronach, and E.J. Ansaldo, Phys. Rev. B **59**, 14099 (1999).

[105] C.W. Chu, Physica C **341-348**, 25 (2000).

[106] A.I. Buzdin and M. Y. Kupriyanov, JETP Letters **52**, 487 (1990).

[107] Z. Radovic, M. Ledvij, L. Dobrosavljevic, A.I. Buzdin, and J.R. Clem, Phys. Rev. B **44**, 759 (1991), and references therein.

[108] H.K. Wong, B. Y. Jin, H.Q. Yang, J.B. Ketterson, and J.E. Hilliard, J. Low Temp. Phys. **63**, 307 (1986).

[109] J.S. Jiang, D. Davidovic, D.H. Reich, and C.L. Chien, Phys. Rev. Lett.**74**, 314 (1995), and Phys. Rev. B **54**, 6119 (1996).

[110] Yu. N. Proshin and M.G. Khusainov, JETP **86**, 930 (1998).

[111] Yu.A. Izyumov, Yu.N. Proshin, and M.G. Khusainov, Phys. Usp. **45**, 109 (2002), and references therein.

[112] H.-U. Habermeier, G. Cristiani, R.K. Kremer, O. Lebedev, and G. Van Tendeloo, Physica C **364**, 298 (2001).

[113] Z. Sefrioui, D. Arias, V. Peña, J.E. Villegas, M. Varela, P. Prieto, C. León, J.L. Martinez, and J. Santamaria, Phys. Rev. B **67**, 214511 (2003).

[114] M. Quijada, J. Cerne, J.R. Simposon, H.D. Drew, K-H. Ahn, A.J. Millis, R. Shreekala, R. Ramesh, M. Rajeswari, and T. Venkatesan, Phys. Rev. B **58**, 16093 (1998).

[115] F.S. Bergeret and N. Garcia, Phys. Rev. B **70**, 052507 (2004).

[116] K.E. Gray, in *"Nonequilibrium Superconductivity, Phonons and Kapitza Boundaries"* , edited by K. E. Gray, Plenum, New York (1981).

[117] W.H. Parker, Phys. Rev. B **12**, 3667 (1975).

[118] D.B. Chrisey and G.K. Hubler, *"Pulsed Laser Deposition of Thin Film"*, John Wiley and Sons, Inc., New York (1994).

[119] S.M. Metev and V.P. Veiko,*"Laser Assisted Microtechnology"*, Springer, Berlin, Heidelberg (1994).

[120] J.F.M Cillessen, *"Pulsed Laser Deposition of Oxidic Film"*, Philips electronics N.V. (1996).

[121] F. Breech and L. Cross, Appl. Spect. **16**, 59 (1962).

[122] H.M. Smith and A.F. Turner, Appl. Opt. **4**, 147 (1965).

[123] C.K.N. Patel, Phys. Rev. Lett. **12**, 588 (1964).

[124] J.E. Geusic, H.M. Marcos, and L.G. Uitert, Appl. Phys. Lett. **4**, 182 (1964).

[125] Y. Zhang, H. Gu, and S. Iijima, Appl. Phys. Lett. **73**, 3827 (1998).

[126] D.B. Geohegan, A.A. Puretzky, and D.J. Rader, Appl. Phys. Lett. **74**, 3788 (1999).

[127] T.J. Goodwin, V.J. Leppert, S.H. Risbud, I.M. Kennedy, and H.W.H. Lee, Appl. Phys. Lett. **70**, 3122 (1997).

[128] J.T. Cheung, I.M. Gergis, J. James, and R.E. DeWames, Appl. Phys. Lett. **60**, 3180 (1992).

[129] J.A. Greer and H.J. Van Hook, Mater. Res. Soc. Symp. Proc. **191**, 171 (1990).

[130] A. Namiki, T. Kawai, K. Ichige, Surf. Sci. **166**, 129 (1986).

[131] M. Hanabusa, Mater. Res. Soc. Symp. Proc. **285**, 447 (1993).

[132] S. Metev, K. Meteva, Appl. Surf. Sci. **43**, 402 (1989).

[133] H. Kirchner, Phys. Lett. **26A**, 651 (1968).

[134] A.A. Polyanskii et al., Sov. Tech. Phys. Lett. **15**, 872 (1989).

[135] J.M. Phillips, J. Appl. Phys. **79**, 1829 (1996).

[136] J. Albrecht , S. Leonhardt , H. -U. Habermeier , S. Brück , R. Spolenak and H. Kronmüller, Physica C **404**, 18 (2004).

[137] J.D. Jorgensen, B.W. Veal, A.P. Paulikas, L.J. Nowicki, G.W. Crabtree, H. Claus, and W.K. Kwok, Phys. Rev. B **41**, 1863 (1990).

[138] J.M. Tranquada, S.M. Heald, A.R. Moodenbaugh, and Y. Xu, Phys. Rev. B **38**, 8893 (1988).

[139] G.A. Farnan, M.P. McCurry, D.G. Walmsley, Z.Z. Li, and H. Raffy, Supercond. Sci. Techn. **14**, 160 (2001).

[140] J. Ye and K. Nakamura, Phys. Rev. B **48**, 7554 (1993).

[141] D.J. Smith, Reports Prog. Phys. , 1513 (1997).

[142] P.R. Buseck, J.M. Cowley, and L. Eyring, Eds., *“High-Resolution Transmission Electron Microscopy and Associated Techniques”*, Oxford University Press, New York (1988).

[143] J.C.H. Spence, in *“Experimental High Resolution Electron Microscopy”*, 2^{nd} edition, Oxford University Press, New York (1988).

[144] W.J. de Ruijter and J.K. Weiss, Ultramicroscopy **50**, 269 (1993).

[145] T.R. Albrecht, S. Akamine, T.E. Carver, and C.F. Quate, J. Vac. Sci. Techn. A **8**, 3386 (1990).

[146] T.R. Albrecht, P. Grütter, D. Horne, and D. Rugar, J. Appl. Phys. **69**, 668 (1991).

[147] S. Alexander, L. Hellemans, O. Marti, J. Schneir, V. Elings, P.K. Hansma, M. Longmiro, and J. Gurley, J. Appl. Phys. **65**, 164 (1989).

[148] G. Binnig, C.F. Quate, and Ch. Gerber, Phys. Rev. Lett. **56**, 930 (1986).

[149] J.A. Gallego-Juárez, J. Phys. E: Sci. Instrum. **22**, 804 (1989).

[150] W.H. Tang, C.Y. Ng, C.Y. Yau, and J. Gao, Supercond. Sci. Technol. **13**, 580 (2000).

[151] J.M. Triscone, . Fischer, O. Brunner, L. Antognazza, A.D. Kent, and M.G. Karkut, Phys. Rev. Lett. **64**, 804 (1990).

[152] J. Albrecht, S. Soltan, and H.-U. Habermeier, Europhys. Lett. **63**, 881 (2003).

[153] H.-U. Habermeier, J. Albrecht, and S. Soltan, Supercond. Sci. Techn. **17**, S140 (2004).

[154] P.M. Tedrow and R. Meservey, Phys. Rev. Lett. **26**, 192 (1971).

[155] A.M. Goldman, V.A. Vaśko, P.A. Kraus, K.R. Nikolaev, and V.A. Larkin, J. Magn. Magn. Mater. **200**, 69 (1999).

[156] N.C. Yeh, R.P. Vasquez, C.C. Fu, A.V. Samoilov, Y. Li, and K. Vakili, Phys. Rev. B **60**, 10522 (1999).

[157] J.Y. Wei, J. Superconduct. **15**, 67 (2002).

[158] Y. Gim, A. W. Kleinsasser, and J. B. Barner, J. Appl. Phys. **90**, 4063 (2001).

[159] R.B. Praus, G.M. Gross, F.S. Razavi, and H.-U. Habermeier, J. Magn. Magn. Mater. **211**, 41 (2000).

[160] P. Przyslupski, I. Komissarov, W. Paszkowicz, P. Dluzewski, R. Minikayev, and M. Sawicki, Phys. Rev. B **69**, 134428 (2004).

[161] N. Haberkorn, J. Guimpel, M. Sirena, L.B. Steren, W. Saldarriaga, E. Baca, and M.E. Gomez, Appl. Phys. Lett. **84**, 3927 (2004).

[162] P.J. Hirschfeld and N.D. Goldenfeld, Phys. Rev. B **48**, 4219 (1993).

[163] M. Franz, C. Kallin, A.J. Berlinsky, and M.I. Salkola, Phys. Rev. B **56**, 7882 (1997).

[164] C.Y. Yang, A.R. Moodenbaugh, Y.L. Wang, Youwen Xu, S.M. Heald, D.O. Welch, M. Suenaga, D.A. Fischer, and J.E. Penner–Hahn, Phys. Rev. B **42**, 2231 (1990).

[165] C.S. Owen and D.J. Scalapino, Phys. Rev. Lett. **28**, 1559 (1972).

[166] E.J. Nicol and J.P. Carbotte, Phys. Rev. B **67**, 214506 (2003).

[167] D. Koller, M.S. Osofsky, D.B. Chrisey, J.S. Horwitz, R.J. Soulen, R.M. Stroud, C.R. Eddy, J. Kim, R.C.Y. Auyeung, J.M. Byers, B.F. Woodfield, G.M. Daly, T.W. Clinton, and M. Johnson, J. Appl. Phys. **83**, 6774 (1998).

[168] T. Holden, H.-U. Habermeier, G. Cristiani, A. Golnik, A. Boris, A. Pimenov, J. Humlíček, O. Lebedev, G. Van Tendeloo, B. Keimer, and C. Bernhard, Phys. Rev. B **69**, 064505 (2004).

[169] F. Chen, B. Gorshunov, G. Cristiani, H.-U. Habermeier, and M. Dressel, Solid State Commun. **131**, 295 (2004).

[170] S. Soltan, J. Albrecht, and H.-U. Hbaermeier, Phys. Rev. B **70**, 144517 (2004).

[171] P.B. Allen, H. Berger, O. Chauvet, L. Forro, T. Jarlborg, A. Junod, B. Revaz, and G. Santi, Phys. Rev. B **53**, 4393 (1996); D.J. Singh, J. Appl. Phys. **79**, 4818 (1996); I.I. Mazin and D.J. Singh, Phys. Rev. B **56**, 2556 (1997).

[172] G.P. Segre, N. Gedik, J. Orenstein, D.A. Bonn, R. Liang, and W.N. Hardy, Phys. Rev. Lett. **88**, 137001 (2002).

[173] J. Schmalian, D. Pines, and B. Stojkovic, Phys. Rev. Lett. **80**, 3839 (1998).

[174] Ch. Jooss, J. Albrecht, H. Kuhn, S. Leonhardt, and H. Kronmüller, Rep. Prog. Phys. **65**,651 (2002).

[175] P.E. Goa, H. Hauglin, A.A.F. Olson, D. Shantsev, and T.H. Johansen, Appl. Phys. Lett. **82**, 79 (2003).

[176] L.N. Bulaevskii, E.M. Chudnovsky, and M.P. Maley, Appl. Phys. Lett. **76**, 2594 (2000).

[177] L.E. Helseth, P.E. Goa, H. Hauglin, M. Baziljevich, and T.H. Johansen, Phys. Rev. B. **65**, 132514(2002).

[178] M.V. Milosevic, S.V. Yampolskii, and F.M. Peeters, Phys. Rev. B. **66**, 174519 (2002).

[179] X.X. Zhang, G.H. Wen, R.K. Zheng, G.C. Xiong, and G.J. Lian Europhys. Lett. **56**, 119 (2001).

[180] M. Kienzle, J. Albrecht, R. Warthmann, H. Kronmüller, S. Leonhardt, and Ch. Jooss, Phys. Rev. B. **66**, 54525 (2002).

[181] T. K. Nath, R. A. Rao, D. Lavric, C. B. Eom, L. Wu, and F. Tsui, Appl. Phys. Lett. **74**, 1615 (1999).

[182] L.N. Bulaevskii, E.M. Chudnovsky, and M.P. Maley, Appl. Phys. Lett. **76**, 2594 (2000).

[183] Alexander Schwarz, Marcus Liebmann, Uwe Kaiser, Roland Wiesendanger, Tae Won Noh, and Dong Wook Kim, Phys. Rev. Lett. **92**, 077206 (2004).

[184] J. Stahn, J. Chakhalian, C. Niedermayer, J. Hoppler, T. Gutberlet, J. Voigt, F. Treubel, H.-U. Habermeier, G. Cristiani, B. Keimer, C. Bernhard cond-mat/**0408311** submitted to Phys. Rev. Lett.

Acknowledgments

After four and a half years in Stuttgart, it is difficult to summarize in a few pages the contributions of several groups of people that made this work possible. Therefore, first of all I would like to ask for forgiveness to those whom I might forget in the following paragraphs.

I am very grateful to …

… Prof. Dr. Martin Dressel, I would like to thank him especially for giving me the possibility of carrying out this work under his supervision. And for the most enjoyable lectures in superconductivity I ever had.

… Prof. Dr. Helmut Kronmüller, for accepting the task of reviewing the thesis.

… Prof. Dr. Hanns-Ulrich Habermeier, for his catching enthusiasm in doing science and the patience and the readiness to discuss even the smallest questions I have had. I would like to thank him especially for giving me and transferring me so much knowledge and expertise, not only on physics, but also as a teacher and a friend.

… Dr. Joachim Albrecht, who is mostly responsible for helping me to complete the writing of this thesis and for many interesting discussions and very close collaboration. He has been a friend and mentor at the same time. All words I can say for you Joachim never could be enough or equal for your help!!!! …*SOUKRAN GAZELIN*… JOACHIM.

… Prof. Dr. Ahmed Ahmed Ramadan, my first teacher, and for his continuous effort to encourage me to succeed finishing the thesis.

… Dr. Claus Irslinger, for the warm welcome and hospitality from the first day in Stuttgart and for many help.

… Dr. Sylvia Leonhardt, M.Sc. Sebastian Brück, and Frau Theresa Dragon, Magneto-Optics group, for their continuous support during the thesis work and many stimulating discussions.

…Herr Georg Cristiani, for explaining the minor details of thin film growth conditions, and especially for his strong effort to provide high quality thin films of HTSC and CMR materials. My office-mate, Herr Frank Schartner, for creating an environment with plenty of perfect contacts for measurements.

…Dr. Peter Wochner, Dr. Martin Ahrens and Dr. Ulrich Clemens, for their friendship and multiple discussions and collaborations. Dr. habil. Eberhard Goering and Dr. Dagmar Goll for introducing me to the SQUID magnetometery.

…Prof. Dr. Giniyat Khaliullin, Prof. Dr. Eugene Kotomin, Dr. Peter Horsch, Dr. Dirk Manske, for many stimulating discussions, and for a thorough reading of parts of the this manuscript.

…Dr. Reinhard Kremer, for making possible the use of the setups in his group for investigations of magnetization. Especially with the help of Frau Eva Brücher and Frau Gisela Siegle.

…Herr Ernst Zimmermann Dr. Jürg Muster, Dr. Michael Wanitschek for his help in using LaTeX, Herr Karl Rößmann, Dr. Armin Burkhard, Herr Armin Schuhmacher, Herr Heinz-Joachim Stärke for their help dealing with Linux and Unix, and many other aspects of computer support.

…my colleagues in the Technology group, for the special atmosphere of team work and friendly collaboration and wonderful coffee sessions every morning at 9:00. Especially, I would like to mention: Brigit Lemke, Karin Foerderreuther, Stephan Schmid, Benjamin Stuhlhofer, Prof. Dr. F.S. Razavi, Dr. Joachim Albrecht, Georg Cristiani, Dr. Sylvia Leonhardt, Dr. Rainer Praus, Dr. Xiao-Jia Chen, Dr. Jean-René Duclere, Dr. Hui Zhang, Dr. Z. Wang, M.Sc. Yan Li, M.Sc. Yoshiharu Krockenberger, Dr. Andrei Matveev, Ingo Fritsch, and M.Sc. Yu Lan,

…, last but not least, to my *parents*, my wife ***Sahar***, my kids *Abdel-Rahman*, *Aya*, *Hossam* without your unconditional love and support, non of this would have been done. My young sister *Shadya* and old brother *Abdel-Monem* for their continuous support, and all my family without which this work would not have been performed, and for their patience, understanding, and love.

…, Max-Planck-Society and the Higher Education Minister, Egyptian government, are to be acknowledged. The Culture and students Scholarships office in Egyptian Embassy in Berlin is to be acknowledged, I would like to express my thanks to Prof. Dr. Aleya Khattab and Frau Amal Abduon for their continuous effort and help for all Ph.D. candidates.

List of publication

- X.J. Chen, S. Soltan, H. Zhang, and H.-U. Habermeier, Phys. Rev. B. **65**, 1714402 (2002).

  Title:*“Strain effect on electronic transport and ferromagnetic transition temperature in* $La_{0.9}Sr_{0.1}MnO_3$ *thin films”.*

- J. Albrecht, S. Soltan, and H.-U. Habermeier, EuroPhys. Lett. **63**, 881 (2003).

  Title:*“Hysteretic behavior of critical currents in heterostructures of high-temperature superconductors and ferromagnets”.*

- S. Soltan, C. Ulrich, G. Cristiani, and H.-U. Habermeier, Physica C **403**, 269 (2004).

  Title:*“Strain effects on the polaron binding energy in* $PrBa_2Cu_3O_{7-\delta}$ *thin films”.*

- S. Soltan, J. Albrecht, and H.-U. Habermeier, Phys. Rev. B. **70**, 144517 (2004).

  Title:*“Ferromagnetic/superconducting bilayer structure: A model system for spin diffusion length estimation”.*

- S. Soltan, J. Albrecht, G. Cristiani, and H.-U. Habermeier, phys.stat.sol.(c)**1**, 1836 (2004).

  Title:*“The role of spin diffusion quasiparticle in CMR/HTSC heterostructures”.*

- J. Albrecht, S. Soltan, and H.-U. Habermeier, Physica C **408-410**, 482 (2004).

  Title:*"Hysteretic currents in superconductor-ferromagnet heterostructures".*

- H.-U. Habermeier, J. Albrecht, S. Soltan, Supercond. Sci. Technol. **17**, S140 (2004).

  Title:*“Enhancement of flux-line pinning in all-oxide superconductor/ferromagnet heterostructures”.*

Submitted manuscripts

- S. Soltan, J. Albrecht, and H.-U. Habermeier. submitted to Phys. Rev. B. May 2004.

  Title: *“Spin polarized qausiparticles injection effects in YBCO thin films”.*

- J. Albrecht, S. Soltan, and H.-U. Habermeier, submitted to Phys. Rev. B. Aug. 2004.

  Title: *“Magnetic pinning of flux lines by magnetic domains in heterostructures of cuprates and manganites”*.

Manuscripts under preparation

- S. Soltan, J. Albrecht, and H.-U. Habermeier,

  Title: *“Spin polarized qausiparticles effects in the transition temperature of high-T_c superconductors”*.

- S. Soltan, J. Albrecht, and H.-U. Habermeier

  Title: *“Strain effect or oxygen content caused duplication of the transition temperature in $La_{1.9}Sr_{0.1}CuO_4$”*.

- S. Soltan, J. Albrecht, and H.-U. Habermeier.

  Title: *“Enhanced the Kosterlitz-Thouless transition temperature by spin polarized qausiparticles injection into high-T_c superconductors”*

Curriculum Vitæ

Soltan Eid Abdel-Gawad Soltan

January 26th, 1968	born in Giza, Egypt
August 26th, 1994	married with Sahar Kamal, 3 kids (Abdel-Rahman, Aya, Hossam)

Schools

1974–1980	Primary school at Giza (Egypt)
1980–1986	High school at Giza (Egypt)
06/1987	High school diploma

Undergraduate Studies

1987–1991	Studies of Physics at Faculty of Science, Helwan University–Cairo (Egypt)
06/1993	Pre-Master at Helwan University–Cairo (Egypt)
03/1997	Master at Faculty of Science, Helwan University–Cairo (Egypt) Advisors: Prof. Dr. A.A. Ramadan and Prof. Dr. S.A. Abdel-Haday Topic: *Structure-properties intercorrelation of high-T_c superconducting YBCO thin films*

Graduate Studies

06/1999	Pre-Ph.D. at Faculty of Science, Helwan University–Cairo (Egypt)
since 07/2000	Ph.D. student at Max-Planck-Institute for Solid State Research in Stuttgart: Advisor Prof. Dr. H.-U. Habermeier

Job

03/1992	Administrator in Physics Department at Faculty of Science, Helwan University–Cairo (Egypt)
since 06/1997	Assistance Lecturer in Physics Department, Faculty of Science, Helwan University–Cairo (Egypt)